The seismo-electric method

and its sensitivity to subsurface contrasts

Proefschrift

ter verkrijging van de graad van doctor
aan de Technische Universtiteit Delft,
op gezag van de Rector Magnificus prof.dr.ir. J.T. Fokkema,
voorzitter van het College van Promoties,
in het openbaar te verdedigen op woensdag 2 november 2005 om 10:30 uur
door Antonio FERNANDEZ-RAÑADA SHAW
Licenciado en Ciencias Físicas,
especialidad Física de la Tierra y el Cosmos,
Universidad Complutense de Madrid,
geboren te Madrid, Spanje.

Dit proefschrift is goedgekeurd door de promotor:
Prof.dr.ir. C.P.A. Wapenaar

Toegevoegd promotor: Dr.ir. E.C. Slob

Samenstelling promotiecommissie:

Rector Magnificus	voorzitter
Prof.dr.ir. C.P.A. Wapenaar	Technische Universiteit Delft, promotor
Dr.ir. E.C. Slob	Technische Universiteit Delft, toegevoegd promotor
Prof.dr.ir. J.T. Fokkema	Technische Universiteit Delft
Prof.dr.ir. A. Gisolf	Technische Universiteit Delft
Prof.dr. J. Trampert	Universiteit Utrecht
Prof.dr.ir. P.M. van den Berg	Technische Universiteit Delft
Prof.dr. U. Yaramanci	Technische Universität Berlin

ISBN-10: 9090201068

ISBN-13: 9789090201061

Printed in the Netherlands.

A mis padres Antonio y Maria
y mis hermanas Isabel e Ines,
de los que tanto he aprendido.

Y dicen que esto es facil...

Faemino & Cansado

Contents

Chapter 1

Introduction

In this PhD thesis we address the question: what can we measure with the seismo-electric effect and how? In order to do this we develop models of several possible acquisition setups and we study the possibility of reconstructing an interface from the seismic and electromagnetic measurements.

The seismo-electric effect is an energy transfer between seismic and electromagnetic wavefields taking place in an electrolyte saturated porous medium. This energy transfer is logically dependent on the mechanical parameters that affect the fluid flow in the pores and the amount of ions present, to name a few.

There are already very well known geophysical methods based on the reflection and refraction of seismic waves. Some of those methods are adapted in this thesis to exploit the seismo-electric effect and to explore the potential of it as a geophysical tool.

The source of the seismo-electric effect lays in the microscopic double layer created in the pore wall of the porous medium, as in Figure 1.1. Assuming we have a porous medium saturated with an electrolyte, the negative ions of the pore fluid are chemically adsorbed to the silicium atoms in the pore wall. The positive ions together with the positive side of the water molecules are then attracted to this layer of negative ions surrounding the grains. This leaves an excess of positive charge in the fluid.

During equilibrium, the overall charge in the porous medium is neutral since positive and negative ions cancel each other. However, during seismic or electromagnetic disturbances of this equilibrium there is a movement of ions that may generate a seismic or an electromagnetic wave. If we have a seismic wave passing by a saturated porous medium, the regions in the wavefront where the medium is compressed will squeeze the electrostatically charged fluid to the regions where

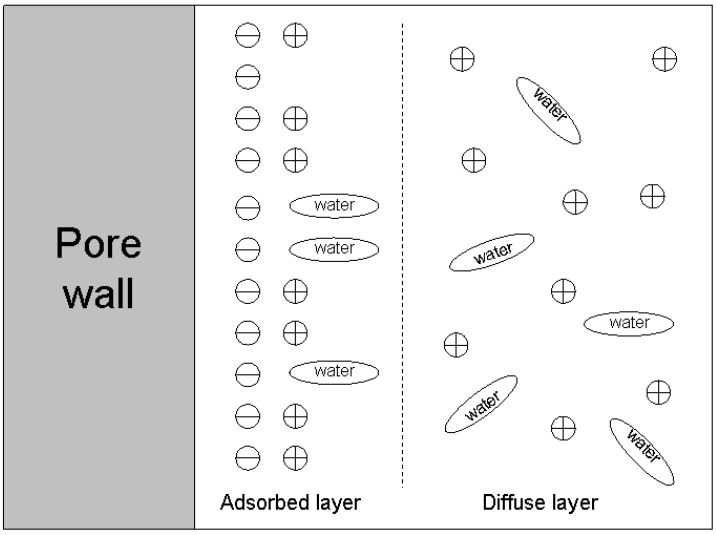

Figure 1.1: *The double layer: the negative ions adsorbed to the pore wall and the positive ions and water molecules attracted to them are fixed to the wall while those in the diffuse layer are free to move when mechanical or electromagnetic disturbances occur.*

the porous medium is expanded. This flow of charged particles generates an electric field that will travel across the porous medium inside the seismic wave. This is the first type of seismo-electric conversion. When this seismic wave encounters an interface in which there is a change in medium parameters as the porosity, permeability or the ion concentration of the pore fluid an electromagnetic wave is generated. Note that this electromagnetic wave has the frequency of the seismic wave that generates it, it is therefore not properly a wave but an electromagnetic diffusive field.

If we have an electromagnetic wave passing by a saturated porous medium, the free ions in the pores oscillate with the frequency of the electromagnetic wave generating an seismic disturbance that reaches everywhere the electromagnetic pulse does, but not further. Similarly to the previous case, when this electromagnetic wave encounters an interface there is a generation of a seismic wave that will travel across the porous medium independent of the electromagnetic wave that initially generated it.

1.1 Background

Theoretical approach

The relation between seismic and electromagnetic wavefields is known since as early as 1936, when in an article published by Thompson [25] he described the modulation of a current applied to the ground by the passage of a seismic wave train. Later he described it as a change in the ground resistivity. Shortly after that Ivanov [9] recorded electric fields generated with the passage of a seismic wave, without applying any current to the subsurface. He used a split-spread configuration and measured a reversal of the polarity on both sides of the source. He explained the seismo-electric effect in terms of a double layer in the pore walls of a saturated porous medium.

In 1944 Frenkel [6] described the seismo-electric effect in terms of electric fields generated by the electrolyte flow in the porous matrix, thus only took into account the field created as a compressional wave passes by, but he didn't take into account the full current present in Ampere's law.

In the following decades there were some scattered publications on this topic, in 1981 Ishido and Mizutani [8] developed a theoretical model for the ζ potential and studied the interesting dependencies of this parameter with pH, pressure and temperature.

The first attempt to derive a set of equations to model the seismo-electric coupling came with Neev and Yeatts [15] but they failed to apply the complete Maxwell's equations. The consequence of this is that their model does not take into account the conversion from and to shear waves.

Pride and Morgan [20] studied the electric fields produced by the pore fluid movement and under what conditions the electrical dissipation is significant compared to the viscous shear dissipation, and they concluded that this only occurs for low molarities and small pore sizes. Later, in 1994 Pride [18] derived a set of coupled equations that describe the conversion of energy between the electromagnetic and acoustic wavefields, and this set of equations is going to be the starting point of this thesis. These equations have the form of Maxwell's equations coupled to Biot's equations, and the coupling between the seismic and the electromagnetic wavefields lies in a frequency dependent coupling coefficient $\mathcal{L}$. This set of equations is the result of volume averaging the continuum equations applied to the grains and pore fluid. Later, together with Haartsen [19], they solved the electro-seismic boundary-value problem and obtained plane wave and point source solutions. In the last part of their publication they derived the boundary conditions that we are using in this thesis.

This thesis begins with the coupled equations derived by Pride [18] combined with the boundary conditions derived by Pride and Haartsen [19].

More recently Beamish [2] did a very complete review on the seismo-electric effect where he described and summarized the current state of the research in seismo-electrics.

Fieldwork measurements

Although theoretically there have been important advances in explaining the seismo-electric effect, there is still much work to be done in the area of fieldwork measurements. This effect was first suggested by Louis Statham and L. W. Blau of the Humble Company and after this, R. R. Thompson tested their assumptions in the field [25]. Since then there have been researchers who tried to measure and characterize the coupling of seismic and electromagnetic wavefields in the subsurface, as well as to exploit it as a geophysical prospecting tool. Parkomenko and Gaskarov [16] mentioned the possibility of using the seismo-electric effect as a wellbore tool since the response depends on rock properties, and they did some experiments in the field.

In the following decades there are some scattered publications describing field measurements like Martner and Sparks [12] who describe for the first time the arrival of an electromagnetic pulse that precedes a seismic wave from a source in a wellbore, and they identify it as the seismo-electric conversion at the water table. This is a different type of conversion of energy between seismic and electromagnetic waves.

Thompson and Gist [24] made field measurements and recorded signals from interfaces, that were correlated with well logs and additional seismic measurements. They claim the seismo-electric arrival can be recorded from as deep as 300m, therefore making it a useful exploration tool for the subsurface. They also measured the electro-osmotic effect, or the reciprocal of the seismo-electric, where they injected a time dependent electric current into the subsurface and recorded the seismic disturbance produced at an interface.

Mikhailov and Haartsen [13] performed very neat fieldwork experiments in which they located a possible seismo-electric arrival and did good prediction with their simulations. Later Oleg Mikhailov [14] detected fractured zones in a seismo-electric VSEP survey from the electromagnetic arrivals. Hunt and Worthington [7] measured also seismo-electric conversion using a similar method in a wellbore.

In a later work of Beamish [1] he studied how the different measuring conditions affect the results of a seismo-electric fieldwork, he experimented with different configurations of sources and receivers trying to find the optimal. And

more recently Butler and Kepic [3] and [11] have written about the difficulties of obtaining a clear seismo-electric signals in field measurements, suggesting the use of small preamplifiers placed at the electrodes on each channel to increase the signal to noise ratio and avoid interferences.

Laboratory measurements

After the first attempts to theoretically explain this phenomenon there were experiments carried in the laboratory trying to control and reproduce the conditions that yield a seismo-electric coupling, and trying to exploit it as a scientific tool. Pengra et al [17] used low frequency AC seismo-electric conversion to study rock properties. They perform laboratory experiments using AC techniques that show advantages over the known DC methods. They present the seismo-electric method as a useful lab tool to obtain the streaming potential coefficient and the electroosmosis coefficient.

But prior to use the seismo-electric effect as a reliable tool it is required that the effect is fully understood, with this approach Reppert et al. [21]- [22] studied the AC/DC streaming potentials and the AC/DC electroosmosis and they reconstructed experimentally the coupling coefficient $\mathcal{L}$.

More recently Zhenya Zhu [29]-[30] tested the seismo-electric conversion in laboratory, in borehole models using different materials. He obtained excellent results with very clear electromagnetic arrivals for a boundary in a wellbore, as well as for boundaries between wellbores.

Finally we shall mention Exxonmobile's extensive research and fieldwork tests on the seimo-electric effect. They have studied mainly the conversion from electromagnetic to seismic waves in a series of experiments that include measurements at the surface and inside wellbores. Some of their most recent results are published in [4] and [23].

1.2 Thesis outline

This thesis is divided into 6 chapters. The first chapter is logically the current chapter where we give a brief introduction to the seismo-electric effect and this thesis. In the second chapter we present the basic theory beginning with Pride's equations for the coupled electromagnetics and acoustics of porous media [18]. From Pride's equations we express the vertical variations of chosen wavefields in terms of the lateral variations of the same wavefield and we combine them into

a matrix-vector equation of the type

$$\frac{\partial \hat{\mathbf{Q}}}{\partial x_3} = \hat{\mathbf{A}}\hat{\mathbf{Q}} + \hat{\mathbf{D}}, \tag{1.1}$$

where $\hat{\mathbf{Q}}$ is the vector with the chosen field quantities, $\hat{\mathbf{A}}$ is an operator with the horizontal derivatives of $\hat{\mathbf{Q}}$ and the independent term $\hat{\mathbf{D}}$ contains the source quantities. Later in the chapter it is shown that for horizontally layered media the wave equation can be rearranged for certain conditions so that it uncouples into two independent sets of partial differential equations. These two sets of equations show us the two existing cases in the seismo-electric coupling: the P-SV-TM and the SH-TE cases. The P-SV-TM coupling includes the interactions between the compressional, vertical shear and TM electromagnetic waves, while the SH-TE coupling includes the interactions between the horizontal shear and the TE electromagnetic waves. TM and TE stand for "transverse magnetic" and "transverse electric" and the term refers to the polarization of the magnetic and electric fields in the electromagnetic wave.

In the third chapter we describe the one-way wave equations and how we transform two-way wavefields to one-way wavefields via the decomposition operator. We also describe an electro-kinetic survey by means of operators describing each of the phenomena taking place, such as excitation, propagation and reflection. Finally we show examples of two cases where we apply the theory of this chapter, first a simple reflection using just one-way wavefields and second a more complex case including the simulation of the source and receivers.

In the fourth chapter we describe further applications of the one-way operators defined in the foregoing chapter. First we derive global reflection and transmission coefficients in a similar way as Kennett [10] does for seismic waves, and in later sections we use them simulating a vertical seismo-electric profile (VSEP) as well as an electro-kinetic wellbore to wellbore survey in the (x_1, x_3, t) domain.

In the fifth chapter we analyze the information we can actually extract from the subsurface with a seismo-electric survey. We look at the reflections we obtain from different types of interfaces, and the different sensitivities the wavefields have to those interfaces. In order to do so we use a cost function with L_2 norm to compare the coefficients and the inversion of the coefficients for different ranges of the medium parameters. Under the ideal conditions these cost functions must have a minimum whose coordinates point at the lower medium parameters. In this way we check theoretically how reliable is the reconstruction of the interface.

Finally, in the sixth chapter we present our conclusions on the topics investigated in this thesis.

Chapter 2

Theoretical introduction

In this chapter we obtain the wave equation for electro-kinetic coupled waves, beginning with Pride's equations for the coupled electromagnetics and acoustics of porous media [18]. From Pride's equations we express the vertical variations of chosen wavefields in terms of the lateral variations of the same wavefield and we combine them into a matrix-vector equation of the type

$$\frac{\partial \hat{\mathbf{Q}}}{\partial x_3} = \hat{\mathbf{A}}\hat{\mathbf{Q}} + \hat{\mathbf{D}}, \tag{2.1}$$

where $\hat{\mathbf{Q}}$ is the vector with the chosen field quantities, $\hat{\mathbf{A}}$ is an operator with the horizontal derivatives of $\hat{\mathbf{Q}}$ and the independent term $\hat{\mathbf{D}}$ contains the source quantities. It is shown that under proper conditions for horizontally layered media the wave equation can be rearranged so that it uncouples into two independent sets of partial differential equations. These two sets of equations show us the two existing cases in the electro-kinetic coupling: the P-SV-TM and the SH-TE cases. The first comprises both compressional waves together with the vertical shear wave and the TM mode of the electromagnetic wave; the latter contains the horizontal shear wave and the TE mode of the electromagnetic wave. Finally we derive independent expressions for the operator matrix $\hat{\mathbf{A}}$ for both cases.

Through almost all this chapter quantities are expressed in the $(\mathbf{x}, \omega)$ domain and carry a hat ($\hat{}$) to denote it. Only in the last subsection, in order to express the operator matrix $\hat{\mathbf{A}}$ in the (p_1, ω) domain, we perform a Radon transformation and then the quantities carry a tilde ($\tilde{}$) to denote it. The results of this thesis will be shown in the (p_1, τ) and (x_1, t) domains. In order to do this an inverse Fourier transform will move the (p_1, ω) domain expressions to the (p_1, τ) domain, and a double inverse Fourier transform will transform expressions in the (k_1, ω)

domain to the (x_1, t) domain. There is no special notation for the expressions on these two last domains since we will only show the results.

We use Einstein's convention for repeated subscripts. Repeated Latin subscripts imply a summation from 1 to 3, hence

$$\frac{\partial v_i}{\partial x_i} \text{ stands for } \sum_{i=1}^{3} \frac{\partial v_i}{\partial x_i}. \tag{2.2}$$

Repeated Greek subscripts imply summation from 1 to 2, hence

$$\frac{\partial v_\alpha}{\partial x_\alpha} \text{ stands for } \sum_{\alpha=1}^{2} \frac{\partial v_\alpha}{\partial x_\alpha}. \tag{2.3}$$

This convention holds only for italic subscripts, but not for roman subscripts.

2.1 Fourier Transformation

In this thesis we will use the following definition for the Fourier transformation

$$\mathcal{F}\{f(\mathbf{x}, t)\} = \hat{f}(\mathbf{x}, \omega) = \int_{-\infty}^{\infty} f(\mathbf{x}, t) e^{-\mathrm{j}\omega t} dt, \tag{2.4}$$

where ω is the angular frequency, t is time, j is the imaginary unit and $f(t)$ is the time domain function that is transformed to the frequency domain function $\hat{f}(\omega)$. The inverse temporal Fourier transformation is

$$\mathcal{F}^{-1}\{F(\mathbf{x}, \omega)\} = f(\mathbf{x}, t) = \frac{1}{\pi} \Re \int_{0}^{\infty} \hat{f}(\mathbf{x}, \omega) e^{\mathrm{j}\omega t} d\omega. \tag{2.5}$$

when $f(\mathbf{x}, t)$ is real valued. Expression (2.5) transforms our quantities from the frequency domain back to the time domain. The symbol $\Re$ denotes that the real part is taken.

2.2 Basic equations in the frequency domain

To develop this set of equations we are going to take two postulates: the grains develop a diffussive double layer on their surface, and the net electric charge prior to the arrival of the disturbance is zero. These equations are only valid for

certain assumptions: the disturbances considered are linear.The pore fluid is an ideal electrolyte. Solid grains are isotropic. Wave induced diffusion effects are ignored. For this $\epsilon^{\mathrm{gr}} << \epsilon^{\mathrm{el}}$ the dielectric constant of the grains must be less than the one of the eletrolyte and the thickness of the double layer must be much smaller than the sizes of the grains. Finally the wave length is such that there is no scattering from the grains.

Pride's equations of motion for elastodynamic waves coupled to electromagnetic waves in a porous medium [18] are an extension of Biot's equations of motion. For an arbitrary inhomogeneous medium they are given by

$$j\omega\rho^b\hat{v}_i^s + j\omega\rho^f\hat{w}_i - \frac{\partial\hat{\tau}_{ij}^b}{\partial x_j} = \hat{f}_i^b, \tag{2.6}$$

$$j\omega\rho^f\hat{v}_i^s + \frac{\eta}{\hat{k}}\hat{w}_i' + \frac{\partial\hat{p}}{\partial x_i} = \hat{f}_i^f, \tag{2.7}$$

with

$$\hat{w}_i' = \hat{w}_i - \hat{\mathcal{L}}\hat{E}_i, \tag{2.8}$$

$$\hat{w}_i = \phi(\hat{v}_i^f - \hat{v}_i^s), \tag{2.9}$$

$$\rho^b = \phi\rho^f + (1-\phi)\rho^s, \tag{2.10}$$

where $\hat{w}_i$ is the Biot filtration velocity and $\hat{w}_i'$ is the effective filtration velocity, $\hat{E}_i$ is the averaged electric field strength and $\hat{\mathcal{L}}$ is the coupling coefficient, that accounts for the coupling between the elastodynamic and electromagnetic wavefields. $\hat{v}_i^s$ and $\hat{v}_i^f$ are the averaged solid and fluid particle velocities, ϕ the porosity, $\hat{\tau}_{ij}^b$ the averaged bulk stress, $\hat{p}$ the fluid pressure, ρ^s, ρ^f and ρ^b are respectively the solid, fluid and bulk densities, η is the fluid viscosity, $\hat{k}$ the dynamic permeability, $\hat{f}_i^b$ and $\hat{f}_i^f$ are the volume densities of the external force applied to the bulk phase and to the fluid phase, respectively. Note the effect of the electro-kinetic coupling $\hat{\mathcal{L}}$ in the effective filtration velocity $\hat{w}'$ and note too that if the coupling coefficient is changed to zero in equation (2.8), equations (2.6) and (2.7) reduce to Biot's equations of motion, i.e. no coupling takes place between the elastic and electromagnetic wavefields. The coupling coefficient is

$$\hat{\mathcal{L}} = \mathcal{L}_0\left[1 + j\frac{\omega}{\omega_c}\frac{m}{4}\left(1 - 2\frac{d}{\Lambda}\right)^2\left(1 - d\sqrt{\frac{j\omega\rho_f}{\eta}}\right)^2\right]^{-\frac{1}{2}} \tag{2.11}$$

where the static coupling coefficient $\mathcal{L}_0$ is defined as

$$\mathcal{L}_0 = -\frac{\phi}{\alpha_\infty}\frac{\epsilon_0\epsilon_r^f\zeta}{\eta}\left(1-2\frac{d}{\Lambda}\right) \tag{2.12}$$

where α_∞ is the tortuosity, ϵ_r^f is the fluid dielectric conductivity, η is the pore fluid viscosity, ζ is the zeta potential taken from [20] which expression is

$$\zeta = 8 + 26\log_{10} c \tag{2.13}$$

where the units are mV for the zeta potential and moles/l for the concentration c. The Debye length is

$$\frac{1}{d^2} = \sum_{l=1}^{L}\frac{(ez_l)^2\mathcal{N}_l}{\epsilon_o\kappa_f k_b T}. \tag{2.14}$$

where z_l are the valences, ez_l represents the net charge and sign of each of the species-l ions, $\mathcal{N}_l$ are the bulk-ionic concentrations, k_b is the Boltzmann constant and T the temperature. The critical frequency is

$$\omega_c = \frac{\phi\eta}{\alpha_\infty k_0\rho_f}. \tag{2.15}$$

The permeability is

$$\hat{k} = k_0\left[\left(1-i\frac{\omega}{\omega_c}\frac{4}{m}\right)^{\frac{1}{2}} - i\frac{\omega}{\omega_c}\right]^{-1} \text{ with } k_0 = \frac{\phi\Lambda^2}{m\alpha_\infty}. \tag{2.16}$$

and the parameter m is defined as

$$m = \frac{\phi\Lambda^2}{\alpha_\infty k_0} \tag{2.17}$$

Maxwell's electromagnetic field equations read

$$j\omega\hat{D}_i + \hat{J}_i - \varepsilon_{ijk}\frac{\partial\hat{H}_k}{\partial x_j} = -\hat{J}_i^e, \tag{2.18}$$

$$j\omega\hat{B}_i + \varepsilon_{ijk}\frac{\partial\hat{E}_k}{\partial x_j} = -\hat{J}_i^m, \tag{2.19}$$

where $\hat{D}_i$ and $\hat{B}_i$ are the averaged electric and magnetic flux densities, $\hat{H}_i$ is the averaged magnetic field strength, $\hat{J}_i$ is the averaged induced electric current density, $\hat{J}_i^e$ and $\hat{J}_i^m$ are the electric and magnetic source functions and ε_{ijk} is the alternating tensor given by

$$\varepsilon_{ijk} = \begin{cases} 1 & \text{if } i,j,k \text{ is an even permutation of 1,2,3} \\ -1 & \text{if } i,j,k \text{ is an odd permutation of 1,2,3} \\ 0 & \text{otherwise.} \end{cases} \tag{2.20}$$

The constitutive relations are given by [18]

$$\hat{D}_i = \epsilon_0 \epsilon_{\mathrm{r}} \hat{E}_i, \tag{2.21}$$

$$\hat{B}_i = \mu_0 \mu_{\mathrm{r}} \hat{H}_i, \tag{2.22}$$

$$\hat{J}_i = \hat{\sigma} \hat{E}_i - \hat{\mathcal{L}} \left(\frac{\partial \hat{p}}{\partial x_i} + j\omega \rho^f \hat{v}_i^s - \hat{f}_i^f \right), \tag{2.23}$$

where ϵ, μ and $\hat{\sigma}$ are respectively the permittivity, permeability and conductivity. The subscripts $_0$ refer to the value in the vacuum, and the subscripts $_{\mathrm{r}}$ refer to the relative value of the parameter.

Note here again that if the coupling coefficient $\hat{\mathcal{L}}$ is set to zero, equation (2.23) turns into Maxwell's constitutive equation for $\hat{J}_i$. According to Pride [18]

$$\epsilon_{\mathrm{r}} = \frac{\phi}{\alpha_\infty} (\epsilon_{\mathrm{r}}^f - \epsilon_{\mathrm{r}}^s) + \epsilon_{\mathrm{r}}^s, \tag{2.24}$$

$$\mu_{\mathrm{r}} = 1, \tag{2.25}$$

where α_∞ is the tortuosity, ϵ_{r}^f and ϵ_{r}^s are the fluid and solid dielectric constants.

The stress-strain relations read

$$-j\omega \hat{\tau}_{ij}^b + d_{ijkl} \frac{\partial \hat{v}_k^s}{\partial x_l} + \delta_{ij} C \frac{\partial \hat{w}_k}{\partial x_k} = 0, \tag{2.26}$$

$$j\omega \hat{p} + C \frac{\partial \hat{v}_k^s}{\partial x_k} + M \frac{\partial \hat{w}_k}{\partial x_k} = 0, \tag{2.27}$$

where d_{ijkl}, C and M are the stiffness parameters of the porous solid. For isotropic media the stiffness tensor is

$$d_{ijkl} = (K_{\mathrm{G}} - \frac{2}{3} G_{\mathrm{fr}}) \delta_{ij} \delta_{kl} + G_{\mathrm{fr}} (\delta_{ik} \delta_{jl} + \delta_{il} \delta_{jk}), \tag{2.28}$$

and the parameters C, M, and the Gassmann's bulk modulus K_G can be defined in terms of the fluid, solid and grain framework bulk moduli

$$K_{\mathrm{G}} = \frac{K_{\mathrm{fr}} + \phi K^f + (1+\phi)K^s\Delta}{1+\Delta}, \tag{2.29}$$

$$C = \frac{K^f + K^s\Delta}{1+\Delta}, \tag{2.30}$$

$$M = \frac{K^f}{\phi(1+\Delta)}, \tag{2.31}$$

where K^s and K^f are respectively the solid and fluid compression moduli, K_{fr} is the compression modulus of the solid framework and Δ is

$$\Delta = \frac{K^f}{\phi(K^s)^2}[(1-\phi)K^s - K_{\mathrm{fr}}], \tag{2.32}$$

where G_{fr} is the shear modulus of the solid framework.

Substituting the constitutive relations for $\hat{D}_i$, $\hat{B}_i$ and $\hat{J}_i$ into Maxwell's equations (2.18) and (2.19) and then adding $\hat{\mathcal{L}}$ times equation (2.7) to equation (2.18) gives

$$j\omega\epsilon_0\epsilon_r\hat{E}_i + (\hat{\sigma} - \frac{\eta}{\hat{k}}\hat{\mathcal{L}}^2)\hat{E}_i + \frac{\eta}{\hat{k}}\hat{\mathcal{L}}\hat{w}_i - \varepsilon_{ijk}\frac{\partial\hat{H}_k}{\partial x_j} = -\hat{J}_i^e, \tag{2.33}$$

$$j\omega\mu_0\hat{H}_i + \varepsilon_{ijk}\frac{\partial\hat{E}_k}{\partial x_j} = -\hat{J}_i^m \tag{2.34}$$

The equations (2.6), (2.7), (2.26), (2.27), (2.33) and (2.34) describe the propagation of the coupled elastodynamic and electromagnetic waves through an inhomogeneous isotropic porous medium.

2.3 Boundary conditions

At horizontal boundaries where the medium properties are not continuous the following wave quantities have to remain continuous according to the open pore

boundary conditions from Deresiewicz and Skalak [5]:

Normal and shear stresses in the bulk; $\hat{\boldsymbol{\tau}}_3^b$, are continuous.
Normal stress in the fluid phase; $\hat{p}$, is continuous.
Normal and horizontal velocities in the bulk; $\hat{\mathbf{v}}^s$, are continuous.
Normal component of filtration velocity; $\hat{w}_3$, is continuous.
Tangential electric field; $\hat{\mathbf{E}}_0$, is continuous.
Tangential magnetic field; $\hat{\mathbf{H}}_0$, is continuous.

All these quantities are contained in the continuous wave vector $\hat{\mathbf{Q}}$

$$\hat{\mathbf{Q}} = (-(\hat{\boldsymbol{\tau}}_3^b)^t \quad \hat{p} \quad (\hat{\mathbf{E}}_0)^t \quad (\hat{\mathbf{v}}^s)^t \quad \hat{w}_3 \quad (\hat{\mathbf{H}}_0)^t)^t \tag{2.35}$$

where

$$\hat{\boldsymbol{\tau}}_3^b = \begin{pmatrix} \hat{\tau}_{13}^b \\ \hat{\tau}_{23}^b \\ \hat{\tau}_{33}^b \end{pmatrix}, \hat{\mathbf{v}}^s = \begin{pmatrix} \hat{v}_1^s \\ \hat{v}_2^s \\ \hat{v}_3^s \end{pmatrix}, \hat{\mathbf{E}}_0 = \begin{pmatrix} \hat{E}_1 \\ \hat{E}_2 \end{pmatrix}, \hat{\mathbf{H}}_0 = \begin{pmatrix} \hat{H}_2 \\ -\hat{H}_1 \end{pmatrix}, \tag{2.36}$$

and the superscript t denotes transposition.

2.4 Wave equations in matrix form

Here we reorganize Pride's equations following the scheme in [27] in such a way that the variations of the chosen wavefields along the x_3 direction are expressed in terms of the lateral variations of the same wavefield, as in equation (2.1). Our aim is to obtain an equation in terms of the quantities that are continuous over a horizontal boundary. This way we will be able to derive the wavefields composition and decomposition operators and later define our models in terms of one-way wavefields. We rewrite equations (2.6) and (2.7) as

$$j\omega\rho^b\hat{\mathbf{v}}^s + j\omega\rho^f\boldsymbol{\delta}_j\hat{w}_j - \frac{\partial\hat{\boldsymbol{\tau}}_j^b}{\partial x_j} = \hat{\mathbf{f}}^b, \tag{2.37}$$

$$j\omega\rho^f\boldsymbol{\delta}_i^t\hat{\mathbf{v}}^s + \frac{\eta}{\hat{k}}[\hat{w}_i - \hat{\boldsymbol{\mathcal{L}}}(\boldsymbol{\gamma}_i^t\hat{\mathbf{E}}_0 + \delta_{3i}\hat{E}_3)] + \frac{\partial\hat{p}}{\partial x_i} = \hat{f}_i^f, \tag{2.38}$$

where

$$\boldsymbol{\delta}_i = \begin{pmatrix} \delta_{1i} \\ \delta_{2i} \\ \delta_{3i} \end{pmatrix}, \boldsymbol{\gamma}_i = \begin{pmatrix} \delta_{1i} \\ \delta_{2i} \end{pmatrix}. \tag{2.39}$$

In order to formulate the stress-strain relations in a similar way we must get rid of the term $\partial\hat{w}_k/\partial x_k$ from equation (2.26) using equation (2.27). From the latter we have

$$\frac{\partial\hat{w}_k}{\partial x_k} = -\frac{1}{M}\left(C\frac{\partial\hat{v}_k^s}{\partial x_k} + j\omega\hat{p}\right) \tag{2.40}$$

which is substituted into (2.26) yielding

$$-j\omega\hat{\tau}_{ij}^b + e_{ijkl}\frac{\partial\hat{v}_k^s}{\partial x_l} - j\omega\frac{C}{M}\delta_{ij}\hat{p} = 0, \tag{2.41}$$

where

$$e_{ijkl} = d_{ijkl} - \frac{C^2}{M}\delta_{ij}\delta_{kl}. \tag{2.42}$$

The stress-strain relations are finally rewritten as

$$-j\omega\hat{\boldsymbol{\tau}}_j^b + \mathbf{C}_{jl}\frac{\partial\hat{\mathbf{v}}^s}{\partial x_l} + j\omega\frac{C}{M}\boldsymbol{\delta}_j\hat{p} = \mathbf{0}, \tag{2.43}$$

$$j\omega\hat{p} + C\boldsymbol{\delta}_k^t\frac{\partial\hat{\mathbf{v}}^s}{\partial x_k} + M\frac{\partial\hat{w}_k}{\partial x_k} = 0, \tag{2.44}$$

where

$$\mathbf{C}_{jl} = \begin{pmatrix} e_{1j1l} & e_{1j2l} & e_{1j3l} \\ e_{2j1l} & e_{2j2l} & e_{2j3l} \\ e_{3j1l} & e_{3j2l} & e_{3j3l} \end{pmatrix}, \mathbf{0} = \begin{pmatrix} 0 \\ 0 \\ 0 \end{pmatrix}, \tag{2.45}$$

and

$$(\mathbf{C}_{jl})_{ik} = e_{ijkl} = S\delta_{ij}\delta_{kl} + G_{\mathrm{fr}}(\delta_{ik}\delta_{jl} + \delta_{il}\delta_{jk}), \tag{2.46}$$

where

$$S = K_G - \frac{2}{3}G_{\mathrm{fr}} - \frac{C^2}{M}. \tag{2.47}$$

Pride's parameters S, K_G, G_{fr}, C and M can be expressed in terms of Biot's parameters A, N, Q and R according to

$$S = A - \frac{Q^2}{R}, \quad C = \frac{Q+R}{\phi}, \quad M = \frac{R}{\phi^2}, \tag{2.48}$$

$$K_G - \frac{2}{3}G_{\mathrm{fr}} = A + 2Q + R, \qquad G_{\mathrm{fr}} = N \tag{2.49}$$

In the electro-magnetic field equations we also separate the vertical from the horizontal derivaties of the electric and magnetic fields. From (2.33) we obtain

$$j\omega\hat{\epsilon}\hat{\mathbf{E}}_0 + \frac{\eta}{\hat{k}}\hat{\mathcal{L}}\boldsymbol{\gamma}_\alpha\hat{w}_\alpha + \frac{\partial\hat{\mathbf{H}}_0}{\partial x_3} - \begin{pmatrix} \frac{\partial}{\partial x_2} \\ \frac{-\partial}{\partial x_1} \end{pmatrix}\hat{H}_3 = -\mathbf{J}_0^e, \tag{2.50}$$

$$j\omega\hat{\epsilon}\hat{E}_3 + \frac{\eta}{\hat{k}}\hat{\mathcal{L}}\hat{w}_3 - \begin{pmatrix} \frac{\partial}{\partial x_1} & \frac{\partial}{\partial x_2} \end{pmatrix}\hat{\mathbf{H}}_0 = -J_3^e, \tag{2.51}$$

analogously from (2.34) we obtain

$$j\omega\mu_0\hat{\mathbf{H}}_0 + \frac{\partial\hat{\mathbf{E}}_0}{\partial x_3} - \begin{pmatrix} \frac{\partial}{\partial x_1} \\ \frac{\partial}{\partial x_2} \end{pmatrix}\hat{E}_3 = -\hat{\mathbf{J}}_0^m, \tag{2.52}$$

$$j\omega\mu_0\hat{H}_3 - \begin{pmatrix} \frac{\partial}{\partial x_2} & -\frac{\partial}{\partial x_1} \end{pmatrix}\hat{\mathbf{E}}_0 = -\hat{J}_3^m, \tag{2.53}$$

where

$$\hat{\mathbf{J}}_0^e = \begin{pmatrix} \hat{J}_1^e \\ \hat{J}_2^e \end{pmatrix}, \hat{\mathbf{J}}_0^m = \begin{pmatrix} \hat{J}_2^m \\ -\hat{J}_1^m \end{pmatrix}, \tag{2.54}$$

and $\hat{\epsilon}$ is

$$\hat{\epsilon} = \epsilon_0\epsilon_r + \frac{1}{j\omega}(\hat{\sigma} - \frac{\eta}{\hat{k}}\hat{\mathcal{L}}^2). \tag{2.55}$$

Now we compile all the needed vertical derivatives

$$-\frac{\partial\hat{\boldsymbol{\tau}}_3^b}{\partial x_3} = -j\omega\rho^b\hat{\mathbf{v}}^s - j\omega\rho^f\ (\boldsymbol{\delta}_\alpha\hat{w}_\alpha + \boldsymbol{\delta}_3\hat{w}_3) + \frac{\partial\hat{\boldsymbol{\tau}}_\alpha^b}{\partial x_\alpha} + \hat{\mathbf{f}}^b, \tag{2.56}$$

$$\frac{\partial\hat{p}}{\partial x_3} = -j\omega\rho^f\boldsymbol{\delta}_3^t\hat{\mathbf{v}}^s - \frac{\eta}{\hat{k}}[\hat{w}_3 - \hat{\mathcal{L}}\hat{E}_3] + \hat{f}_3^f, \tag{2.57}$$

$$\frac{\partial\hat{\mathbf{v}}^s}{\partial x_3} = \mathbf{C}_{33}^{-1}\left[j\omega\hat{\tau}_3^b + j\omega\frac{C}{M}\boldsymbol{\delta}_3\hat{p} - \mathbf{C}_{3\beta}\frac{\partial\hat{\mathbf{v}}^s}{\partial x_\beta}\right], \tag{2.58}$$

$$\frac{\partial\hat{w}_3}{\partial x_3} = -\frac{j\omega}{M}\hat{p} - \frac{C}{M}\left[\boldsymbol{\delta}_\beta^t\frac{\partial\hat{\mathbf{v}}^s}{\partial x_\beta} + \boldsymbol{\delta}_3^t\frac{\partial\hat{\mathbf{v}}^s}{\partial x_3}\right] - \frac{\partial\hat{w}_\beta}{\partial x_\beta}, \tag{2.59}$$

$$\frac{\partial\hat{\mathbf{E}}_0}{\partial x_3} = -j\omega\mu_0\hat{\mathbf{H}}_0 + \begin{pmatrix} \frac{\partial}{\partial x_1} \\ \frac{\partial}{\partial x_2} \end{pmatrix}\hat{E}_3 - \hat{\mathbf{J}}_0^m, \tag{2.60}$$

$$\frac{\partial\hat{\mathbf{H}}_0}{\partial x_3} = -j\omega\hat{\epsilon}\hat{\mathbf{E}}_0 - \frac{\eta}{\hat{k}}\hat{\mathcal{L}}\boldsymbol{\gamma}_\alpha\hat{w}_\alpha + \begin{pmatrix} \frac{\partial}{\partial x_2} \\ \frac{-\partial}{\partial x_1} \end{pmatrix}\hat{H}_3 - \hat{\mathbf{J}}_0^e. \tag{2.61}$$

Now we have to express the vertical derivatives as functions of the elements of $\hat{\mathbf{Q}}$ and their horizontal derivatives.

In equation (2.56) we eliminate the terms $\boldsymbol{\delta}_\alpha \hat{w}_\alpha$ and $\partial \hat{\boldsymbol{\tau}}^b_\alpha / \partial x_\alpha$ combining equations (2.43), (2.38) and (2.44)

$$-\frac{\partial \hat{\boldsymbol{\tau}}^b_3}{\partial x_3} = -j\omega\rho^b \hat{\mathbf{v}}^s + j\omega\rho^f \boldsymbol{\delta}_\alpha \left(j\omega\rho^f \frac{\hat{k}}{\eta} \boldsymbol{\delta}^t_\alpha \hat{\mathbf{v}}^s + \frac{\hat{k}}{\eta}\frac{\partial \hat{p}}{\partial x_\alpha} - \hat{\mathcal{L}}\boldsymbol{\gamma}^t_\alpha \hat{\mathbf{E}}_0 - \frac{\hat{k}}{\eta}\hat{f}^f_\alpha \right) - j\omega\rho^f \boldsymbol{\delta}_3 \hat{w}_3 + \frac{1}{j\omega}\frac{\partial}{\partial x_\alpha}\left[\mathbf{C}_{\alpha\beta}\frac{\partial \hat{\mathbf{v}}^s}{\partial x_\beta} + \mathbf{C}_{\alpha 3}\frac{\partial \hat{\mathbf{v}}^s}{\partial x_3} - j\omega\frac{C}{M}\boldsymbol{\delta}_\alpha \hat{p}\right] + \hat{\mathbf{f}}^b. \quad (2.62)$$

Substituting the term $\partial \hat{\mathbf{v}}^s / \partial x_3$ by equation (2.58) yields

$$\frac{\partial \hat{\tau}^b_3}{\partial x_3} = \frac{-\partial}{\partial x_\alpha}(\mathbf{C}_{\alpha 3}\mathbf{C}^{-1}_{33}\hat{\tau}^b_3) - j\omega\rho^f \frac{\hat{k}}{\eta}\boldsymbol{\delta}_\alpha \frac{\partial \hat{p}}{\partial x_\alpha} + \frac{1}{j\omega}\frac{\partial}{\partial x_\alpha}\left[j\omega\frac{C}{M}\mathbf{u}_\alpha \hat{p} - \mathbf{U}_{\alpha\beta}\frac{\partial \hat{\mathbf{v}}^s}{x_\beta}\right] + j\omega(\rho^b \mathbf{I}_3 - j\omega(\rho^f)^2 \frac{\hat{k}}{\eta}\boldsymbol{\delta}_\alpha \boldsymbol{\delta}^t_\alpha)\hat{\mathbf{v}}^s + j\omega\rho^f \boldsymbol{\delta}_3 \hat{w}_3 + j\omega\rho^f \hat{\mathcal{L}}\boldsymbol{\delta}_\alpha \boldsymbol{\gamma}^t_\alpha \hat{\mathbf{E}}_0 - \hat{\mathbf{f}}^b + j\omega\rho^f \frac{\hat{k}}{\eta}\boldsymbol{\delta}_\alpha \hat{f}^f_\alpha \quad (2.63)$$

where

$$\mathbf{U}_{\alpha\beta} = \mathbf{C}_{\alpha\beta} - \mathbf{C}_{\alpha 3}\mathbf{C}^{-1}_{33}\mathbf{C}_{3\beta}, \quad (2.64)$$

$$\mathbf{u}_\alpha = \boldsymbol{\delta}_\alpha - \mathbf{C}_{\alpha 3}\mathbf{C}^{-1}_{33}\boldsymbol{\delta}_3. \quad (2.65)$$

In equation (2.57) we eliminate the term $\hat{E}_3$ with equation (2.34), which gives

$$\frac{\partial \hat{p}}{\partial x_3} = -j\omega\rho^f \boldsymbol{\delta}^t_3 \hat{\mathbf{v}}^s - \frac{\eta}{\hat{k}}\left(1 + \frac{\hat{\rho}^E}{\hat{\epsilon}}\hat{\mathcal{L}}^2\right)\hat{w}_3 + \frac{\hat{\rho}^E}{\hat{\epsilon}}\hat{\mathcal{L}}\begin{pmatrix}\frac{\partial}{\partial x_1} & \frac{\partial}{\partial x_2}\end{pmatrix}\hat{\mathbf{H}}_0 - \frac{\hat{\rho}^E}{\hat{\epsilon}}\hat{\mathcal{L}}\hat{J}^e_3 + \hat{f}^f_3, \quad (2.66)$$

where

$$\hat{\rho}^E = \frac{\eta}{j\omega\hat{k}}. \quad (2.67)$$

In equation (2.59) we eliminate $\partial \hat{\mathbf{v}}^s / \partial x_3$ and $\partial \hat{w}_\beta / \partial x_\beta$ with equations (2.58)

and (2.38) giving

$$\frac{\partial \hat{w}_3}{\partial x_3} = -\frac{C}{M}\boldsymbol{\delta}_3^t \mathbf{C}_{33}^{-1}\left[j\omega\hat{\boldsymbol{\tau}}_3^b + j\omega\frac{C}{M}\boldsymbol{\delta}_3\hat{p}\right] - \frac{j\omega}{M}\hat{p} + \frac{\partial}{\partial x_\beta}\left[\frac{\hat{k}}{\eta}\left(\frac{\partial \hat{p}}{\partial x_\beta} - \hat{f}_\beta^f\right) + j\omega\rho^f\frac{\hat{k}}{\eta}\boldsymbol{\delta}_\beta^t\hat{\mathbf{v}}^s - \hat{\mathcal{L}}\boldsymbol{\gamma}_\beta^t\hat{\mathbf{E}}_0\right] - \frac{C}{M}\mathbf{u}_\beta^t\frac{\partial\hat{\mathbf{v}}^s}{\partial x_\beta}. \quad (2.68)$$

In equation (2.60) we remove $\hat{E}_3$ using equation (2.51) yielding

$$\frac{\partial\hat{\mathbf{E}}_0}{\partial x_3} = -j\omega\mu_0\hat{\mathbf{H}}_0 + \begin{pmatrix}\frac{\partial}{\partial x_1}\\ \frac{\partial}{\partial x_2}\end{pmatrix}\frac{1}{j\omega\hat{\epsilon}}\begin{pmatrix}\frac{\partial}{\partial x_1} & \frac{\partial}{\partial x_2}\end{pmatrix}\hat{\mathbf{H}}_0 - \begin{pmatrix}\frac{\partial}{\partial x_1}\\ \frac{\partial}{\partial x_2}\end{pmatrix}\frac{\hat{\rho}^E}{\hat{\epsilon}}\hat{\mathcal{L}}\hat{w}_3 - \hat{\mathbf{J}}_0^m - \begin{pmatrix}\frac{\partial}{\partial x_1}\\ \frac{\partial}{\partial x_2}\end{pmatrix}\frac{1}{j\omega\hat{\epsilon}}\hat{J}_3^e. \quad (2.69)$$

In equation (2.61) we eliminate $\hat{H}_3$ and $\hat{w}_\alpha$ using equations (2.53) and (2.38) yielding

$$\frac{\partial\hat{\mathbf{H}}_0}{\partial x_3} = -j\omega\hat{\epsilon}\hat{\mathbf{E}}_0 + \frac{\eta}{\hat{k}}\hat{\mathcal{L}}\boldsymbol{\gamma}_\alpha\left(j\omega\rho^f\frac{\hat{k}}{\eta}\boldsymbol{\delta}_\alpha^t\hat{\mathbf{v}}^s + \frac{\hat{k}}{\eta}\left(\frac{\partial\hat{p}}{\partial x_\alpha} - f_\alpha^f\right) - \hat{\mathcal{L}}\boldsymbol{\gamma}_\alpha^t\hat{\mathbf{E}}_0\right) - \hat{\mathbf{J}}_0^e + \begin{pmatrix}\frac{\partial}{\partial x_2}\\ \frac{-\partial}{\partial x_1}\end{pmatrix}\frac{1}{j\omega\mu_0}\begin{pmatrix}\frac{\partial}{\partial x_2} & \frac{-\partial}{\partial x_1}\end{pmatrix}\hat{\mathbf{E}}_0 - \begin{pmatrix}\frac{\partial}{\partial x_2}\\ \frac{-\partial}{\partial x_1}\end{pmatrix}\frac{1}{j\omega\mu_0}\hat{J}_3^m. \quad (2.70)$$

Equations (2.58), (2.63), (2.66), (2.68), (2.69) and (2.70) can be now combined into the matrix-vector equation

$$\frac{\partial\hat{\mathbf{Q}}}{\partial x_3} = \hat{\mathbf{A}}\hat{\mathbf{Q}} + \hat{\mathbf{D}}, \quad (2.71)$$

where

$$\hat{\mathbf{Q}} = (-(\hat{\boldsymbol{\tau}}_3^b)^t \quad \hat{p} \quad (\hat{\mathbf{E}}_0)^t \quad (\hat{\mathbf{v}}^s)^t \quad \hat{w}_3 \quad (\hat{\mathbf{H}}_0)^t)^t \quad (2.72)$$

$$\hat{\mathbf{D}} = \begin{pmatrix} \hat{\mathbf{f}}^b - j\omega\rho^f \frac{\hat{k}}{\eta}\boldsymbol{\delta}_\alpha \hat{f}^f_\alpha \\ -\frac{\hat{\rho}^E}{\hat{\epsilon}}\hat{\mathcal{L}}\hat{J}^e_3 + \hat{f}^f_3 \\ -\hat{\mathbf{J}}^m_0 - \begin{pmatrix} \frac{\partial}{\partial x_1} \\ \frac{\partial}{\partial x_2} \end{pmatrix} \frac{1}{j\omega\hat{\epsilon}}\hat{J}^e_3 \\ \mathbf{0} \\ -\frac{\partial}{\partial x_\beta}\left(\frac{\hat{k}}{\eta}\hat{f}^f_\beta\right) \\ -\hat{\mathbf{J}}^e_0 - \begin{pmatrix} \frac{\partial}{\partial x_2} \\ -\frac{\partial}{\partial x_1} \end{pmatrix} \frac{1}{j\omega\hat{\mu}_0}\hat{J}^m_3 - \hat{\mathcal{L}}\boldsymbol{\gamma}_\alpha \hat{f}^f_\alpha \end{pmatrix} \tag{2.73}$$

and the matrix operator $\hat{\mathbf{A}}$ is composed by the following submatrices

$$\hat{\mathbf{A}} = \begin{pmatrix} \hat{\mathbf{A}}_{11} & \hat{\mathbf{A}}_{12} \\ \hat{\mathbf{A}}_{21} & \hat{\mathbf{A}}_{22} \end{pmatrix}, \tag{2.74}$$

where

$$\hat{\mathbf{A}}_{11} = \begin{pmatrix} \hat{\mathbf{A}}^{11}_{11} & \hat{\mathbf{A}}^{12}_{11} & \hat{\mathbf{A}}^{13}_{11} \\ \mathbf{0}_{3\times3} & \mathbf{0}_{3\times1} & \mathbf{0}_{3\times2} \end{pmatrix}, \qquad \hat{\mathbf{A}}_{12} = \begin{pmatrix} \hat{\mathbf{A}}^{11}_{12} & \hat{\mathbf{A}}^{12}_{12} & \mathbf{0}_{3\times2} \\ \hat{\mathbf{A}}^{21}_{12} & \hat{\mathbf{A}}^{22}_{12} & \hat{\mathbf{A}}^{23}_{12} \\ \mathbf{0}_{2\times3} & \hat{\mathbf{A}}^{32}_{12} & \hat{\mathbf{A}}^{33}_{12} \end{pmatrix}, \tag{2.75}$$

$$\hat{\mathbf{A}}_{21} = \begin{pmatrix} \hat{\mathbf{A}}^{11}_{21} & \hat{\mathbf{A}}^{12}_{21} & \mathbf{0}_{3\times2} \\ \hat{\mathbf{A}}^{21}_{21} & \hat{\mathbf{A}}^{22}_{21} & \hat{\mathbf{A}}^{23}_{21} \\ \mathbf{0}_{2\times3} & \hat{\mathbf{A}}^{32}_{21} & \hat{\mathbf{A}}^{33}_{21} \end{pmatrix}, \qquad \hat{\mathbf{A}}_{22} = \begin{pmatrix} \hat{\mathbf{A}}^{11}_{22} & \mathbf{0}_{3\times3} \\ \hat{\mathbf{A}}^{21}_{22} & \mathbf{0}_{1\times3} \\ \hat{\mathbf{A}}^{31}_{22} & \mathbf{0}_{2\times3} \end{pmatrix}, \tag{2.76}$$

where the dimension of $\mathbf{A}_{11}$, $\mathbf{A}_{12}$, $\mathbf{A}_{21}$ and $\mathbf{A}_{22}$ is 6×6 and $\mathbf{0}_{m\times n}$ is a zeros matrix of dimension $m \times n$. The elements of these submatrices are

$$\hat{\mathbf{A}}_{11}^{11} = -\frac{\partial}{\partial x_\alpha}(\mathbf{C}_{\alpha 3}\mathbf{C}_{33}^{-1}\cdot), \tag{2.77}$$

$$\hat{\mathbf{A}}_{11}^{12} = j\omega\rho^f\frac{\hat{k}}{\eta}\boldsymbol{\delta}_\alpha\frac{\partial}{\partial x_\alpha} - \frac{\partial}{\partial x_\alpha}\left(\frac{C}{M}\mathbf{u}_\alpha\cdot\right), \tag{2.78}$$

$$\hat{\mathbf{A}}_{11}^{13} = -j\omega\rho^f\hat{\mathcal{L}}\boldsymbol{\delta}_\alpha\boldsymbol{\gamma}_\alpha^t, \tag{2.79}$$

$$\hat{\mathbf{A}}_{12}^{11} = \frac{1}{j\omega}\frac{\partial}{\partial x_\alpha}\left[\mathbf{U}_{\alpha\beta}\frac{\partial}{\partial x_\beta}\cdot\right] - j\omega(\rho^b\mathbf{I}_3 - j\omega(\rho^f)^2\frac{\hat{k}}{\eta}\boldsymbol{\delta}_\alpha\boldsymbol{\delta}_\alpha^t), \tag{2.80}$$

$$\hat{\mathbf{A}}_{12}^{12} = -j\omega\rho^f\boldsymbol{\delta}_3, \tag{2.81}$$

$$\hat{\mathbf{A}}_{12}^{21} = -j\omega\rho^f\boldsymbol{\delta}_3^t, \tag{2.82}$$

$$\hat{\mathbf{A}}_{12}^{22} = -\frac{\eta}{\hat{k}}\left(1 + \frac{\hat{\rho}^E}{\hat{\epsilon}}\hat{\mathcal{L}}^2\right), \tag{2.83}$$

$$\hat{\mathbf{A}}_{12}^{23} = \frac{\hat{\rho}^E}{\hat{\epsilon}}\hat{\mathcal{L}}\begin{pmatrix}\frac{\partial}{\partial x_1} & \frac{\partial}{\partial x_2}\end{pmatrix}, \tag{2.84}$$

$$\hat{\mathbf{A}}_{12}^{32} = -\begin{pmatrix}\frac{\partial}{\partial x_1}\\ \frac{\partial}{\partial x_2}\end{pmatrix}\frac{\hat{\rho}^E}{\hat{\epsilon}}\hat{\mathcal{L}}, \tag{2.85}$$

$$\hat{\mathbf{A}}_{12}^{33} = -j\omega\mu_0\mathbf{I}_2 + \begin{pmatrix}\frac{\partial}{\partial x_1}\\ \frac{\partial}{\partial x_2}\end{pmatrix}\frac{1}{j\omega\hat{\epsilon}}\begin{pmatrix}\frac{\partial}{\partial x_1} & \frac{\partial}{\partial x_2}\end{pmatrix}, \tag{2.86}$$

$$\hat{\mathbf{A}}_{21}^{11} = -j\omega\mathbf{C}_{33}^{-1}, \tag{2.87}$$

$$\hat{\mathbf{A}}_{21}^{12} = j\omega\frac{C}{M}\mathbf{C}_{33}^{-1}\boldsymbol{\delta}_3, \tag{2.88}$$

$$\hat{\mathbf{A}}_{21}^{21} = j\omega\frac{C}{M}\boldsymbol{\delta}_3^t\mathbf{C}_{33}^{-1}, \tag{2.89}$$

$$\hat{\mathbf{A}}_{21}^{22} = -j\omega\frac{C^2}{M^2}\boldsymbol{\delta}_3^t\mathbf{C}_{33}^{-1}\boldsymbol{\delta}_3 - \frac{j\omega}{M} + \frac{\partial}{\partial x_\beta}\left(\frac{\hat{k}}{\eta}\frac{\partial}{\partial x_\beta}\cdot\right), \tag{2.90}$$

$$\hat{\mathbf{A}}_{21}^{23} = -\frac{\partial}{\partial x_\beta}\hat{\mathcal{L}}\boldsymbol{\gamma}_\beta^t, \tag{2.91}$$

$$\hat{\mathbf{A}}_{21}^{32} = \hat{\mathcal{L}}\boldsymbol{\gamma}_\alpha\frac{\partial}{\partial x_\alpha}, \tag{2.92}$$

$$\hat{\mathbf{A}}_{21}^{33} = -j\omega\hat{\epsilon}\mathbf{I}_2 + \begin{pmatrix}\frac{\partial}{\partial x_2}\\ \frac{-\partial}{\partial x_1}\end{pmatrix}\frac{1}{j\omega\mu_0}\begin{pmatrix}\frac{\partial}{\partial x_2} & \frac{-\partial}{\partial x_1}\end{pmatrix} - \frac{\eta}{\hat{k}}\hat{\mathcal{L}}^2\boldsymbol{\gamma}_\alpha\boldsymbol{\gamma}_\alpha^t, \tag{2.93}$$

$$\hat{\mathbf{A}}_{22}^{11} = -\mathbf{C}_{33}^{-1}\mathbf{C}_{3\beta}\frac{\partial}{\partial x_\beta}, \tag{2.94}$$

$$\hat{\mathbf{A}}_{22}^{21} = \frac{\partial}{\partial x_\beta}(j\omega\rho^f \frac{\hat{k}}{\eta}\boldsymbol{\delta}_\beta^t) - \frac{C}{M}\mathbf{u}_\beta^t \frac{\partial}{\partial x_\beta}, \tag{2.95}$$

$$\hat{\mathbf{A}}_{22}^{31} = j\omega\rho^f \hat{\mathcal{L}}\boldsymbol{\gamma}_\alpha \boldsymbol{\delta}_\alpha^t. \tag{2.96}$$

2.5 Wave equation in matrix-vector form for the 2D case

We consider a medium consisting of horizontal layers of homogeneous porous media in which waves propagate only in the x_1, x_3-plane with the x_3-axis pointing downward. Consequently the derivatives with respect to x_2 are zero. In that case the previously defined matrix $\hat{\mathbf{A}}$ is simplified to

$$\hat{\mathbf{A}} = \begin{pmatrix} \hat{\mathbf{A}}_{11} & \hat{\mathbf{A}}_{12} \\ \hat{\mathbf{A}}_{21} & \hat{\mathbf{A}}_{22} \end{pmatrix}, \tag{2.97}$$

where

$$\hat{\mathbf{A}}_{11} = \begin{pmatrix} 0 & 0 & -\frac{\partial}{\partial x_1}\left(\frac{S}{K_c}\cdot\right) & \frac{\rho^f}{\hat{\rho}^E}\frac{\partial}{\partial x_1} - \frac{\partial}{\partial x_1}\left(\frac{2CG_{\mathrm{fr}}}{MK_c}\cdot\right) & -j\omega\rho^f\hat{\mathcal{L}} & 0 \\ 0 & 0 & 0 & 0 & 0 & -j\omega\rho^f\hat{\mathcal{L}} \\ -\frac{\partial}{\partial x_1} & 0 & 0 & 0 & 0 & 0 \\ 0 & 0 & 0 & 0 & 0 & 0 \\ 0 & 0 & 0 & 0 & 0 & 0 \\ 0 & 0 & 0 & 0 & 0 & 0 \end{pmatrix} \tag{2.98}$$

$$\hat{\mathbf{A}}_{12} = \begin{pmatrix} -j\omega(\rho^b - \frac{(\rho^f)^2}{\hat{\rho}^E}) + \frac{1}{j\omega}\frac{\partial}{\partial x_1}\left(\nu\frac{\partial}{\partial x_1}\cdot\right) & 0 \\ 0 & -j\omega(\rho^b - \frac{(\rho^f)^2}{\hat{\rho}^E}) + \frac{1}{j\omega}\frac{\partial}{\partial x_1}\left(G_{\mathrm{fr}}\frac{\partial}{\partial x_1}\cdot\right) \\ 0 & 0 \\ 0 & 0 \\ 0 & 0 \\ 0 & 0 \end{pmatrix}$$

$$\begin{pmatrix} 0 & 0 & 0 & 0 \\ 0 & 0 & 0 & 0 \\ -j\omega\rho^b & -j\omega\rho^f & 0 & 0 \\ -j\omega\rho^f & -\frac{\eta}{\hat{k}}\left(1+\frac{\hat{\rho}^E}{\hat{\epsilon}}\hat{\mathcal{L}}^2\right) & \frac{\hat{\rho}^E}{\hat{\epsilon}}\hat{\mathcal{L}}\frac{\partial}{\partial x_1} & 0 \\ 0 & -\frac{\partial}{\partial x_1}\left(\frac{\hat{\rho}^E}{\hat{\epsilon}}\hat{\mathcal{L}}\cdot\right) & -j\omega\mu_0+\frac{1}{j\omega}\frac{\partial}{\partial x_1}\left(\frac{1}{\hat{\epsilon}}\frac{\partial}{\partial x_1}\cdot\right) & 0 \\ 0 & 0 & 0 & -j\omega\mu_0 \end{pmatrix} \tag{2.99}$$

$$\hat{\mathbf{A}}_{21} = \begin{pmatrix} -\frac{j\omega}{G_{\rm fr}} & 0 & 0 & 0 \\ 0 & -\frac{j\omega}{G_{\rm fr}} & 0 & 0 \\ 0 & 0 & -\frac{j\omega}{K_c} & \frac{j\omega C}{MK_c} \\ 0 & 0 & \frac{j\omega C}{MK_c} & -j\omega\left(\frac{C^2}{M^2K_c}+\frac{1}{M}\right)+\frac{\partial}{\partial x_1}(\frac{\hat{k}}{\eta}\frac{\partial}{\partial x_1}\cdot) \\ 0 & 0 & 0 & \hat{\mathcal{L}}\frac{\partial}{\partial x_1} \\ 0 & 0 & 0 & 0 \end{pmatrix}$$

$$\begin{pmatrix} 0 & 0 \\ 0 & 0 \\ 0 & 0 \\ -\frac{\partial}{\partial x_1}(\hat{\mathcal{L}}\cdot) & 0 \\ -j\omega\epsilon-\frac{\eta}{\hat{k}}\hat{\mathcal{L}}^2 & 0 \\ 0 & -j\omega\epsilon-\frac{\eta}{\hat{k}}\hat{\mathcal{L}}^2+\frac{1}{j\omega}\frac{\partial}{\partial x_1}\left(\frac{1}{\mu_0}\frac{\partial}{\partial x_1}\cdot\right) \end{pmatrix} \tag{2.100}$$

$$\hat{\mathbf{A}}_{22} = \begin{pmatrix} 0 & 0 & -\frac{\partial}{\partial x_1} & 0 & 0 & 0 \\ 0 & 0 & 0 & 0 & 0 & 0 \\ -\left(\frac{S}{K_c}\right)\frac{\partial}{\partial x_1} & 0 & 0 & 0 & 0 & 0 \\ \frac{\partial}{\partial x_1}\left(\frac{\rho^f}{\hat{\rho^E}}\cdot\right)-\frac{2CG_{\rm fr}}{MK_c}\frac{\partial}{\partial x_1} & 0 & 0 & 0 & 0 & 0 \\ j\omega\rho^f\hat{\mathcal{L}} & 0 & 0 & 0 & 0 & 0 \\ 0 & j\omega\rho^f\hat{\mathcal{L}} & 0 & 0 & 0 & 0 \end{pmatrix} \tag{2.101}$$

where

$$\nu = 4G_{\rm fr}\left(\frac{S+G_{\rm fr}}{K_c}\right), \tag{2.102}$$

$$K_c = S + 2G_{\rm fr}. \tag{2.103}$$

and from equation (2.73) we have

$$\hat{\mathbf{D}} = \begin{pmatrix} \hat{\mathbf{f}}^b - j\omega\rho^f \frac{\hat{k}}{\eta}\boldsymbol{\delta}_\alpha \hat{f}^f_\alpha \\ -\frac{\hat{\rho}^E}{\hat{\epsilon}}\hat{\mathcal{L}}\hat{J}^e_3 + \hat{f}^f_3 \\ -\hat{\mathbf{J}}^m_0 - \begin{pmatrix} \frac{\partial}{\partial x_1} \\ 0 \end{pmatrix} \frac{1}{j\omega\hat{\epsilon}}\hat{J}^e_3 \\ \mathbf{0} \\ -\frac{\partial}{\partial x_1}\left(\frac{\hat{k}}{\eta}\hat{f}^f_1\right) \\ -\hat{\mathbf{J}}^e_0 - \begin{pmatrix} 0 \\ -\frac{\partial}{\partial x_1} \end{pmatrix} \frac{1}{j\omega\hat{\mu}_0}\hat{J}^m_3 - \hat{\mathcal{L}}\boldsymbol{\gamma}_\alpha \hat{f}^f_\alpha \end{pmatrix} \tag{2.104}$$

2.6 The A matrix in the (p_1, ω) domain

2.6.1 Generalized Radon transformation

We use the Radon transformation to decompose a two dimensional wavefield $u(x_1, x_3, \omega)$ into propagating and evanescent plane waves. The definition of the Radon transformation we will use in this thesis is

$$\mathcal{R}\left\{\hat{f}(x_1, x_3, \omega)\right\} = \tilde{f}(p_1, x_3, \omega) = \int_{-\infty}^{\infty} \hat{f}(x_1, x_3, \omega) e^{j\omega p_1 x_1} dx_1, \tag{2.105}$$

where p_1 is the ray parameter, which is a measure for the direction of propagation of a plane wave, according to

$$p_1 = \frac{\sin(\theta)}{c} \tag{2.106}$$

where θ is the propagation angle and c is the wave propagation velocity. Since we assume that the medium where the waves propagate is horizontally layered all derivatives with respect to x_2 vanish while the derivatives with respect to x_1 are replaced by $-j\omega p_1$. After the transformation these plane waves are described in the (p_1, ω) domain. Later through a Fourier transformation they will be expressed in the (p_1, τ) domain.

2.6.2 Rearrangement of the A matrix

In this section we show how from the previous matrix-vector equation two sets of independent equations representing two sets of independent wavefields decouple

completely. As it is known from Biot theory, fast and slow P waves couple together with vertically polarized shear waves, while horizontal shear waves do not couple with other wavefields. In the electro-kinetic effect we find that the transverse magnetic polarization (or TM mode) of the electromagnetic waves is coupled with the fast and slow P waves and the vertical shear waves into what is called the P-SV-TM coupling. Similarly the transverse electric polarization (or TE mode) of the electromagnetic waves is coupled with the horizontal shear wave into what is called the SH-TE coupling.

The uncoupling of the equations is achieved through a rearrangement of the vectors $\hat{\mathbf{Q}}$ and $\hat{\mathbf{D}}$, and the matrix $\hat{\mathbf{A}}$. Furthermore we transform the equations from the (x_1, ω) domain to the (p_1, ω) domain through a generalized Radon transformation in which the derivatives with respect to x_1 are replaced by $-j\omega p_1$. In the following expressions the quantities will be written with a tilde ($\tilde{}$) to denote the (p_1, ω) domain.

Hence the general wave equation in vector-matrix form in the (p, ω) domain is

$$\frac{\partial \tilde{\mathbf{Q}}}{\partial x_3} = \tilde{\mathbf{A}}\tilde{\mathbf{Q}} + \tilde{\mathbf{D}}, \tag{2.107}$$

and the vector $\tilde{\mathbf{Q}}$ is now arranged like

$$\tilde{\mathbf{Q}} = \begin{pmatrix} \tilde{\mathbf{Q}}_{\mathrm{H}} \\ \tilde{\mathbf{Q}}_{\mathrm{V}} \end{pmatrix}, \tag{2.108}$$

where $\tilde{\mathbf{Q}}_{\mathrm{H}}$ and $\tilde{\mathbf{Q}}_{\mathrm{V}}$ are

$$\tilde{\mathbf{Q}}_{\mathrm{H}} = (-\tilde{\tau}^b_{23}, -\tilde{H}_1, \tilde{E}_2, \tilde{v}^s_2)^t, \tag{2.109}$$

$$\tilde{\mathbf{Q}}_{\mathrm{V}} = (\tilde{v}^s_3, \tilde{w}_3, -\tilde{\tau}^b_{13}, \tilde{H}_2, \tilde{E}_1, -\tilde{\tau}^b_{33}, \tilde{p}, \tilde{v}^s_1)^t. \tag{2.110}$$

This new order in the vector-matrix equation results in a new and simpler arrangement of $\tilde{\mathbf{A}}$ that finally gives way to the uncoupling of the two sets of equations:

$$\tilde{\mathbf{A}} = j\omega \begin{bmatrix} \tilde{\mathbf{A}}_{\mathrm{H}} & \mathbf{0}_{4\times 8} \\ \mathbf{0}_{8\times 4} & \tilde{\mathbf{A}}_{\mathrm{V}} \end{bmatrix}, \tag{2.111}$$

where

$$\tilde{\mathbf{A}}_{\mathrm{H}} = \begin{pmatrix} \mathbf{0}_{2\times 2} & \tilde{\mathbf{A}}_{1,\mathrm{H}} \\ \tilde{\mathbf{A}}_{2,\mathrm{H}} & \mathbf{0}_{2\times 2} \end{pmatrix} \quad \text{and} \quad \tilde{\mathbf{A}}_{\mathrm{V}} = \begin{pmatrix} \mathbf{0}_{4\times 4} & \tilde{\mathbf{A}}_{1,\mathrm{V}} \\ \tilde{\mathbf{A}}_{2,\mathrm{V}} & \mathbf{0}_{4\times 4} \end{pmatrix}, \tag{2.112}$$

where

$$\tilde{\mathbf{A}}_{1,\mathrm{H}} = \begin{pmatrix} -\rho^f \hat{\mathcal{L}} & \frac{(\rho^f)^2}{\hat{\rho^E}} - \rho^b + p_1^2 G_{\mathrm{fr}} \\ -\hat{\epsilon} - \hat{\rho}^E \hat{\mathcal{L}}^2 + \frac{p_1^2}{\mu_0} & \rho^f \hat{\mathcal{L}} \end{pmatrix}, \quad \tilde{\mathbf{A}}_{2,\mathrm{H}} = \begin{pmatrix} 0 & -\mu_0 \\ -\frac{1}{G_{\mathrm{fr}}} & 0 \end{pmatrix}, \tag{2.113}$$

$$\tilde{\mathbf{A}}_{1,\mathrm{V}} = \begin{pmatrix} 0 & \frac{-1}{K_C} & \frac{C}{MK_C} & p_1 \frac{S}{K_C} \\ p_1 \hat{\mathcal{L}} & \frac{C}{MK_C} & \frac{p_1^2}{\hat{\rho}^E} - \frac{C^2 + MK_C}{M^2 K_C} & p_1 \left(\frac{2G_{\mathrm{fr}} C}{MK_C} - \frac{\rho^f}{\hat{\rho}^E} \right) \\ -\rho^f \hat{\mathcal{L}} & p_1 \frac{S}{K_C} & p_1 \left(\frac{2G_{\mathrm{fr}} C}{MK_C} - \frac{\rho^f}{\hat{\rho}^E} \right) & -\frac{\rho^f}{\hat{\rho}^E} - \rho^b - p_1^2 \nu \\ -\hat{\epsilon} - \hat{\rho}^E \hat{\mathcal{L}}^2 & 0 & -p_1 \hat{\mathcal{L}} & \rho^f \hat{\mathcal{L}} \end{pmatrix} \tag{2.114}$$

$$\tilde{\mathbf{A}}_{2,\mathrm{V}} = \begin{pmatrix} 0 & \frac{p_1 \hat{\mathcal{L}} \hat{\rho}^E}{\hat{\epsilon}} & 0 & \frac{p_1^2}{\hat{\epsilon}} - \mu_0 \\ -\rho^b & -\rho^f & p_1 & 0 \\ -\rho^f & -\hat{\rho}^E \left(\frac{\hat{\epsilon} + \hat{\rho}^E \hat{\mathcal{L}}^2}{\hat{\epsilon}} \right) & 0 & \frac{\hat{\rho}^E p_1 \hat{\mathcal{L}}}{\hat{\epsilon}} \\ p_1 & 0 & -\frac{1}{G_{\mathrm{fr}}} & 0 \end{pmatrix}, \tag{2.115}$$

where the parameters C, M, Δ are defined in equations (2.30-2.31), S in equation (2.47), and ν and K_c in equations (2.102-2.103). The subscripts V and H stand for the P-SV-TM and the SH-TE cases respectively.

Furthermore the source vector $\tilde{\mathbf{D}}$ also is rearranged as

$$\tilde{\mathbf{D}} = \begin{pmatrix} \tilde{\mathbf{D}}_{\mathrm{H}} \\ \tilde{\mathbf{D}}_{\mathrm{V}} \end{pmatrix}, \tag{2.116}$$

where $\tilde{\mathbf{D}}_{\mathrm{H}}$ and $\tilde{\mathbf{D}}_{\mathrm{V}}$ are

$$\tilde{\mathbf{D}}_{\mathrm{H}} = \left(\tilde{f}_2^b - \frac{\rho^f}{\rho^E} \tilde{f}_2^f, -\tilde{J}_2^e - \frac{p_1}{\mu_0} \tilde{J}_3^m - \hat{\mathcal{L}} \tilde{f}_2^f, \tilde{J}_1^m, 0 \right)^t, \tag{2.117}$$

$$\tilde{\mathbf{D}}_{\mathrm{V}} = \left(0, \frac{p_1}{\rho^E} \tilde{f}_1^f, \tilde{f}_1^b - \frac{\rho^f}{\rho^E} \tilde{f}_1^f, -\tilde{J}_1^e - \hat{\mathcal{L}} \tilde{f}_1^f, -\tilde{J}_2^m + \frac{p_1}{\hat{\epsilon}} J_3^e, \right.$$
$$\left. \tilde{f}_3^b - \frac{\rho^f}{\rho^E} \tilde{f}_3^f, -\frac{\rho^E}{\hat{\epsilon}} \hat{\mathcal{L}} \tilde{J}_3^e + \tilde{f}_3^f, 0 \right)^t. \tag{2.118}$$

2.7 Wave equation in matrix-vector form for the 1D case

We are going to study now the one dimensional version of the $\mathbf{A}_{\mathrm{H,V}}$ matrices . For normal incidence we know that $p_1 = 0$.

Substituting this on expressions (2.113) gives the following for matrix $\tilde{\mathbf{A}}_{\mathrm{H}}$

$$\tilde{\mathbf{A}}_{\mathrm{H}} = \begin{pmatrix} \mathbf{0}_{2\times 2} & \tilde{\mathbf{A}}_{1,\mathrm{H}} \\ \tilde{\mathbf{A}}_{2,\mathrm{H}} & \mathbf{0}_{2\times 2} \end{pmatrix} \tag{2.119}$$

$$\tilde{\mathbf{A}}_{1,\mathrm{H}} = \begin{pmatrix} -\rho^f \hat{\mathcal{L}} & \frac{(\rho^f)^2}{\hat{\rho^E}} - \rho^b \\ -\hat{\epsilon} - \hat{\rho}^E \hat{\mathcal{L}}^2 & \rho^f \hat{\mathcal{L}} \end{pmatrix}, \quad \tilde{\mathbf{A}}_{2,\mathrm{H}} = \begin{pmatrix} 0 & -\mu_0 \\ -\frac{1}{G_{\mathrm{fr}}} & 0 \end{pmatrix}, \tag{2.120}$$

and substituting $p_1 = 0$ into expressions (2.114-2.123) gives this matrix $\tilde{\mathbf{A}}_{\mathrm{V}}$

$$\tilde{\mathbf{A}}_{\mathrm{V}} = \begin{pmatrix} \mathbf{0}_{8\times 8} & \tilde{\mathbf{A}}_{1,\mathrm{V}} \\ \tilde{\mathbf{A}}_{2,\mathrm{V}} & \mathbf{0}_{8\times 8} \end{pmatrix}, \tag{2.121}$$

$$\tilde{\mathbf{A}}_{1,\mathrm{V}} = \begin{pmatrix} 0 & -\frac{1}{K_c} & \frac{C}{MK_c} & 0 \\ 0 & \frac{C}{MK_c} & -\frac{c^2}{M^2 K_c} - \frac{1}{M} & 0 \\ -\rho^f \hat{\mathcal{L}} & 0 & 0 & \frac{\rho^f}{\hat{\rho}^E} - \rho^b \\ -\hat{\epsilon} - \hat{\rho}^E \hat{\mathcal{L}}^2 & 0 & 0 & \rho^f \hat{\mathcal{L}} \end{pmatrix}, \tag{2.122}$$

$$\tilde{\mathbf{A}}_{2,\mathrm{V}} = \begin{pmatrix} 0 & 0 & 0 & -\mu_0 \\ -\rho^b & -\rho^f & 0 & 0 \\ -\rho^f & -\frac{\eta}{k}\left(1 + \frac{\hat{\rho}^E}{\hat{\epsilon}} \hat{\mathcal{L}}^2\right) & 0 & 0 \\ 0 & 0 & -\frac{1}{G_{\mathrm{fr}}} & 0 \end{pmatrix}, \tag{2.123}$$

Looking at these matrices we see that $\tilde{\mathbf{A}}_{\mathrm{V}}$ uncouples into two subcases: one containing the wavefields corresponding to the compressional waves, and a second containing the wavefields corresponding to the shear and electromagnetic waves.

$$\frac{\partial \tilde{\mathbf{Q}}_{\mathrm{V}}^{\mathrm{l,t}}}{\partial x_3} = \tilde{\mathbf{A}}_{\mathrm{V}}^{\mathrm{l,t}} \tilde{\mathbf{Q}}_{\mathrm{V}}^{\mathrm{l,t}} + \tilde{\mathbf{D}}_{\mathrm{V}}^{\mathrm{l,t}}, \tag{2.124}$$

$$\tilde{\mathbf{Q}}^{\mathrm{l}}_{\mathrm{V}} = (\tilde{v}^s_3, \tilde{w}_3, -\tilde{\tau}^b_{33}, \tilde{p})^t \text{ and } \tilde{\mathbf{Q}}^{\mathrm{t}}_{\mathrm{V}} = (-\tilde{\tau}^b_{13}, \tilde{H}_2, \tilde{E}_1, \tilde{v}^s_1)^t \tag{2.125}$$

$$\tilde{\mathbf{A}}^{\mathrm{l,t}}_{\mathrm{V}} = \begin{pmatrix} \mathbf{0}_{2\times 2} & \tilde{\mathbf{A}}^{\mathrm{l,t}}_{1,\mathrm{V}} \\ \tilde{\mathbf{A}}^{\mathrm{l,t}}_{2,\mathrm{V}} & \mathbf{0}_{2\times 2} \end{pmatrix}, \tag{2.126}$$

where

$$\tilde{\mathbf{A}}^{\mathrm{l}}_{1,\mathrm{V}} = \begin{pmatrix} -\frac{1}{K_c} & \frac{C}{MK_c} \\ \frac{C}{MK_c} & -\frac{C^2}{M^2K_c} - \frac{1}{M} \end{pmatrix} \text{ and } \tilde{\mathbf{A}}^{\mathrm{l}}_{2,\mathrm{V}} = \begin{pmatrix} -\rho^b & -\rho^f \\ -\rho^f & -\frac{\eta}{k}\left(1 + \frac{\hat{\rho}^E}{\hat{\epsilon}}\hat{\mathcal{L}}^2\right) \end{pmatrix} \tag{2.127}$$

and

$$\tilde{\mathbf{A}}^{\mathrm{t}}_{1,\mathrm{V}} = \begin{pmatrix} -\rho^f\hat{\mathcal{L}} & -\frac{\rho^f}{\hat{\rho^E}} - \rho^b \\ -\hat{\epsilon} - \sigma & \rho^f\hat{\mathcal{L}} \end{pmatrix} \text{ and } \quad \tilde{\mathbf{A}}^{\mathrm{t}}_{2,\mathrm{V}} = \begin{pmatrix} 0 & -\mu_0 \\ -\frac{1}{G_{\mathrm{fr}}} & 0 \end{pmatrix}. \tag{2.128}$$

The P-SV-TM coupling separates into two couplings, one containing the fast and slow-P waves, or P coupling and the other containing the vertical shear and TM electromagnetic waves, or SV-TM coupling. Note that $\tilde{\mathbf{A}}^{\mathrm{t}}_{\mathrm{V}}$ is identical to $\tilde{\mathbf{A}}_{\mathrm{H}}$, since for vertical propagation the SV-TM coupling is just a different orientation of the SH-TE coupling. The compressional and shear wavefields are completely uncoupled for normal incidence and the seismo-electric coupling takes place only among transversal waves (shear and electromagnetic waves). As the angle of incidence increases, so does the contribution of the compressional waves to the transversal waves in the P-SV-TM coupling. Although this is an unrealistic case, it gives insight in the coupling mechanism between different wavefields and its dependencies on the angle of incidence. For example, it explains why right below the source point there is no seismo-electric conversion taking place when using a P-wave source.

2.8 Conclusions

In this chapter we have obtained the wave equation for the coupled seismic and electromagnetic waves in a porous medium in the frequency domain for the 3D and 2D cases, and in the ray parameter domain for the 2D and 1D cases.

We have begun this chapter with Pride's equations for the coupled electromagnetics and acoustics of porous media in the frequency domain. Then we have

expressed the vertical variations of a chosen set of wavefields in terms of their lateral variation, and combined them into the following matrix-vector equation

$$\frac{\partial \hat{\mathbf{Q}}}{\partial x_3} = \hat{\mathbf{A}}\hat{\mathbf{Q}} + \hat{\mathbf{D}}. \tag{2.129}$$

This is done first for the 3D case in the frequency domain, and second for a 2D case where we consider a medium consisting of horizontally layered homogeneous media. In this situation all derivatives with respect to x_2 are taken zero, which simplifies dramatically the structure of matrix $\hat{\mathbf{A}}$ as shown in Section 2.5. At this point we see clearly how the wave equation separates into two uncoupled partial differential equations that will describe the two types of coupling found on the seismo-electric effect: the SH-TE and the P-SV-TM couplings. On the SH-TE coupling we have the horizontal shear waves coupled with the TE electromagnetic wave. In the P-SV-TM coupling we have the compressional (fast-P and slow-P) and the vertical shear waves coupled to the TM electromagnetic wave.

Next we Radon transformed the wave equation from the $(\mathbf{x}, \omega)$ domain to the (p_1, ω) domain. Here all derivatives with respect to x_1 are replaced by $-j\omega p_1$.

From the 2D wave equation in the ray parameter domain we derived the 1D wave equation in the same domain. In this wave equation we found that the P-SV-TM coupling uncouples into longitudinal (compressional) and transversal (shear and TM electromagnetic) wavefields, therefore for normal incidence the compressional waves do not couple with electromagnetic waves.

The final expression for the 2D case gives us a neat expression that will be used in the following chapter to develop the composition and decomposition operators and later the seismo-electric reflection coefficients.

Chapter 3

One way equations for the electrokinetic effect

3.1 Introduction

In this chapter we describe the one-way wave equations and how we move from two-way to one-way expressions. We describe an electro-kinetic survey by means of operators describing each of the phenomena taking place, such as excitation, propagation or reflection.

Finally we show examples of two cases where we apply the contents of this chapter, first a simple WRW reflection using just one-way quantities and second a more complex case including decomposition and composition at the source and receivers.

3.2 Decomposition of wavefields

In this section we introduce the composition and decomposition operators. We finished the previous chapter with the two-way wave equations for the two types of electro-kinetic coupling, the SH-TE and the P-SV-TM cases

$$\frac{\partial \tilde{\mathbf{Q}}_{\mathrm{H}}}{\partial x_3} = \tilde{\mathbf{A}}_{\mathrm{H}} \tilde{\mathbf{Q}}_{\mathrm{H}} + \tilde{\mathbf{D}}_{\mathrm{H}}, \tag{3.1}$$

$$\frac{\partial \tilde{\mathbf{Q}}_{\mathrm{V}}}{\partial x_3} = \tilde{\mathbf{A}}_{\mathrm{V}} \tilde{\mathbf{Q}}_{\mathrm{V}} + \tilde{\mathbf{D}}_{\mathrm{V}}. \tag{3.2}$$

In this chapter we show the method of transforming two-way field quantities into one-way wavefields via the composition operator $\tilde{\mathbf{L}}$.

As shown in the previous chapter there are two types of electro-kinetic coupling, SH-TE and P-SV-TM. We look at these couplings separately and derive expressions for the composition operators.

3.2.1 Composition operator

The wave field represented by vector $\tilde{\mathbf{Q}}$ in equations (3.1-3.2) is decomposed in downgoing and upgoing wavefields by using the transformation

$$\tilde{\mathbf{Q}} = \tilde{\mathbf{L}}\tilde{\mathbf{P}}, \tag{3.3}$$

where matrix $\tilde{\mathbf{L}}$ is the composition operator that converts the one-way wavefields into two-way wavefields. One-way wave equations describe the propagation of a certain wave (e.g. fast-P wave) across the medium either up or downgoing, while two-way wave equations describe the propagation of a certain field quantity (e.g. E_1 field) up and downgoing.

We see in equation (3.3) how the operator $\tilde{\mathbf{L}}$ composes the field quantities present in $\tilde{\mathbf{Q}}$ from the up and downgoing one-way wavefields contained in $\tilde{\mathbf{P}}$.

The composition operator contains the eigenvectors of matrix $\tilde{\mathbf{A}}$

$$\tilde{\mathbf{A}} = \tilde{\mathbf{L}}\tilde{\mathbf{\Lambda}}\tilde{\mathbf{L}}^{-1}. \tag{3.4}$$

Substituting (3.3) and (3.4) into (3.1) or (3.2) and assuming that there are no vertical variations of the medium parameters in a layer, we obtain

$$\frac{\partial\tilde{\mathbf{P}}}{\partial x_3} = \tilde{\mathbf{\Lambda}}\tilde{\mathbf{P}} + \tilde{\mathbf{L}}^{-1}\tilde{\mathbf{D}}. \tag{3.5}$$

which shows the vertical variation of the one-way wavefields present in $\tilde{\mathbf{D}}$ as a function of the eigenvalues of $\tilde{\mathbf{A}}$ and the one-way source.

3.2.2 Coupling between SH-waves and TE-waves

When a horizontally polarized shear wave (SH-mode) propagates in the x_1-x_3 plane, its propagation is not coupled to the other three seismic wavefields (the fast and slow P-waves and the vertically polarized shear wave); however, the SH-wave generates electric currents in the x_2-direction and these currents couple to the electromagnetic wavefield with transverse electric polarization (TE-mode).

Wave velocities

The system matrix $\tilde{\mathbf{A}}_{\mathrm{H}}$ in Eq. (3.1) can be used to determine the velocities of the SH-wave and TE-wave in a homogeneous porous layer. Since the medium is isotropic, we consider the special case of a horizontally propagating wave with velocity $c=1/p_1$. For this specific case the left hand side of Eq. (3.1) becomes zero (i.e., there is no x_3-dependency) and the non-trivial solution for the resulting linear set of equations is the one for which the determinant $\left|\tilde{\mathbf{A}}_{\mathrm{H}}\right| = \left|\tilde{\mathbf{A}}_{1,\,\mathrm{H}}\right| \left|\tilde{\mathbf{A}}_{2,\,\mathrm{H}}\right|$ vanishes. Consequently, since $\left|\tilde{\mathbf{A}}_{2,\,\mathrm{H}}\right| \neq 0$, one simply has to find a horizontal slowness $p_1 = 1/c$ for which $\left|\tilde{\mathbf{A}}_{1,\,\mathrm{H}}\right|$ is zero. We thus obtain

$$\frac{2}{c^2} = \frac{\rho_{\mathrm{B}} - \rho_{\mathrm{f}}^2/\hat{\rho}_{\mathrm{E}}}{\hat{G}} + (\hat{\varepsilon} + \hat{\rho}_{\mathrm{E}}\hat{\mathcal{L}}^2)\mu \pm \sqrt{\left(\frac{\rho_{\mathrm{B}} - \rho_{\mathrm{f}}^2/\hat{\rho}_{\mathrm{E}}}{G} - (\hat{\varepsilon} + \hat{\rho}_{\mathrm{E}}\hat{\mathcal{L}}^2)\mu\right)^2 - 4\frac{\mu\rho_{\mathrm{f}}^2\hat{\mathcal{L}}^2}{G}}, \quad (3.6)$$

where the plus sign is associated with the velocity of the SH-wave (denoted by c_{sh}) and the minus sign with the velocity of the TE-wave (denoted by c_{te}).

Composition operator

As previously said, the wave field represented by vector $\tilde{\mathbf{Q}}_{\mathrm{H}}$ in Eq. (3.1) is decomposed in downgoing and upgoing wavefields by using the transformation $\tilde{\mathbf{Q}}_{\mathrm{H}} = \tilde{\mathbf{L}}_{\mathrm{H}}\tilde{\mathbf{P}}_{\mathrm{H}}$. By using the results of [19], we find that matrix $\tilde{\mathbf{L}}_{\mathrm{H}}$ is given by $\tilde{\mathbf{L}}_{\mathrm{H}} = j\omega\left(\tilde{\mathbf{a}}_{\mathrm{sh}}^{+},\, \tilde{\mathbf{a}}_{\mathrm{te}}^{+},\, \tilde{\mathbf{a}}_{\mathrm{sh}}^{-},\, \tilde{\mathbf{a}}_{\mathrm{te}}^{-}\right)$, in which

$$\tilde{\mathbf{a}}_{\mathrm{n}}^{\pm} = \begin{pmatrix} \mp\tilde{q}_{\mathrm{n}}G \\ \pm\tilde{q}_{\mathrm{n}}\hat{\gamma}_{\mathrm{n}} \\ -\mu\hat{\gamma}_{\mathrm{n}} \\ 1 \end{pmatrix} \quad \text{with} \quad \hat{\gamma}_{\mathrm{n}} = \frac{\hat{\mathcal{L}}\hat{\rho}_{\mathrm{E}}(G - \rho_{\mathrm{B}}c_{\mathrm{n}}^2)}{\hat{\varepsilon}\mu\rho_{\mathrm{f}}c_{\mathrm{n}}^2 - \rho_{\mathrm{f}}}, \quad \text{where} \quad \mathrm{n}=\{\mathrm{sh,te}\}. \quad (3.7)$$

Here, $\tilde{q}_{\mathrm{n}}$ represents the two vertical slownesses belonging to the SH-wave and TE-wave and it is defined as

$$p_1^2 + \tilde{q}_{\mathrm{n}}^2 = 1/c_{\mathrm{n}}^2 \text{ with } \mathrm{Im}(\tilde{q}_{\mathrm{n}}) < 0 \quad (3.8)$$

hence, by combining Eq. (3.1) with the relation

$$\tilde{\mathbf{L}}_{\mathrm{H}}^{-1}\tilde{\mathbf{A}}_{\mathrm{H}}\tilde{\mathbf{L}}_{\mathrm{H}} = \mathrm{diag}(-\tilde{q}_{\mathrm{sh}},\, -\tilde{q}_{\mathrm{te}},\, \tilde{q}_{\mathrm{sh}},\, \tilde{q}_{\mathrm{te}}) \quad (3.9)$$

one finds in a homogeneous porous layer

$$\tilde{\mathbf{P}}_{\mathrm{H}} = \begin{pmatrix} \tilde{\mathbf{P}}_{\mathrm{H}}^{+} \\ \tilde{\mathbf{P}}_{\mathrm{H}}^{-} \end{pmatrix} \quad \text{with} \quad \tilde{\mathbf{P}}_{\mathrm{H}}^{\pm} = \begin{pmatrix} \hat{d}_{\mathrm{sh}}^{\pm} \exp(\mp j\omega\tilde{q}_{\mathrm{sh}} x_3) \\ \hat{d}_{\mathrm{te}}^{\pm} \exp(\mp j\omega\tilde{q}_{\mathrm{te}} x_3) \end{pmatrix} \tag{3.10}$$

where $\tilde{\mathbf{P}}_{\mathrm{H}}^{+}$ and $\tilde{\mathbf{P}}_{\mathrm{H}}^{-}$ are the downgoing and the upgoing wavefield, respectively.

3.2.3 Coupling between fast and slow P-waves, SV-waves, and TM-waves

When a fast P-wave, a slow P-wave, or a vertically polarized shear wave (SV-mode) propagates in the x_1-x_3 plane, it generates electric currents in the x_1-x_3 plane and these currents couple to the electromagnetic wavefield with transverse magnetic polarization (TM-mode).

Wave velocities

Similar to the SH-TE-case in the previous section, the system matrix $\tilde{\mathbf{A}}_{\mathrm{V}}$ can be used to determine the velocities of the fast and slow P-waves, SV-wave and TM-wave: find a horizontal slowness $p_1 = 1/c$ for which $\left|\tilde{\mathbf{A}}_{1,\,\mathrm{V}}\right| \left|\tilde{\mathbf{A}}_{2,\,\mathrm{V}}\right| = 0$. As expected, the solution for $\left|\tilde{\mathbf{A}}_{2,\,\mathrm{V}}\right| = 0$ results in velocities for the SV-wave and TM-wave as given in Eq. (3.6), in which the plus and minus sign are associated with the SV-wave (c_{s}) and TM-wave (c_{tm}), respectively. On the other hand, the solution for $\left|\tilde{\mathbf{A}}_{1,\,\mathrm{V}}\right| = 0$ results in [19]

$$\frac{2}{c^2} = \hat{\nu} \pm \sqrt{\hat{\nu}^2 - \frac{4}{\Delta}\left(\frac{(\hat{\varepsilon} + \hat{\rho}_{\mathrm{E}}\hat{\mathcal{L}}^2)\hat{\rho}_{\mathrm{E}}\rho_{\mathrm{B}}}{\hat{\varepsilon}} - \rho_{\mathrm{f}}^2\right)}, \tag{3.11}$$

where $\hat{\nu}$ is

$$\hat{\nu} = \rho_{\mathrm{B}}\frac{M}{\Delta} + \frac{(\hat{\varepsilon} + \hat{\rho}_{\mathrm{E}}\hat{\mathcal{L}}^2)\hat{\rho}_{\mathrm{E}}}{\hat{\varepsilon}}\frac{H}{\Delta} - 2\rho_{\mathrm{f}}\frac{C}{\Delta}, \tag{3.12}$$

Δ is defined in equation (2.32), and $H = K_G + 4G_{\mathrm{fr}}/3$. The $\pm$ sign in equation (5.4) denotes from which wavefield is c the velocity. The plus is associated with the velocity of the slow P-wave (denoted by c_{ps}) and the minus sign is associated with the velocity of the fast P-wave (denoted by c_{pf}).

Composition operator

Similar to the SH-TE-case in the previous section, the vector $\tilde{\mathbf{Q}}_{\mathrm{V}}$ in Eq. (3.2) is transformed as $\tilde{\mathbf{Q}}_{\mathrm{V}} = \tilde{\mathbf{L}}_{\mathrm{V}}\tilde{\mathbf{P}}_{\mathrm{V}}$. By using the results of [19], we find that $\tilde{\mathbf{L}}_{\mathrm{V}} = j\omega\left(\tilde{\mathbf{b}}^{+}_{\mathrm{pf}},\ \tilde{\mathbf{b}}^{+}_{\mathrm{ps}},\ \tilde{\mathbf{b}}^{+}_{\mathrm{sv}},\ \tilde{\mathbf{b}}^{+}_{\mathrm{tm}},\ \tilde{\mathbf{b}}^{-}_{\mathrm{pf}},\ \tilde{\mathbf{b}}^{-}_{\mathrm{ps}},\ \tilde{\mathbf{b}}^{-}_{\mathrm{sv}},\ \tilde{\mathbf{b}}^{-}_{\mathrm{tm}}\right)$ where

$$\tilde{\mathbf{b}}^{\pm}_{\mathrm{m}} = \begin{pmatrix} \pm\tilde{q}_{\mathrm{m}}c_{\mathrm{m}} \\ \pm\tilde{q}_{\mathrm{m}}c_{\mathrm{m}}\hat{\gamma}_{\mathrm{m}} \\ \mp 2p_1\tilde{q}_{\mathrm{m}}c_{\mathrm{m}}G \\ 0 \\ -(p_1c_{\mathrm{m}}\hat{\gamma}_{\mathrm{m}}\hat{\rho}_{\mathrm{E}}\hat{\mathcal{L}})/\hat{\varepsilon} \\ (2Gp_1^2c_{\mathrm{m}}^2 - H - \hat{\gamma}_{\mathrm{m}}C)/c_{\mathrm{m}} \\ -(C + \hat{\gamma}_{\mathrm{m}}M)/c_{\mathrm{m}} \\ p_1c_{\mathrm{m}} \end{pmatrix}, \qquad \tilde{\mathbf{b}}^{\pm}_{\mathrm{n}} = \begin{pmatrix} \pm p_1c_{\mathrm{n}} \\ \pm p_1(G - \rho_{\mathrm{B}}c_{\mathrm{n}}^2)/(c_{\mathrm{n}}\rho_{\mathrm{f}}) \\ \pm c_{\mathrm{n}}(\tilde{q}_{\mathrm{n}}^2 - p_1^2)G \\ \pm\hat{\gamma}_{\mathrm{n}}/c_{\mathrm{n}} \\ \mu\tilde{q}_{\mathrm{n}}c_{\mathrm{n}}\hat{\gamma}_{\mathrm{n}} \\ -2p_1\tilde{q}_{\mathrm{n}}c_{\mathrm{n}}G \\ 0 \\ -\tilde{q}_{\mathrm{n}}c_{\mathrm{n}} \end{pmatrix}, \tag{3.13}$$

where $\hat{\gamma}_{\mathrm{n}}$ is defined in Eq. (3.7) with $\mathrm{n}=\{\mathsf{sv,tm}\}$, and $\hat{\gamma}_{\mathrm{m}}$ is

$$\hat{\gamma}_{\mathrm{m}} = \frac{H - \rho_{\mathrm{B}}c_{\mathrm{m}}^2}{\rho_{\mathrm{f}}c_{\mathrm{m}}^2 - C} \qquad \text{with} \qquad \mathrm{m}=\{\mathsf{pf,\ ps}\}. \tag{3.14}$$

Here, $\tilde{q}_{\mathrm{n}}$ and $\tilde{q}_{\mathrm{m}}$ represent the four vertical slownesses belonging to the SV-wave, TM-wave, fast P-wave and slow P-wave, and they are defined as

$$p_1^2 + \tilde{q}_{\mathrm{m,n}}^2 = 1/c_{\mathrm{m,n}}^2 \text{ with } \mathrm{Im}(\tilde{q}_{\mathrm{m,n}}) < 0. \tag{3.15}$$

Note that $\pm\tilde{q}_{\mathrm{m,n}}$ are the eigenvalues of $\tilde{\mathbf{A}}_{\mathrm{V}}$; hence, by combining Eq. (3.2) with the relation

$$\tilde{\mathbf{L}}_{\mathrm{V}}^{-1}\tilde{\mathbf{A}}_{\mathrm{V}}\tilde{\mathbf{L}}_{\mathrm{V}} = \mathsf{diag}(-\tilde{q}_{\mathrm{pf}},\ -\tilde{q}_{\mathrm{ps}},\ -\tilde{q}_{\mathrm{sv}},\ -\tilde{q}_{\mathrm{tm}},\ \tilde{q}_{\mathrm{pf}},\ \tilde{q}_{\mathrm{ps}},\ \tilde{q}_{\mathrm{sv}},\ \tilde{q}_{\mathrm{tm}}) \tag{3.16}$$

one finds in a homogeneous porous layer

$$\tilde{\mathbf{P}}_{\mathrm{V}} = \begin{pmatrix} \tilde{\mathbf{P}}_{\mathrm{V}}^{+} \\ \tilde{\mathbf{P}}_{\mathrm{V}}^{-} \end{pmatrix} \quad \text{with} \quad \tilde{\mathbf{P}}_{\mathrm{V}}^{\pm} = \begin{pmatrix} \hat{d}_{\mathrm{pf}}^{\pm}\exp(\mp j\omega\tilde{q}_{\mathrm{pf}}x_3) \\ \hat{d}_{\mathrm{ps}}^{\pm}\exp(\mp j\omega\tilde{q}_{\mathrm{ps}}x_3) \\ \hat{d}_{\mathrm{sv}}^{\pm}\exp(\mp j\omega\tilde{q}_{\mathrm{sv}}x_3) \\ \hat{d}_{\mathrm{tm}}^{\pm}\exp(\mp j\omega\tilde{q}_{\mathrm{tm}}x_3) \end{pmatrix}. \tag{3.17}$$

3.3 Reflection and transmission coefficients

In the following section we derive the reflection and transmission coefficients from the boundary conditions of the interface. We will consider two types of interfaces: porous-porous and porous-vacuum. The first will simulate an interface between two layers in the subsurface while the second will simulate the surface of the earth.

3.3.1 Reflection and transmission coefficients for the porous/ porous interface

In this section we derive a general expression for the reflection and transmission coefficients of the SH-TE and P-SV-TM couplings. At the end of the section each particular case is described in detail. This method will be used later to obtain the coefficients for a porous/vacuum interface.

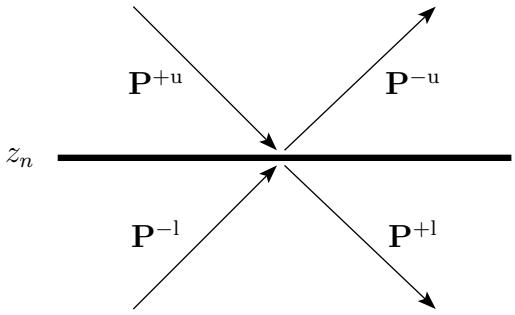

Figure 3.1: *Wavefields incoming and outgoing to an interface. The sign denotes the direction of the wavefield, and the superscripts ^{u} and ^{l} denote the upper and lower media respectively.*

The coefficients for both coupling cases are derived via the scattering matrix. This matrix relates the incoming wavefield to the outgoing wavefield by means of the reflection and transmission coefficients of that interface

$$\tilde{\mathbf{P}}^{\mathrm{out}} = \tilde{\mathbf{S}}\tilde{\mathbf{P}}^{\mathrm{in}}, \tag{3.18}$$

or

$$\begin{pmatrix} \mathbf{P}^{-u} \\ \mathbf{P}^{+\mathrm{l}} \end{pmatrix} = \begin{pmatrix} \tilde{\mathbf{r}}^{+} & \tilde{\mathbf{t}}^{-} \\ \tilde{\mathbf{t}}^{+} & \tilde{\mathbf{r}}^{-} \end{pmatrix} \begin{pmatrix} \mathbf{P}^{+\mathrm{u}} \\ \mathbf{P}^{-\mathrm{l}} \end{pmatrix} \tag{3.19}$$

where the left hand side of the equation contains the outgoing wavefields from the interface, and the right hand side contains the scattering matrix times the wavefields incoming to the interface.

In order to solve the equations of the system (3.19) we need the boundary conditions from Deresiewicz and Skalak [5] presented in section 1.3. At an interface the boundary conditions require that the elements of $\tilde{\mathbf{Q}}$ are equal at both sides,

$$\tilde{\mathbf{Q}}^{\mathrm{u}} = \tilde{\mathbf{Q}}^{\mathrm{l}}, \tag{3.20}$$

Substituting equation (3.3) into equation (3.20) gives

$$\tilde{\mathbf{L}}^{\mathrm{u}}\tilde{\mathbf{P}}^{\mathrm{u}} = \tilde{\mathbf{L}}^{\mathrm{l}}\tilde{\mathbf{P}}^{\mathrm{l}}, \tag{3.21}$$

and substituting equation (3.17) into the previous yields

$$\tilde{\mathbf{L}}^{\mathrm{u}} \begin{pmatrix} \tilde{\mathbf{P}}^{+\mathrm{u}} \\ \tilde{\mathbf{P}}^{-\mathrm{u}} \end{pmatrix} = \tilde{\mathbf{L}}^{\mathrm{l}} \begin{pmatrix} \tilde{\mathbf{P}}^{+\mathrm{l}} \\ \tilde{\mathbf{P}}^{-\mathrm{l}} \end{pmatrix}. \tag{3.22}$$

For this derivation we express $\tilde{\mathbf{L}}^{\mathrm{u,l}}$ in terms of the eigenvalues corresponding to down and upgoing wavefields respectively

$$\tilde{\mathbf{L}}_{\mathrm{a}}^{\mathrm{u,l}} = j\omega \begin{pmatrix} \tilde{\mathbf{a}}_{\mathrm{a}}^{+\mathrm{u,l}} & \tilde{\mathbf{a}}_{\mathrm{a}}^{-\mathrm{u,l}} \end{pmatrix}, \text{ where } \mathrm{a} = \{\mathrm{H}, \mathrm{V}\} \tag{3.23}$$

for the SH-TE coupling

$$\tilde{\mathbf{a}}_{\mathrm{H}}^{\pm\mathrm{u,l}} = \begin{pmatrix} \tilde{\mathbf{a}}_{\mathrm{sh}}^{\pm\mathrm{u,l}} & \tilde{\mathbf{a}}_{\mathrm{te}}^{\pm\mathrm{u,l}} \end{pmatrix}, \tag{3.24}$$

and for the P-SV-TM coupling

$$\tilde{\mathbf{a}}_{\mathrm{V}}^{\pm\mathrm{u,l}} = \begin{pmatrix} \tilde{\mathbf{a}}_{\mathrm{pf}}^{\pm\mathrm{u,l}} & \tilde{\mathbf{a}}_{\mathrm{ps}}^{\pm\mathrm{u,l}} & \tilde{\mathbf{a}}_{\mathrm{sv}}^{\pm\mathrm{u,l}} & \tilde{\mathbf{a}}_{\mathrm{tm}}^{\pm\mathrm{u,l}} \end{pmatrix}. \tag{3.25}$$

The columns of the composition operators $\tilde{\mathbf{L}}_{\mathrm{a}}^{\mathrm{u,l}}$ are defined in equations (3.7) and (3.13). Substituting equations (3.23) into (3.22) gives

$$\mathbf{Q}^{\mathrm{u}} = j\omega \begin{pmatrix} \tilde{\mathbf{a}}^{+\mathrm{u}} & \tilde{\mathbf{a}}^{-\mathrm{u}} \end{pmatrix} \begin{pmatrix} \mathbf{P}^{+\mathrm{u}} \\ \mathbf{P}^{-\mathrm{u}} \end{pmatrix} = j\omega \left(\tilde{\mathbf{a}}^{+\mathrm{u}}\mathbf{P}^{+\mathrm{u}} + \tilde{\mathbf{a}}^{-\mathrm{u}}\mathbf{P}^{-\mathrm{u}} \right), \tag{3.26}$$

and

$$\mathbf{Q}^{\mathrm{l}} = j\omega \begin{pmatrix} \tilde{\mathbf{a}}^{+\mathrm{l}} & \tilde{\mathbf{a}}^{-\mathrm{l}} \end{pmatrix} \begin{pmatrix} \mathbf{P}^{+\mathrm{l}} \\ \mathbf{P}^{-\mathrm{l}} \end{pmatrix} = j\omega \left(\tilde{\mathbf{a}}^{+\mathrm{l}}\mathbf{P}^{+\mathrm{l}} + \tilde{\mathbf{a}}^{-\mathrm{l}}\mathbf{P}^{-\mathrm{l}} \right). \tag{3.27}$$

According to the boundary conditions (3.20), $\mathbf{Q}^{\mathrm{u}}$ in equation (3.26) and $\mathbf{Q}^{\mathrm{l}}$ in equation (3.27) must be equal, hence

$$\tilde{\mathbf{a}}^{+\mathrm{u}}\mathbf{P}^{+\mathrm{u}} + \tilde{\mathbf{a}}^{-\mathrm{u}}\mathbf{P}^{-\mathrm{u}} = \tilde{\mathbf{a}}^{+\mathrm{l}}\mathbf{P}^{+\mathrm{l}} + \tilde{\mathbf{a}}^{-\mathrm{l}}\mathbf{P}^{-\mathrm{l}}, \tag{3.28}$$

this equation can be rearranged as

$$\tilde{\mathbf{a}}^{-\mathrm{u}}\mathbf{P}^{-\mathrm{u}} - \tilde{\mathbf{a}}^{+\mathrm{l}}\mathbf{P}^{+\mathrm{l}} = -\tilde{\mathbf{a}}^{+\mathrm{u}}\mathbf{P}^{+\mathrm{u}} + \tilde{\mathbf{a}}^{-\mathrm{l}}\mathbf{P}^{-\mathrm{l}}, \tag{3.29}$$

where the left hand side of the equation contains the wavefields incoming to the interface while the right hand side contains the outgoing wavefields. Rewriting things back to the notation of equation (3.26), we get

$$\underbrace{\begin{pmatrix}\tilde{\mathbf{a}}^{-\mathrm{u}} & -\tilde{\mathbf{a}}^{+\mathrm{l}}\end{pmatrix}}_{\tilde{\mathbf{S}}_1}\begin{pmatrix}\mathbf{P}^{-\mathrm{u}}\\ \mathbf{P}^{+\mathrm{l}}\end{pmatrix} = \underbrace{\begin{pmatrix}-\tilde{\mathbf{a}}^{+\mathrm{u}} & \tilde{\mathbf{a}}^{-\mathrm{l}}\end{pmatrix}}_{\tilde{\mathbf{S}}_2}\begin{pmatrix}\mathbf{P}^{+\mathrm{u}}\\ \mathbf{P}^{-\mathrm{l}}\end{pmatrix}. \tag{3.30}$$

Comparing equation (3.30) with (3.19) gives the following expression for the scattering matrix.

$$\tilde{\mathbf{S}} = \tilde{\mathbf{S}}_1^{-1}\tilde{\mathbf{S}}_2 = \begin{pmatrix}\tilde{\mathbf{r}}^{+} & \tilde{\mathbf{t}}^{-}\\ \tilde{\mathbf{t}}^{+} & \tilde{\mathbf{r}}^{-}\end{pmatrix}. \tag{3.31}$$

Each of the elements of $\tilde{\mathbf{S}}$ is a matrix that will have the form

$$\tilde{\mathbf{r}}^{\pm}_{\mathrm{H}} = \begin{pmatrix}\tilde{r}^{\pm}_{\mathrm{sh,sh}} & \tilde{r}^{\pm}_{\mathrm{sh,te}}\\ \tilde{r}^{\pm}_{\mathrm{te,sh}} & \tilde{r}^{\pm}_{\mathrm{te,te}}\end{pmatrix}, \tilde{\mathbf{t}}^{\pm}_{\mathrm{H}} = \begin{pmatrix}\tilde{t}^{\pm}_{\mathrm{sh,sh}} & \tilde{t}^{\pm}_{\mathrm{sh,te}}\\ \tilde{t}^{\pm}_{\mathrm{te,sh}} & \tilde{t}^{\pm}_{\mathrm{te,te}}\end{pmatrix} \tag{3.32}$$

and

$$\tilde{\mathbf{r}}^{\pm}_{\mathrm{V}} = \begin{pmatrix}\tilde{r}^{\pm}_{\mathrm{pf,pf}} & \tilde{r}^{\pm}_{\mathrm{pf,ps}} & \tilde{r}^{\pm}_{\mathrm{pf,sv}} & \tilde{r}^{\pm}_{\mathrm{pf,tm}}\\ \tilde{r}^{\pm}_{\mathrm{ps,pf}} & \tilde{r}^{\pm}_{\mathrm{ps,ps}} & \tilde{r}^{\pm}_{\mathrm{ps,sv}} & \tilde{r}^{\pm}_{\mathrm{ps,tm}}\\ \tilde{r}^{\pm}_{\mathrm{sv,pf}} & \tilde{r}^{\pm}_{\mathrm{sv,ps}} & \tilde{r}^{\pm}_{\mathrm{sv,sv}} & \tilde{r}^{\pm}_{\mathrm{sv,tm}}\\ \tilde{r}^{\pm}_{\mathrm{tm,pf}} & \tilde{r}^{\pm}_{\mathrm{tm,ps}} & \tilde{r}^{\pm}_{\mathrm{tm,sv}} & \tilde{r}^{\pm}_{\mathrm{tm,tm}}\end{pmatrix}, \tag{3.33}$$

$$\tilde{\mathbf{t}}^{\pm}_{\mathrm{V}} = \begin{pmatrix}\tilde{t}^{\pm}_{\mathrm{pf,pf}} & \tilde{t}^{\pm}_{\mathrm{pf,ps}} & \tilde{t}^{\pm}_{\mathrm{pf,sv}} & \tilde{t}^{\pm}_{\mathrm{pf,tm}}\\ \tilde{t}^{\pm}_{\mathrm{ps,pf}} & \tilde{t}^{\pm}_{\mathrm{ps,ps}} & \tilde{t}^{\pm}_{\mathrm{ps,sv}} & \tilde{t}^{\pm}_{\mathrm{ps,tm}}\\ \tilde{t}^{\pm}_{\mathrm{sv,pf}} & \tilde{t}^{\pm}_{\mathrm{sv,ps}} & \tilde{t}^{\pm}_{\mathrm{sv,sv}} & \tilde{t}^{\pm}_{\mathrm{sv,tm}}\\ \tilde{t}^{\pm}_{\mathrm{tm,pf}} & \tilde{t}^{\pm}_{\mathrm{tm,ps}} & \tilde{t}^{\pm}_{\mathrm{tm,sv}} & \tilde{t}^{\pm}_{\mathrm{tm,tm}}\end{pmatrix}, \tag{3.34}$$

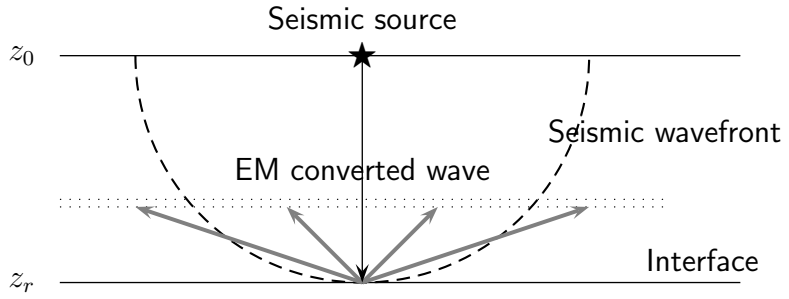

Figure 3.2: *The conversion from seismic to electromagnetic takes place when the seismic wavefront touches the interface, and from that point the electromagnetic wave is generated to all the points at the surface.*

where for example $r^{+}_{\mathrm{tm,sv}}$ is the reflection coefficient for an downgoing incoming vertically polarized shear wave and outgoing TM mode electromagnetic wave.

Results

In the first half of this section we have derived the expressions for the reflection and transmission coefficients for the seismo-electric effect, in this subsection we make use of those expressions and show certain cases as examples.

We calculate all the reflection coefficients of the same type of interface: a contrast in porosity, permeability and pore fluid ion concentration between the upper and lower media. The medium parameters can be found in Table 3.1.

Parameter	Upper medium	Lower medium
ϕ	0.4	0.2
k	$1.28 \cdot 10^{-12}$	$1.6 \cdot 10^{-13}$
C	10^{-6}	10^{-2}
K^s	$4 \cdot 10^{10}$	$4 \cdot 10^{10}$
K^{fr}	$4 \cdot 10^{9}$	$4 \cdot 10^{9}$
G^{fr}	$9 \cdot 10^{9}$	$9 \cdot 10^{9}$

Table 3.1: *medium parameters*

In Figure 3.2 we see how the conversion from seismic to electromagnetic waves takes place in a very small area around normal incidence when the seismic

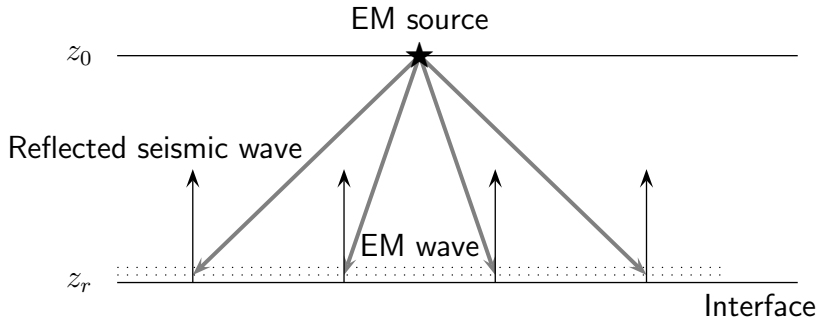

Figure 3.3: *When an electromagnetic source is used, the wave reaches instantaneously to all the points in the interface, that after conversion act as seismic sources generating an upgoing inhomogeneous plane wave.*

wavefront touches the horizontal interface. If we look at Snell's law

$$\frac{\sin\theta_{\mathrm{s}}}{c_{\mathrm{s}}} = \frac{\sin\theta_{\mathrm{em}}}{c_{\mathrm{em}}} \tag{3.35}$$

where the subscripts $_{\mathrm{s}}$ and $_{\mathrm{em}}$ stand for seismic and electromagnetic respectively, we see that since the electromagnetic velocity c_{em} is much higher than the seismic velocity c_{s} the critical angle for the incident seismic wave

$$\theta_{\mathrm{s}}^{\mathrm{c}} = \arcsin\left(\frac{c_{\mathrm{s}}}{c_{\mathrm{em}}}\right), \tag{3.36}$$

is very small, in the order of 10^{-3}. This means that for any angle of incidence $\theta_{\mathrm{s}} > \theta_{\mathrm{s}}^{\mathrm{c}}$ the reflected and transmitted wavefields are going to be evanescent. Only when there is normal incidence there is a generation of homogeneous electromagnetic wavefields.

Figure 3.3 shows a scheme of the reflection of seismic waves as electromagnetic waves are incident at a horizontal interface. In this case the electromagnetic wave arrives to all the points on the interface almost instantaneously, each of those points acts as a source point of seismic waves and this generates a plane seismic wave that propagates upwards.

If the incident angle of the electromagnetic wavefield is 90^{o}, the angle of the reflected and transmitted seismic wavefields is

$$\theta_{\mathrm{s}}^{\mathrm{s}} = \arcsin\left(\frac{c_{\mathrm{s}}}{c_{\mathrm{em}}}\right) \tag{3.37}$$

which is a very small angle, again in the order of 10^{-3}. This means that for almost any angle of incidence of the electromagnetic wavefield there is generation of non-evanescent seismic waves vertically directed to the upper and lower interfaces.

Reflection coefficients for the SH-TE coupling.

In Figure 3.4 we see the reflection coefficients for the SH-TE coupling. The graphs in this figure are from left to right $|\tilde{\mathbf{r}}_{\mathrm{te,sh}}|$ and $|\tilde{\mathbf{r}}_{\mathrm{sh,te}}|$. On the vertical axis we have the modulus of the reflection coefficient that is calculated as a function of the horizontal slowness p_1 times the velocity of the outgoing wave $c^u_{sh,te}$. In the case of an incident seismic wave the region $0 < p_1 c^u < 1$ corresponds to reflection angles from zero to ninety degrees and for $p_1 c^u \geq 1$ the reflected wave becomes evanescent. Since $|c^u_{\mathrm{te}}|$ is much larger than the incident Sh wave velocity $|c^u_{\mathrm{sh}}|$, the region $0 < p_1 c^u_{\mathrm{te}} < 1$ also corresponds to very small incident angles. In the case of an incident electromagnetic wave any angle of incidence will give an almost normal reflected wave. In the right graph of Figure 3.4 we see $|\tilde{\mathbf{r}}_{\mathrm{sh,te}}|$ in a much wider range of p_1, although it looks as if this coefficient is zero for normal incidence it is just an effect of the scale used on this figure, and there is indeed conversion for normally incident horizontal shear waves, as pointed out in the previous chapter.

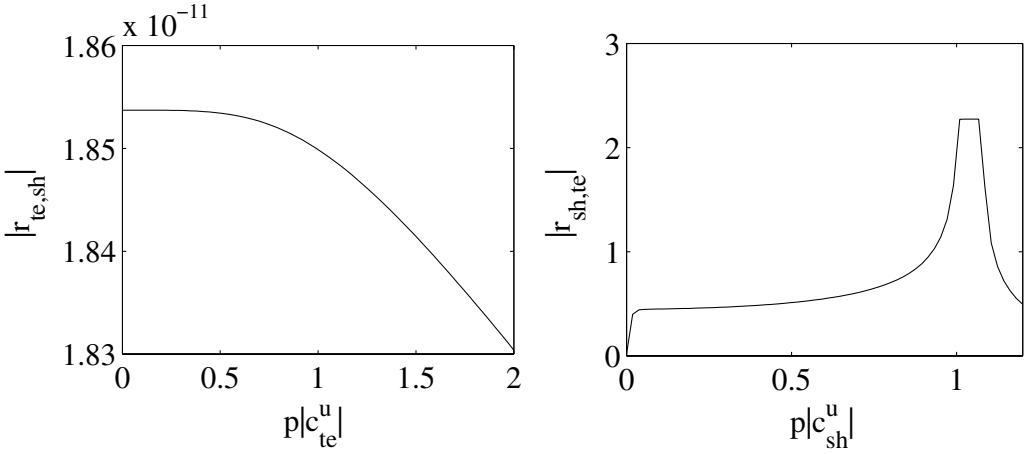

Figure 3.4: *Reflection coefficients of the SH-TE coupling. Left: conversion from horizontal shear wave to TE electromagnetic wave for low values of the ray parameter p_1. Right: conversion from TE electromagnetic wave to horizontal shear wave for high values of the ray parameter p_1.*

Reflection coefficients for the P-SV-TM coupling.

In Figure 3.5 we see the reflection coefficients of the P-SV-TM coupling. The upper row of the four graphs in this figure are conversions from fast-P wave and shear vertical wave to electromagnetic TM wave, i.e. from left to right we have $|\tilde{\mathbf{r}}_{\mathrm{tm,pf}}|$ and $|\tilde{\mathbf{r}}_{\mathrm{tm,sv}}|$. On the lower row of graphs we have conversions from the electromagnetic TM wave to the seismic fast-P and shear vertical waves, i.e. from left to right we have $|\tilde{\mathbf{r}}_{\mathrm{pf,tm}}|$ and $|\tilde{\mathbf{r}}_{\mathrm{sv,tm}}|$.

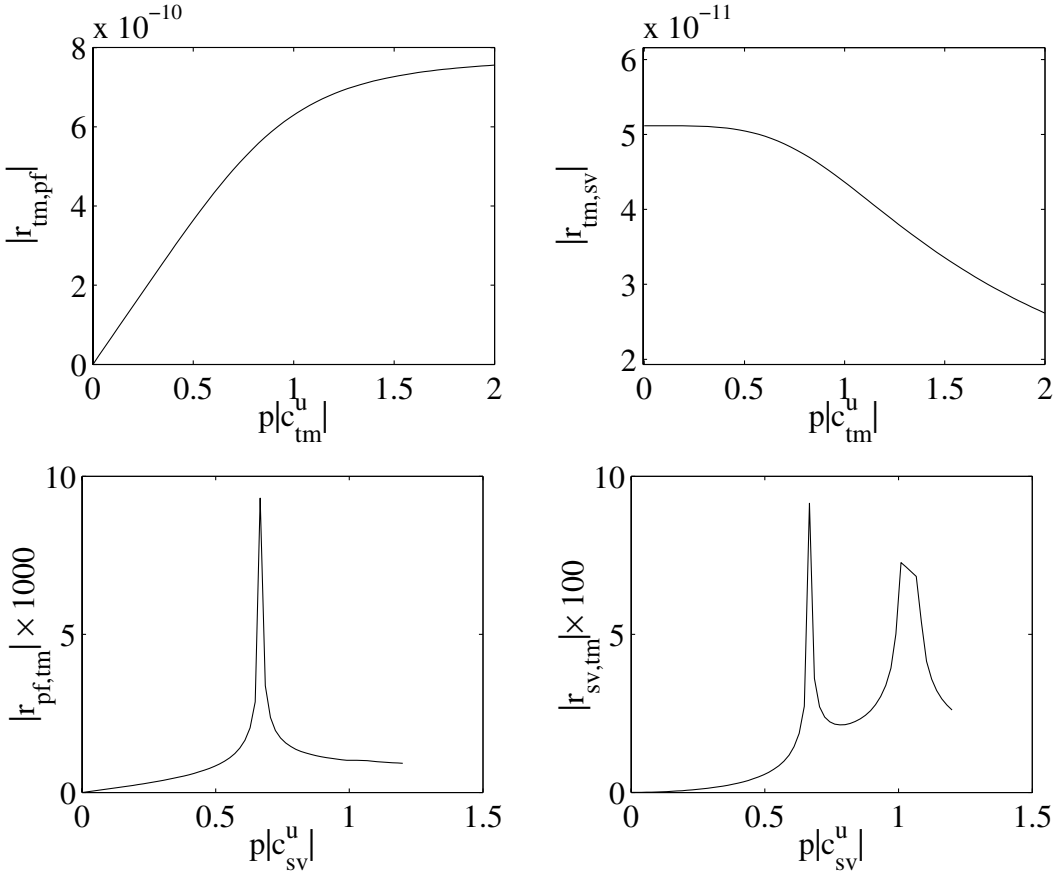

Figure 3.5: *Reflection coefficients for the P-SV-TM coupling. Above: conversions from fast-P (left) and shear vertical waves (right) to electromagnetic TM wave. Below: conversions from electromagnetic TM wave to fast-P (left) and shear vertical waves (right)*

As in the previous results of this section, on the vertical axis we have the

modulus of the reflection coefficient that is calculated as a function of the horizontal slowness p_1 times the velocity of the TM electromagnetic wave $c_{\rm tm}^{\rm u}$ for the seismic-electromagnetic reflections, and the velocity of the vertical shear wave for the electromagnetic-seismic case.

As described by the equations derived in Section 2.7 the reflection coefficients that include the fast-P wave are zero at normal incidence, and according to Figure 3.5 their value increases as p_1 does. In the upper left graph of Figure 3.5 we have the coefficient $|\tilde{\mathbf{r}}_{\rm tm,pf}|$ for the range of p_1 in which this reflection generates an homogeneous wavefield. We clearly see in this graph how the compressional waves also generate homogeneous seismic waves. We can therefore classify the angle of incidence in three different ranges according to the generated wavefields

$$\theta_{\rm s} = \begin{cases} 0^{\rm o} & \text{no conversion from compressional waves and the conversion from shear waves produces homogeneous electromagnetic waves} \\ < \theta_{\rm s}^{\rm c} & \text{the conversion from all seismic waves produces homogeneous electromagnetic waves} \\ > \theta_{\rm s}^{\rm c} & \text{the conversion from all incident seismic waves produces only evanescent electromagnetic wavefields} \end{cases}$$

As we already saw previously, the conversion from electromagnetic to seismic wavefields does not depend so dramatically on the angle of incidence and any angle will generate reflected and transmitted seismic wavefields almost normal to the interface.

Variation of the Reflection coefficients for the SH-TE case with the porosity contrast.

In Figure 3.6 we see the variation of the reflection coefficients for the SH-TE coupling with the porosity contrast. For this and the coming simulations we have chosen to link porosity and permeability as related in the Kozeny-Carman relation $k = \phi^2/A$ where A is a constant of the porous medium, in this case $A = 2.963 \cdot 10^{11}$. On the vertical axis we find the modulus of the reflection coefficient and on the horizontal axis the upper and lower porosities differences. All medium parameters are equal in both media, except the porosity that in the upper medium is 0.3 and in the lower medium ranges from 0.2 to 0.4, therefore when $\Delta\phi = \phi^u - \phi^l = 0$ both porosities are equal and there is no reflection.

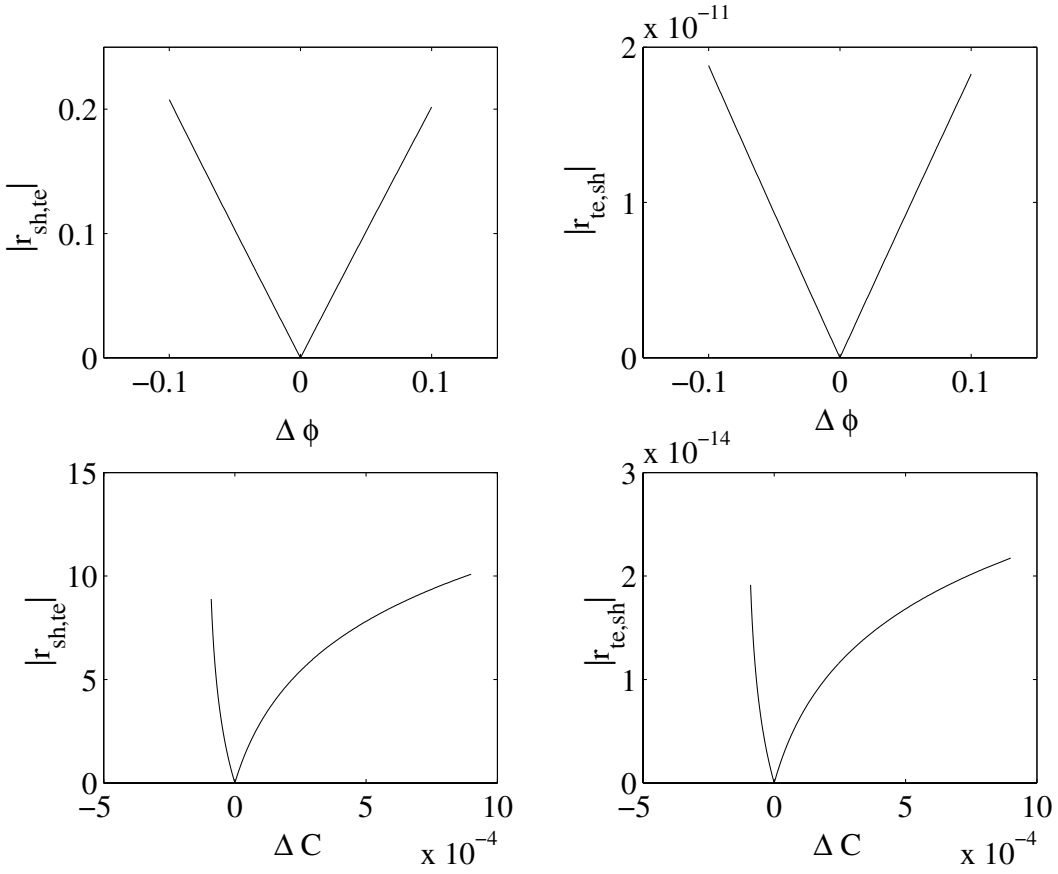

Figure 3.6: *Variation of the Reflection coefficients for the SH-TE coupling with the pore fluid ion concentration contrast.*

Variation of the Reflection coefficients for the SH-TE case with the pore fluid ion concentration contrast.

In Figure 3.6 we see the variation of the reflection coefficients for the SH-TE coupling with the pore fluid ion concentration contrast. On the vertical axis we find the modulus of the reflection coefficient and on the horizontal axis the ion concentration ratio. All medium parameters are equal in both media, except the ion concentration that in the upper medium is 10^{-4}M and in the lower medium ranges from 10^{-5}M to 10^{-3}M, therefore when $\Delta C = C^u - C^l = 0$ both ion concentrations are equal and there is no reflection.

3.3.2 Reflection and transmission coefficients for the porous/ vacuum interface

In this section we derive the reflection and transmission coefficients for the surface of the earth that will be simulated as an interface between an upper vacuum halfspace and a lower porous medium. Later in the chapter we shall show how in the wavefield decomposition at the source and in the wavefield composition at the receiver, the reflection at the surface plays an important role.

In order to obtain these coefficients we use the scattering matrix method presented in the previous section, but on this case assuming that no seismic waves propagate in the vacuum, so applying equations (3.18) and (3.19) to the vacuum/porous interface we can write

$$\tilde{\mathbf{P}}^{\text{out}}_{\text{vac}} = \tilde{\mathbf{S}}_{\text{vac}} \tilde{\mathbf{P}}^{\text{in}}_{\text{vac}}, \tag{3.38}$$

or

$$\begin{pmatrix} \mathbf{P}^{-u}_{\text{vac}} \\ \mathbf{P}^{+l} \end{pmatrix} = \begin{pmatrix} \tilde{\mathbf{r}}^{+}_{\text{vac}} & \tilde{\mathbf{t}}^{-}_{\text{vac}} \\ \tilde{\mathbf{t}}^{+}_{\text{vac}} & \tilde{\mathbf{r}}^{-}_{\text{vac}} \end{pmatrix} \begin{pmatrix} \mathbf{P}^{+u}_{\text{vac}} \\ \mathbf{P}^{-l} \end{pmatrix} \tag{3.39}$$

where $\mathbf{P}^{\pm u}_{\text{vac}}$ contains only the wavefields that can propagate in vacuum, i.e. electromagnetic wavefields, and the coefficients with the subscript $_{\text{vac}}$ take into account that no seismic wave can propagate in vacuum.

We use the same approach as in the porous/porous case, but bearing in mind that only electromagnetic wavefields propagate in the vacuum, then $\mathbf{P}^{\pm u}_{\text{vac}}$ from equation (3.39) is

$$\mathbf{P}^{\pm u}_{\text{vac}} = \begin{pmatrix} \mathbf{0} \\ \mathbf{P}^{\pm u}_{\text{em}} \end{pmatrix}, \tag{3.40}$$

and the coefficients

$$\tilde{\mathbf{r}}^{+}_{\text{vac}} = \begin{pmatrix} 0 & 0 \\ 0 & \tilde{r}^{+}_{\text{em,em}} \end{pmatrix}, \tilde{\mathbf{t}}^{-}_{\text{vac}} = \begin{pmatrix} 0 & 0 \\ \tilde{t}^{-}_{\text{em,se}} & \tilde{t}^{-}_{\text{em,em}} \end{pmatrix}, \tag{3.41}$$

$$\tilde{\mathbf{t}}^{+}_{\text{vac}} = \begin{pmatrix} 0 & \tilde{t}^{+}_{\text{se,em}} \\ 0 & \tilde{t}^{+}_{\text{em,em}} \end{pmatrix}, \tilde{\mathbf{r}}^{-}_{\text{vac}} = \begin{pmatrix} \tilde{r}^{-}_{\text{se,se}} & \tilde{r}^{-}_{\text{se,em}} \\ \tilde{r}^{-}_{\text{em,se}} & \tilde{r}^{-}_{\text{em,em}} \end{pmatrix}, \tag{3.42}$$

where the subscripts $_{\text{se}}$ and $_{\text{em}}$ refer to the seismic and electromagnetic waves from each type of coupling.

In order to solve the equations of the system (3.39) we need a number of boundary conditions equal to the number of wavefields to which the scattering matrix is applied, which is 3 for the SH-TE coupling and 5 for the P-SV-TM

coupling. From the quantities present in vector $\tilde{\mathbf{Q}}_{\mathrm{a}}$, equations (2.109-2.110) we choose $-\tilde{\tau}_{23}$, $-\tilde{H}_1$ and $\tilde{E}_2$ to form the boundary conditions for the SH-TE coupling, and $-\tilde{\tau}_{13}$, $\tilde{H}_2$, $\tilde{E}_1$, $-\tilde{\tau}_{33}$, and $\tilde{p}$ to form the boundary conditions for the P-SV-TM coupling. Since the vacuum cannot sustain stresses, and since horizontal components of the magnetic and electric fields should be continuous across this interface we thus have

$$\tilde{\mathbf{Q}}^{\mathrm{u}}_{\mathrm{vac}} = \tilde{\mathbf{Q}}^{\mathrm{l}}_{\mathrm{vac}} \tag{3.43}$$

or

$$\begin{pmatrix} 0 \\ -\tilde{H}_1 \\ \tilde{E}_2 \end{pmatrix}^{\mathrm{u}}_{\mathrm{H}} = \begin{pmatrix} -\tilde{\tau}_{23} \\ -\tilde{H}_1 \\ \tilde{E}_2 \end{pmatrix}^{\mathrm{l}}_{\mathrm{H}} \quad \text{and} \quad \begin{pmatrix} 0 \\ \tilde{H}_2 \\ \tilde{E}_1 \\ 0 \\ 0 \end{pmatrix}^{\mathrm{u}}_{\mathrm{V}} = \begin{pmatrix} -\tilde{\tau}_{13} \\ \tilde{H}_2 \\ \tilde{E}_1 \\ -\tilde{\tau}_{33} \\ \tilde{p} \end{pmatrix}^{\mathrm{l}}_{\mathrm{V}}. \tag{3.44}$$

We can express the two-way quantities present in the boundary conditions as the composition of the one-way wavefields propagating in the upper or lower media as

$$\tilde{\mathbf{Q}}^{\mathrm{u}}_{\mathrm{vac}} = \tilde{\mathbf{L}}^{\mathrm{u}}_{\mathrm{vac}} \tilde{\mathbf{P}}^{\mathrm{u}}_{\mathrm{vac}} \quad \text{and} \quad \tilde{\mathbf{Q}}^{\mathrm{l}}_{\mathrm{vac}} = \tilde{\mathbf{L}}^{\mathrm{l}}_{\mathrm{vac}} \tilde{\mathbf{P}}^{\mathrm{l}}_{\mathrm{vac}}, \tag{3.45}$$

where the composition matrix $\tilde{\mathbf{L}}^{l}_{\mathrm{H}}$ is

$$\tilde{\mathbf{L}}^{\mathrm{l}}_{\mathrm{H}} = j\omega \left(\tilde{\mathbf{a}}^{+l}_{\mathrm{sh}},\, \tilde{\mathbf{a}}^{+l}_{\mathrm{te}},\, \tilde{\mathbf{a}}^{-l}_{\mathrm{sh}},\, \tilde{\mathbf{a}}^{-l}_{\mathrm{te}} \right), \tag{3.46}$$

in which

$$\tilde{\mathbf{a}}^{\pm}_{\mathrm{n}} = \begin{pmatrix} \mp \tilde{q}_{\mathrm{n}} G \\ \pm \tilde{q}_{\mathrm{n}} \hat{\gamma}_{\mathrm{n}} \\ -\mu \hat{\gamma}_{\mathrm{n}} \end{pmatrix} \text{ where } \quad \mathrm{n} = \{\mathsf{sh},\, \mathsf{te}\}. \tag{3.47}$$

The composition operator used for the lower medium $\tilde{\mathbf{L}}^{l}_{\mathrm{H}}$ is the one defined in equation (3.7) but it contains only the rows corresponding to the quantities chosen in the vector $\tilde{\mathbf{Q}}^{\mathrm{l}}_{\mathrm{H}}$ for the boundary conditions. This way we only compose or decompose the quantities that are present in the boundary conditions.

The composition matrix $\tilde{\mathbf{L}}^{\mathrm{u}}_{\mathrm{H}}$ is

$$\tilde{\mathbf{L}}^{\mathrm{u}}_{\mathrm{H}} = j\omega \left(\tilde{\mathbf{a}}^{+u}_{\mathrm{te}}, \tilde{\mathbf{a}}^{-u}_{\mathrm{te}} \right) = \frac{1}{\sqrt{2}} \begin{pmatrix} 0 & 0 \\ -\tilde{\tilde{Y}} & \tilde{\tilde{Y}} \\ 1 & 1 \end{pmatrix}, \tag{3.48}$$

The composition operator for the upper medium $\tilde{\mathbf{L}}_{\mathrm{H}}^{\mathrm{u}}$ was extracted from [26] where the parameter $\tilde{\tilde{Y}}$ is

$$\tilde{\tilde{Y}} = \frac{\tilde{\Gamma}}{j\omega\mu_0} \quad \text{and} \quad \tilde{\Gamma} = \omega\sqrt{p_1^2 - \frac{1}{c_0}}. \tag{3.49}$$

The composition matrix $\tilde{\mathbf{L}}_{\mathrm{V}}^{\mathrm{u}}$ is

$$\tilde{\mathbf{L}}_{\mathrm{V}}^{\mathrm{u}} = j\omega\left(\tilde{\mathbf{b}}_{\mathrm{tm}}^{+u}, \tilde{\mathbf{b}}_{\mathrm{tm}}^{-u}\right) = \begin{pmatrix} 0 & 0 \\ \tilde{Y} & \tilde{Y} \\ 1 & -1 \\ 0 & 0 \\ 0 & 0 \end{pmatrix}. \tag{3.50}$$

The composition operator for the upper medium $\tilde{\mathbf{L}}_{\mathrm{V}}^{\mathrm{u}}$ was also extracted from [26] where the parameter $\tilde{Y}$ is

$$\tilde{Y} = \frac{j\omega\varepsilon_0}{\Gamma}. \tag{3.51}$$

The composition matrix $\tilde{\mathbf{L}}_{\mathrm{V}}^{l}$ is

$$\tilde{\mathbf{L}}_{\mathrm{V}}^{l} = j\omega\left(\tilde{\mathbf{b}}_{\mathrm{pf}}^{+l}, \tilde{\mathbf{b}}_{\mathrm{ps}}^{+l}, \tilde{\mathbf{b}}_{\mathrm{sv}}^{+l}, \tilde{\mathbf{b}}_{\mathrm{tm}}^{+l}, \tilde{\mathbf{b}}_{\mathrm{pf}}^{-l}, \tilde{\mathbf{b}}_{\mathrm{ps}}^{-l}, \tilde{\mathbf{b}}_{\mathrm{sv}}^{-l}, \tilde{\mathbf{b}}_{\mathrm{tm}}^{-l}\right) \tag{3.52}$$

where

$$\tilde{\mathbf{b}}_{\mathrm{m}}^{\pm} = \begin{pmatrix} \mp 2p_1\tilde{q}_{\mathrm{m}}c_{\mathrm{m}}G \\ 0 \\ -(pc_{\mathrm{m}}\hat{\gamma}_{\mathrm{m}}\hat{\rho}_{\mathrm{E}}\hat{\mathcal{L}})/(\hat{\varepsilon} - \hat{\rho}_{\mathrm{E}}\hat{\mathcal{L}}^2) \\ (2Gp_1^2c_{\mathrm{m}}^2 - H - \hat{\gamma}_{\mathrm{m}}C)/c_{\mathrm{m}} \\ -(C + \hat{\gamma}_{\mathrm{m}}M)/c_{\mathrm{m}} \end{pmatrix}, \quad \tilde{\mathbf{b}}_{n}^{\pm} = \begin{pmatrix} \pm c_n(\tilde{q}_{\mathrm{n}}^2 - p_1^2)G \\ \pm\hat{\gamma}_{\mathrm{n}}/c_{\mathrm{n}} \\ \mu\tilde{q}_{\mathrm{n}}c_{\mathrm{n}}\hat{\gamma}_{\mathrm{n}} \\ -2p_1\tilde{q}_{\mathrm{n}}c_{\mathrm{n}}G \\ 0 \end{pmatrix}. \tag{3.53}$$

The composition operator used in this occasion for the lower medium $\tilde{\mathbf{L}}_{\mathrm{V}}^{l}$ is the one defined in equation (3.13) but it contains only the rows corresponding to the quantities chosen in the vector $\tilde{\mathbf{Q}}_{\mathrm{V}}^{l}$ for the boundary conditions.

From here onward the derivation of the reflection and transmission coefficients for the porous/vacuum interface follows the same scheme as in section 3.3 where the coefficients for the porous/porous case were derived.

Reflection coefficients for the SH-TE coupling at a porous/vacuum interface.

In Figure 3.7 we see the reflection coefficients for the SH-TE coupling for the porous/vacuum case. The graphs in this figure are from left to right $|\tilde{\mathbf{r}}^{-}_{\mathrm{te,sh}}|$ and $|\tilde{\mathbf{r}}^{-}_{\mathrm{sh,te}}|$. On the vertical axis we have the modulus of the reflection coefficient that is calculated as a function of the horizontal slowness p_1 times the velocity of the outgoing wave $c^{u}_{sh,te}$.

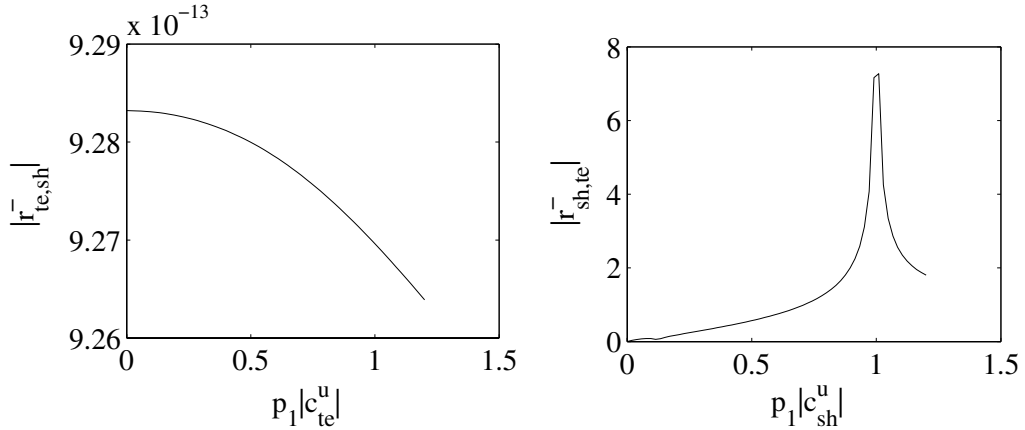

Figure 3.7: *Reflection coefficients of the SH-TE coupling at a vacuum/porous interface. Left: conversion from horizontal shear wave to TE electromagnetic wave for low values of the ray parameter p_1. Right: conversion from TE electromagnetic wave to horizontal shear wave for high values of the ray parameter p_1.*

Reflection coefficients for the P-SV-TM coupling at a vacuum/porous interface.

In Figure 3.8 we see the reflection coefficients of the P-SV-TM coupling for the vacuum/porous case. The upper row of the four graphs in this figure are conversions from fast-P wave and shear vertical wave to electromagnetic TM wave, i.e. from left to right we have $|\tilde{\mathbf{r}}^{-}_{\mathrm{tm,pf}}|$ and $|\tilde{\mathbf{r}}^{-}_{\mathrm{tm,sv}}|$. On the lower row of graphs we have conversions from the electromagnetic TM wave to the seismic fast-P and shear vertical waves, i.e. from left to right we have $|\tilde{\mathbf{r}}^{-}_{\mathrm{pf,tm}}|$ and $|\tilde{\mathbf{r}}^{-}_{\mathrm{sv,tm}}|$.

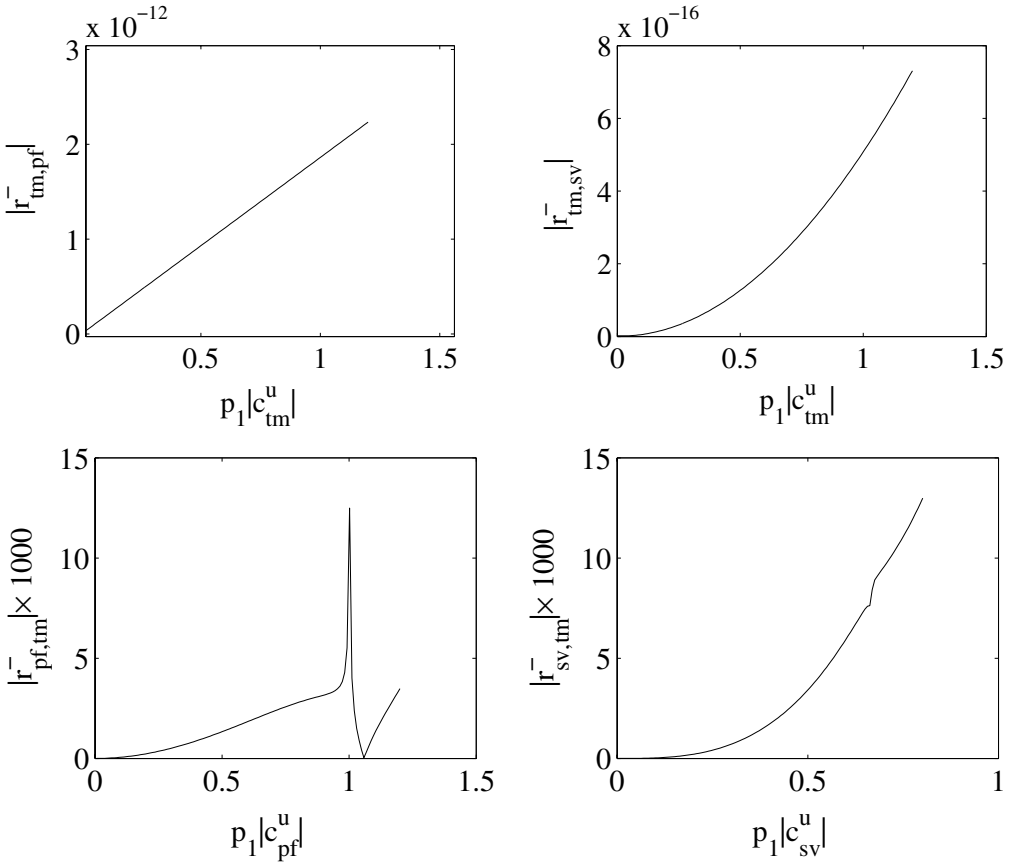

Figure 3.8: *Reflection coefficients for the P-SV-TM coupling at a vacuum/porous interface. Above: conversions from fast-P (left) and shear vertical waves (right) to electromagnetic TM wave. Below: conversions from electromagnetic TM wave to fast-P (left) and shear vertical waves (right)*

3.4 Wavefield extrapolators

Here we present the wavefield extrapolation operators. These operators describe the propagation of a wavefield through a medium, they are

$$\tilde{\mathbf{W}}^{\pm}_{\mathrm{V}} = \begin{pmatrix} \tilde{w}^{\pm}_{\mathrm{pf}} & 0 & 0 & 0 \\ 0 & \tilde{w}^{\pm}_{\mathrm{ps}} & 0 & 0 \\ 0 & 0 & \tilde{w}^{\pm}_{\mathrm{sv}} & 0 \\ 0 & 0 & 0 & \tilde{w}^{\pm}_{\mathrm{tm}} \end{pmatrix} \text{ and } \tilde{\mathbf{W}}^{\pm}_{\mathrm{H}} = \begin{pmatrix} \tilde{w}^{\pm}_{\mathrm{sh}} & 0 \\ 0 & \tilde{w}^{\pm}_{\mathrm{te}} \end{pmatrix} \tag{3.54}$$

where

$$\tilde{w}^{\pm}_{\mathrm{m,n}}(p_1, z_{\mathrm{r}}, z_{\mathrm{o}}, \omega) = e^{-j\omega\tilde{q}_{\mathrm{m,n}}|z_{\mathrm{r}} - z_{\mathrm{o}}|} \tag{3.55}$$

where the general sign convention holds. We use the $+$ sign in $\tilde{w}^{+}_{\mathrm{m,n}}$ when the wavefield is downgoing, i.e. when $z_{\mathrm{r}} > z_0$ and the - sign in $\tilde{w}^{-}_{\mathrm{m,n}}$ when the wavefield is upgoing, i.e. when $z_{\mathrm{r}} < z_0$.

3.5 Source decomposition operator

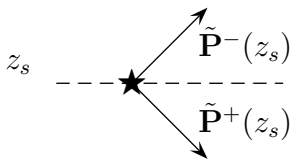

Figure 3.9: *The source decomposition operator converts the two way wavefields into up and downgoing one way wavefields at the source level*

The relation between the two-way wavefields generated by the source and the up or downgoing one-way wavefields is given by the source decomposition operator. In this section we derive a general expression for both cases SH-TE and P-SV-TM.

The one-way representation of the source function $\tilde{\mathbf{S}}(z)$, in the (p_1, ω) domain is

$$\tilde{\mathbf{S}}(z) = \tilde{\mathbf{L}}^{-1}\tilde{\mathbf{D}}(z). \tag{3.56}$$

where $\tilde{\mathbf{L}}^{-1}$ is the inverse of the composition operator $\tilde{\mathbf{L}}$ defined in the first section of this chapter. The inverse of the composition operator decomposes the different two-way source wavefields into one-way up and downgoing source wavefields. $\tilde{\mathbf{D}}(z)$ is a matrix containing the source vectors defined in equations (2.117) and (2.118) that have been chosen as sources. Note that equations (3.57) and (3.58) are not the only possible selection of source vectors and other combinations are also available, e.g. one containing J_3^e for the P-SV-TM coupling. The two-way source matrix $\tilde{\mathbf{D}}_{\mathrm{H}}(z)$ contains therefore two source types while $\tilde{\mathbf{D}}_{\mathrm{V}}(z)$ contains four

$$\tilde{\mathbf{D}}_{\mathrm{H}} = \begin{pmatrix} \tilde{\mathbf{D}}_{\mathrm{H}}^{\mathrm{f_2}} & \tilde{\mathbf{D}}_{\mathrm{H}}^{\mathrm{J_2^e}} \end{pmatrix} \tag{3.57}$$

$$\tilde{\mathbf{D}}_{\mathrm{V}} = \begin{pmatrix} \tilde{\mathbf{D}}_{\mathrm{V}}^{\mathrm{f_1}} & \tilde{\mathbf{D}}_{\mathrm{V}}^{\mathrm{f_3}} & \tilde{\mathbf{D}}_{\mathrm{V}}^{\mathrm{J_1^e}} & \tilde{\mathbf{D}}_{\mathrm{V}}^{\mathrm{J_3^e}} \end{pmatrix}, \tag{3.58}$$

and substituting from equations (2.117) and (2.118) we have

$$\tilde{\mathbf{D}}_{\mathrm{H}}^{\mathrm{f_2}} = \left(\tilde{f}_2^b - \frac{\rho^f}{\rho^E}\tilde{f}_2^f, -\tilde{\mathcal{L}}\tilde{f}_2^f, 0, 0 \right)^t \tag{3.59}$$

$$\tilde{\mathbf{D}}_{\mathrm{H}}^{\mathrm{J_2^e}} = \left(0, -\tilde{J}_2^e, 0, 0 \right)^t \tag{3.60}$$

$$\tilde{\mathbf{D}}_{\mathrm{V}}^{\mathrm{f_1}} = \left(0, \frac{p_1}{\rho^E}\tilde{f}_1^f, \tilde{f}_1^b - \frac{\rho^f}{\rho^E}\tilde{f}_1^f, -\hat{\mathcal{L}}\tilde{f}_1^f, 0, 0, 0, 0 \right)^t \tag{3.61}$$

$$\tilde{\mathbf{D}}_{\mathrm{V}}^{\mathrm{f_3}} = \left(0, 0, 0, 0, \tilde{f}_3^b - \frac{\rho^f}{\rho^E}\tilde{f}_3^f, \tilde{f}_3^f, 0 \right)^t \tag{3.62}$$

$$\tilde{\mathbf{D}}_{\mathrm{V}}^{\mathrm{J_1^e}} = \left(0, 0, 0, -\tilde{J}_1^e, 0, 0, 0, 0 \right)^t \tag{3.63}$$

$$\tilde{\mathbf{D}}_{\mathrm{V}}^{\mathrm{J_2^m}} = \left(0, 0, 0, 0, -\tilde{J}_2^m, 0, 0, 0 \right)^t \tag{3.64}$$

where the superscript in $\tilde{\mathbf{D}}$ shows the type and direction of the source. In the coming two-way wave models we use some of the source types present here, when the source is seismic we assume that the forces applied to the fluid and to the solid are equal, therefore $\tilde{f}_i^f = \tilde{f}_i^b$.

For the following simulations it will be convenient to separate the up and downgoing one-way wavefields from the source, we can therefore write equation

(3.56) as

$$\begin{pmatrix} \tilde{\mathbf{S}}^{+} \\ \tilde{\mathbf{S}}^{-} \end{pmatrix} = \begin{pmatrix} \tilde{\mathbf{N}}_{11} & \tilde{\mathbf{N}}_{12} \\ \tilde{\mathbf{N}}_{21} & \tilde{\mathbf{N}}_{22} \end{pmatrix} \begin{pmatrix} \tilde{\mathbf{D}}_{1} \\ \tilde{\mathbf{D}}_{2} \end{pmatrix} \tag{3.65}$$

Later in this chapter we make use of this operator when simulating the sources used in a seismo-electric reflection simulation. In this case we only use the downgoing components of the source $\tilde{\mathbf{S}}^{+}(z)$ because we simulate a source at the surface. The next chapter deals with more complex cases like wellbore to wellbore where the source is placed inside a wellbore and the up and downgoing source wavefields are used.

3.6 Receiver composition operator

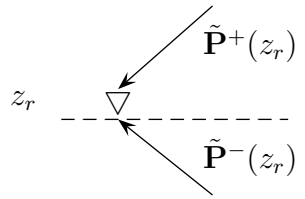

Figure 3.10: *The relation between the two-way wavefield recorded at the receivers and the one-way wavefields is given by the receiver composition operator*

The relation between the two-way wavefield recorded at the receivers and the one-way wavefields arriving there is given by the receiver composition operator, that combines all the up and downgoing one-way wavefields into the measurable two-way wavefields we are interested in. For example the signal we can measure with electrodes placed on the surface in the x_1 direction will be composed of the conversion of compressional and shear waves at some interface, plus the electric fields that these waves will carry along, thus we need the receiver composition operator to compose these two-way wavefields (E_1) from the one-way wavefields that arrive to the receivers (fast-P, vertical shear and electromagnetic TM waves). In this section we derive a general expression for the receiver composition operator. Later this expression will be particularized and used for the cases in the forward simulations.

From chapter 2 we know that the composition of two-way wavefields from one-way wavefields is done by the composition operator $\mathbf{L}(z)$ by means of the transformation

$$\tilde{\mathbf{Q}} = \tilde{\mathbf{L}}\tilde{\mathbf{P}}, \tag{3.66}$$

where $\tilde{\mathbf{Q}}$ contains the two-way wavefields and $\tilde{\mathbf{P}}$ the one-way wavefield that contains the upgoing and downgoing waves.

The derivation of the receiver composition operator in the coming lines requires that the vector $\tilde{\mathbf{Q}}$ has certain order, so the second half of it contains two-way wavefields that we want to measure in the field. This allows us to separate the composition matrix $\tilde{\mathbf{L}}$ into easier to handle submatrices for the coming derivation.

For the SH-TE coupling we do not need to rearrange $\tilde{\mathbf{Q}}_{\mathrm{H}}$ since $\tilde{\mathbf{Q}}_{2,H}$ already contains the measurable two-way quantities we want

$$\tilde{\mathbf{Q}}_{\mathrm{H}} = \begin{pmatrix} \tilde{\mathbf{Q}}^t_{1,\mathrm{H}} & \tilde{\mathbf{Q}}^t_{2,\mathrm{H}} \end{pmatrix}^t = \begin{pmatrix} -\tilde{\tau}^b_{23} & -\tilde{H}_1 & \tilde{E}_2 & \tilde{v}^s_2 \end{pmatrix}^t \tag{3.67}$$

$$\text{where} \quad \tilde{\mathbf{Q}}_{2,\mathrm{H}} = \begin{pmatrix} \tilde{E}_2 & \tilde{v}^s_2 \end{pmatrix}^t \tag{3.68}$$

However for the P-SV-TM coupling this is no longer the case since

$$\tilde{\mathbf{Q}}_{\mathrm{V}} = (\tilde{v}^s_3 \quad \tilde{w}_3 \quad -\tilde{\tau}^b_{13} \quad \tilde{H}_2 \quad \tilde{E}_1 \quad -\tilde{\tau}^b_{33} \quad \tilde{p} \quad \tilde{v}^s_1)^t \tag{3.69}$$

and the $\tilde{\mathbf{Q}}_{\mathrm{V}}$ vector we need is

$$\tilde{\mathbf{Q}}'_{\mathrm{V}}(z) = \begin{pmatrix} \tilde{\mathbf{Q}}'^{,t}_{1,\mathrm{V}}(z) & \tilde{\mathbf{Q}}'^{,t}_{2,\mathrm{V}}(z) \end{pmatrix}^t = \begin{pmatrix} -\tilde{p} & \tilde{w}_3 & \tilde{\tau}^b_{13} & \tilde{\tau}^b_{33} & \tilde{H}_2 & \tilde{E}_1 & \tilde{v}^s_3 & \tilde{v}^s_1 \end{pmatrix}^t \tag{3.70}$$

where $\mathbf{Q}'_{2,\mathrm{V}}(z)$ is

$$\tilde{\mathbf{Q}}'_{2,\mathrm{V}}(z) = \begin{pmatrix} \tilde{H}_2(z) & \tilde{E}_1(z) & \tilde{v}^s_3(z) & \tilde{v}^s_1(z) \end{pmatrix}^t. \tag{3.71}$$

Thus we need to do the following transformation

$$\tilde{\mathbf{Q}}'_{\mathrm{V}}(z) = \mathbf{\Pi}_{\mathrm{V}}\tilde{\mathbf{Q}}_{\mathrm{V}}(z) \text{ and } \tilde{\mathbf{L}}'_{\mathrm{V}}(z) = \mathbf{\Pi}_{\mathrm{V}}\tilde{\mathbf{L}}_{\mathrm{V}}(z) \tag{3.72}$$

where $\mathbf{\Pi}_{\mathrm{V}}$ is

$$\mathbf{\Pi}_{\mathrm{V}} = \begin{pmatrix} 0 & 0 & 0 & 0 & 0 & 0 & -1 & 0 \\ 0 & 1 & 0 & 0 & 0 & 0 & 0 & 0 \\ 0 & 0 & -1 & 0 & 0 & 0 & 0 & 0 \\ 0 & 0 & 0 & 0 & 0 & -1 & 0 & 0 \\ 0 & 0 & 0 & 1 & 0 & 0 & 0 & 0 \\ 0 & 0 & 0 & 0 & 1 & 0 & 0 & 0 \\ 1 & 0 & 0 & 0 & 0 & 0 & 0 & 0 \\ 0 & 0 & 0 & 0 & 0 & 0 & 0 & 1 \end{pmatrix} \tag{3.73}$$

Note that if the order in $\tilde{\mathbf{Q}}'_{\mathrm{V}}$ should be changed to fit another set of measurable quantities, e.g. to simulate hydrophones as receivers, the row order in $\tilde{\mathbf{L}}'_{\mathrm{V}}$ and $\mathbf{\Pi}_{\mathrm{V}}$ should change accordingly so it would include $\tilde{p}$ in $\tilde{\mathbf{Q}}'_{2,\mathrm{V}}(z)$.

Once we have the required arrangement in $\tilde{\mathbf{Q}}_{\mathrm{a}}$ and $\tilde{\mathbf{L}}_{\mathrm{a}}$ we can express the composition operator as

$$\tilde{\mathbf{L}}' = \begin{pmatrix} \tilde{\mathbf{L}}'^{+}_{1} & \tilde{\mathbf{L}}'^{-}_{1} \\ \tilde{\mathbf{L}}'^{+}_{2} & \tilde{\mathbf{L}}'^{-}_{2} \end{pmatrix}, \tag{3.74}$$

where each of the submatrices is a 2x2 matrix for a=H and 4x4 for a=V. Substituting equation (3.74) into (3.66) gives

$$\begin{pmatrix} \tilde{\mathbf{Q}}'_{1} \\ \tilde{\mathbf{Q}}'_{2} \end{pmatrix} = \begin{pmatrix} \tilde{\mathbf{L}}'^{+}_{1} & \tilde{\mathbf{L}}'^{-}_{1} \\ \tilde{\mathbf{L}}'^{+}_{2} & \tilde{\mathbf{L}}'^{-}_{2} \end{pmatrix} \begin{pmatrix} \tilde{\mathbf{P}}^{+} \\ \tilde{\mathbf{P}}^{-} \end{pmatrix} \tag{3.75}$$

where $\tilde{\mathbf{Q}}'_2$ contains the set of quantities from $\tilde{\mathbf{Q}}'$ that we have selected to be measured by the receivers. Let's assume a generic receiver at depth z_n where the up and downgoing wavefields $\tilde{\mathbf{P}}^{-}$ and $\tilde{\mathbf{P}}^{+}$ respectively arrive, then on the one hand we can write

$$\tilde{\mathbf{Q}}'_2(z_r) = \tilde{\mathbf{C}}^{+}_{\mathrm{r}}(z_r)\tilde{\mathbf{P}}^{+}(z_r) + \tilde{\mathbf{C}}^{-}_{\mathrm{r}}(z_r)\tilde{\mathbf{P}}^{-}(z_r), \tag{3.76}$$

And on the other hand from the lower row of equation (3.74) we can write

$$\tilde{\mathbf{Q}}'_2(z_r) = \tilde{\mathbf{L}}'^{+}_{2}\tilde{\mathbf{P}}^{+}(z_r) + \tilde{\mathbf{L}}'^{-}_{2}\tilde{\mathbf{P}}^{-}(z_r), \tag{3.77}$$

comparing this with equation (3.76) yields the receiver composition operators

$$\tilde{\mathbf{C}}^{-}_{\mathrm{r}} = \tilde{\mathbf{L}}'^{-}_{2} \text{ and } \tilde{\mathbf{C}}^{+}_{\mathrm{r}} = \tilde{\mathbf{L}}'^{+}_{2} \tag{3.78}$$

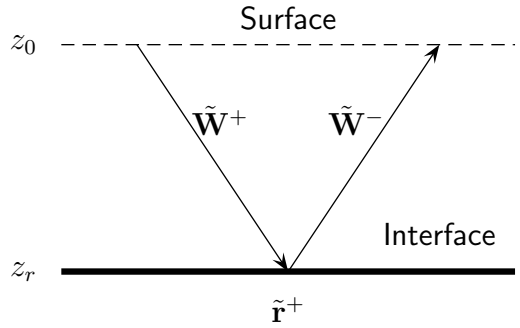

Figure 3.11: *One-way reflection model*

3.7 Results: Reflection model in the (x_1, t) domain

In this section we present some of the results obtained using this approach to the electro-kinetic effect and its use in a geophysical survey. We show first the results of a one-way wavefield case in which we use neither decomposition, nor composition, just up and downgoing wavefields and the reflection at the porous/porous interface. Later we show the effects of the composition and decomposition in a more complex case. This forward simulation has been calculated in the (k_1, ω), and then Fourier transformed to the (x_1, t) domain where the results are shown.

For our simulation we use as a time source function the Ricker wavelet, that in the frequency domain is

$$\hat{S}(\omega) = \frac{2}{\sqrt{\pi}} \frac{f^2}{f_0^3} \exp\left(\frac{-f^2}{f_0^2}\right), \tag{3.79}$$

where f_0 is the peak frequency and has been set to 800 Hz. We can see in Figure 3.11 the setup for our simulation. We consider an interface at a depth of 50m with the same contrast as the one defined in Table 3.1. There are 32 receivers at each side of the source (split-spread configuration), with 1m separation between receivers.

3.7.1 One-way Reflection model in the (x_1, t) domain

In this section we present results of a simple reflection simulation as in Figure 3.11. We compute the propagation of waves down to an interface, the reflection

and its propagation up to the surface. Note that in this subsection's figures there are only one-way wavefields represented. This is a very simple approach to a seismo-electric reflection, but it helps understanding the interaction of the different wavefields, and it will be a reference for the two-way reflection model results that follow the current subsection. The expression that describes this one-way seismo-electric simulation is

$$\tilde{\mathbf{P}}(z_0, z_r) = \tilde{\mathbf{W}}^{-}(z_0, z_r)\tilde{\mathbf{r}}^{+}(z_r)\tilde{\mathbf{W}}^{+}(z_r, z_0) \tag{3.80}$$

where $\tilde{\mathbf{W}}^{\pm}$ is a matrix containing the wavefield extrapolators defined in section 3.4 that propagate the wave from the surface to the interface level z_r and back to the surface, and $\tilde{\mathbf{r}}$ is a matrix containing the reflection coefficients defined in section 3.3 that describe the reflection and conversion between different wavefields. To follow the ray path in this expression, it must be read from right to left, so the first wavefield extrapolator $\tilde{\mathbf{W}}^{+}(z_r, z_0)$ describes the propagation of the wave from the surface to the interface, the reflection coefficient $\tilde{\mathbf{r}}(z_r)$ describes the reflection and conversion of wavefields, and finally the leftmost term in the right hand side of the equation, the wavefield extrapolator $\tilde{\mathbf{W}}^{-}(z_0, z_r)$ describes the propagation of the converted wave from the interface to the surface.

In order to understand the results of this section we have to keep in mind Figures 3.2 and 3.3. In the coming figures we show the result of our model for both types of conversion.

In Figure 3.12 we see the results of the one-way reflection model applied to the seismo-electric conversion of wavefields for the SH-TE coupling. In the left graph we see the conversion of a horizontal shear wave to an electromagnetic TE wave, and in the right one the conversion of an electromagnetic TE wave to a horizontal shear wave. Note that both arrivals occur at the same time, which is one-way vertical seismic travel time. In the left figure we have a conversion taking place right below the source point and from there the electromagnetic wave is radiated to all the receivers in the surface. In the right figure we have a conversion of an electromagnetic wave that arrives to all the points in the interface, from there a seismic plane wave is radiated up to the receivers above them. If there was a dip in the interface, it should be very visible in the conversion from electromagnetic to seismic (right graph in Figure 3.12) because the response would show as a dipped flat arrival. However in the conversion from seismic to electromagnetic as soon as the interface was slightly dipped the incidence would not be normal and the flat arrival from the seismo-electric conversion would dissappear.

In Figure 3.13 we see the results of the same one-way reflection model applied to the seismo-electric conversion of the P-SV-TM coupling wavefields. In the

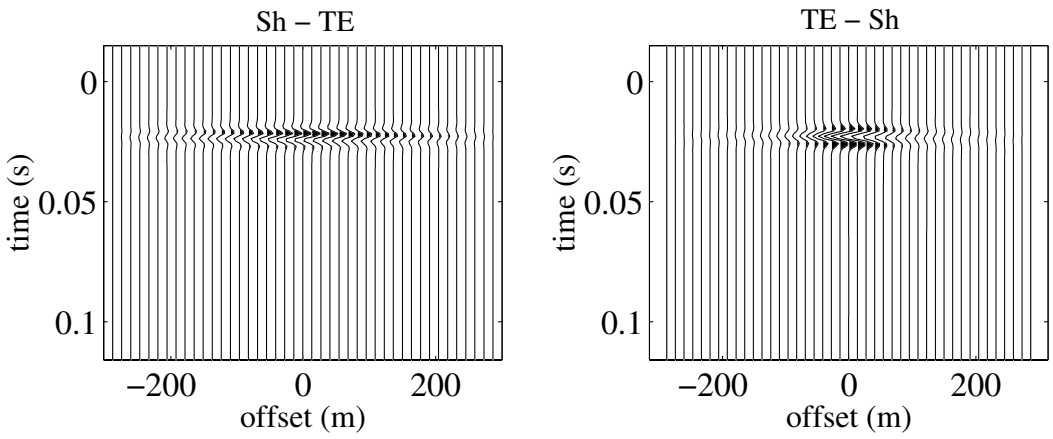

Figure 3.12: *Seismo-electric conversion of wavefields for the SH-TE coupling: in the left graph we see the conversion from shear horizontal wave to TE electromagnetic wave, in the right graph we see the conversion from TE electromagnetic wave to shear horizontal wave.*

upper left graph we see the conversion of a fast P-wave to an electromagnetic TM wave, and in the upper right one the conversion of an electromagnetic TM wave to a fast P-wave. It is clear from these two graphs that at normal incidence there is no conversion between the compressional and the electromagnetic wavefields. Note also how the polarity at both sides of the source is opposite. In the lower graphs we show the same cases in logarithmic scale. Note that in this case we can also see a hyperbolic event with the same arrival time as the seimo-electric flat arrival otherwise invisible due to the difference in amplitude.

In Figure 3.14 we see now the conversion of a vertical shear wave to an electromagnetic TM wave, and in the right one the conversion of an electromagnetic TM wave to a vertical shear wave. Note that both arrivals occur at half-way shear wave travel time. Note also that as predicted in the last section of previous chapter at normal incidence there is conversion between the shear and the electromagnetic waves.

There is a notable feature in all the figures presented on this section, although barely visible in most of them except the conversion from TM to fast-P wave. All of them contain together with the flat seismo-electric event a hyperbolic event with the same arrival time, one way travel time. This occurs in both types of conversions, from seismic to electromagnetic and vice versa. As a incident seismic wave hits normally the interface there is a conversion and an

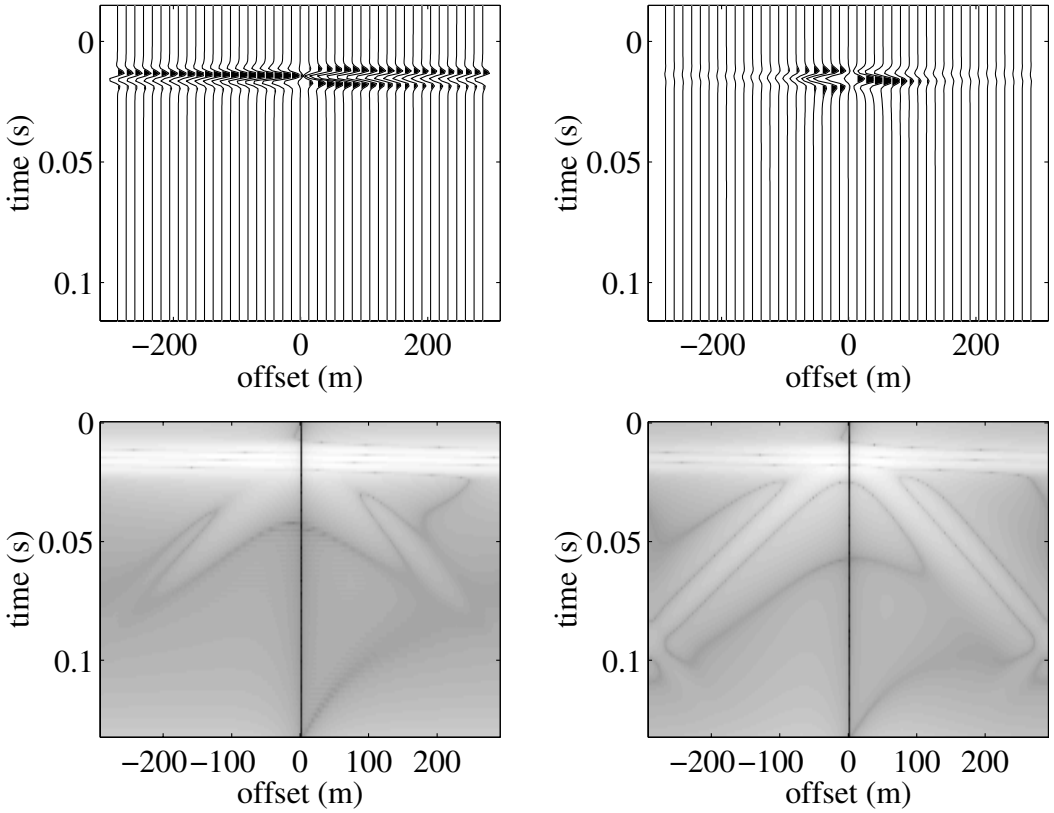

Figure 3.13: *Seismo-electric conversion of wavefields for the P-SV-TM coupling: in the left we see the conversion from fast-P wave to TM electromagnetic wave, in the right vice versa. The lower graphs show the same cases in logarithmic scale.*

electromagnetic wave is generated at the interface. As the wave continues propagating downwards the reflected electromagnetic wave becomes evanescent but due to the high diffusive character of the seismo-electric there is indeed certain amount of energy radiated from this post-critical conversion that can reach the surface if the interface is sufficiently shallow. This conversion takes place in the intersection between the seismic wavefront and the interface, and it moves along the interface with the velocity of the seismic wave. When the incident wave is an electromagnetic wave first there is a conversion and a plane seismic wave is generated at all the points of the interface where the electromagnetic TM wave arrives. However the amplitude of the TM wave is not constant with offset and

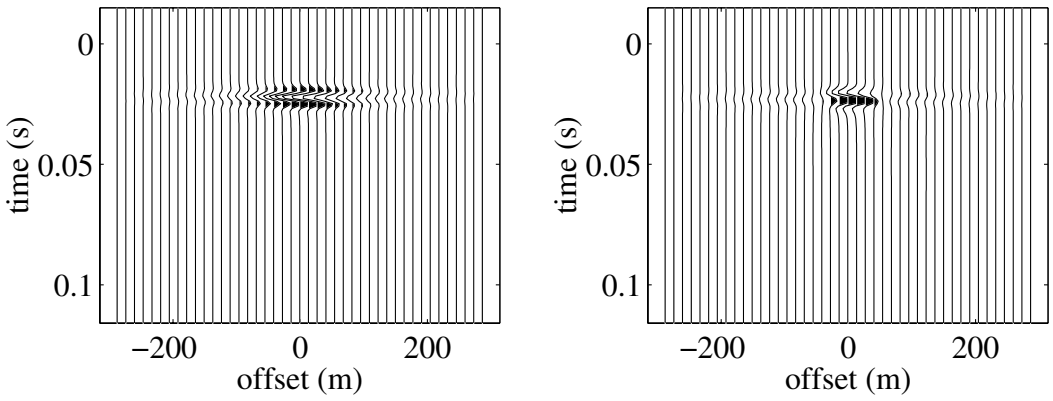

Figure 3.14: *Seismo-electric conversion of wavefields for the P-SV-TM coupling: in the left graph we see the conversion from vertical shear wave to TM electromagnetic wave, in the right graph we see the conversion from TM electromagnetic wave to vertical shear wave.*

this creates an imbalance at the interface surface and contiguous point sources will not cancel completely creating a seismic wave. This would show as an hyperbolic event in the receivers, in the hypothetical case of having very sensitive receivers in an almost completely noise-free environment.

3.7.2 Two-way Reflection model in the (x_1, t) domain

In this section we present results of a seismo-electric reflection that includes the properties of the source and the receivers. This scheme includes the decomposition of the two-way wavefields into one-way wavefields at the source as well as the composition back to two-way wavefields at the receivers. We use the same medium as in the previous section.

In sections 3.5 and 3.6 we derived a general expression for the composition and decomposition operators that has to be specified for this case. Because we place our source and receivers at the surface, the wavefields coming out of the source are only downgoing seismic waves and up and downgoing electromagnetic waves. In any case we use as source wavefields those that are downgoing. The source decomposition operator we use is defined in equation (3.56)

$$\tilde{\mathbf{S}}(z) = \tilde{\mathbf{L}}^{-1}\tilde{\mathbf{D}}(z). \tag{3.81}$$

and the downgoing one-way wavefields are

$$\tilde{\mathbf{S}}^{+} = \tilde{\mathbf{N}}_{11}^{+}\tilde{\mathbf{D}}_{1} \tag{3.82}$$

All the wavefields from the source will be downgoing thus we only use $\tilde{\mathbf{S}}^{+}$.

The two-way source wavefields $\tilde{\mathbf{D}}_1(z)$ are given in equations (2.117-2.118). These expressions for the two-way source terms are expressed as a function of the external force applied to bulk and fluid, $f_i^b = f_i^f$ and of the electric and magnetic source functions, J_i^e and J_i^m. By turning on and off these terms we can select the sources we want to use for the model.

In our model we have assumed that the receivers are also at the surface, therefore there is no ghost wave reflected from the surface and all the wavefields arriving at the receiver are upgoing. Note here that this is a ficticious surface since we do not take surface waves into account. The receiver composition operator we use is defined in equation (3.76)

$$\tilde{\mathbf{Q}}_2'(z_r) = \tilde{\mathbf{C}}_{\mathrm{r}}(z_r)\tilde{\mathbf{P}}^{-}(z_r), \tag{3.83}$$

where

$$\tilde{\mathbf{C}}_{\mathrm{r}}^{-} = \tilde{\mathbf{L}}_2^{-}. \tag{3.84}$$

The expression for the complete simulation including source and receivers is

$$\tilde{\mathbf{Q}} = \tilde{\mathbf{C}}_{\mathrm{r}}^{-}\tilde{\mathbf{W}}^{-}\tilde{\mathbf{r}}^{+}\tilde{\mathbf{W}}^{+}\tilde{\mathbf{S}}^{+}, \tag{3.85}$$

where $\tilde{\mathbf{S}}^{+}$ is defined in equation (3.82) as the downgoing one-way wavefields from the source, $\tilde{\mathbf{W}}^{+}$ and $\tilde{\mathbf{W}}^{-}$ are the extrapolation operators that propagate the wavefield from the source level to the interface and back to the receivers, $\tilde{\mathbf{r}}$ contains the reflection coefficients and $\tilde{\mathbf{C}}_{\mathrm{r}}^{-}$ is the receiver composition operator that composes the two-way wavefields from the upgoing one-way wavefields arriving at the receivers. If this expression is read from right to left we can follow the path of the wavefields. This reflection model does not take into account surface waves.

In Figure 3.16 we see two graphs, on the left we have the measurement with electrodes in the x_2 direction (E_2) and the source is $f_2^b = f_2^f$ in the x_2 direction. In the right graph the measurement with geophones in the x_2 direction (v_2) and the source is a source current $\tilde{J}_2^e$. In both graphs we see two arrivals, one at zero time and a second at 0.025 s. In the left graph the first arrival is the seismo-electric conversion at the source, that arrives at zero time. At one way travel time we find the conversion from Sh to TE waves at the interface. The

amplitude of these arrivals do not let us see a third arrival that arrives after these conversions at two way travel time, it is the electric field that travels with the Sh wave velocity. In the right graph the first arrival is the mechanical disturbance associated with a TE wave. At one way travel time we find the conversion from TE to Sh waves at the interface. Finally there is also a third arrival not seen because of the low amplitude which is the seismo-electric conversion at the source that arrives at two way travel time and has the shape of a hyperbola.

Next we show the results of the two-way wavefields model of the P-SV-TM coupling. The TM-TM reflections have been filtered out. All figures are organized in the same manner, we show the measurements of the receivers H_2 and E_1 if the source is seismic and the measurements of the receivers v_3 and v_1 if the source is electromagnetic.

In Figure 3.17 we have two graphs of the seismo-electric conversion of wavefields for the P-SV-TM coupling. Left to right we see the measurements from the H_2 and E_1 receivers. The source is an external force applied to the bulk and fluid phases in the x_1 direction, $f_1^b = f_1^f$. In this case the seismo-electric conversion at the source radiated as a TM wave has been filtered out. In the left graph we see several events. The first visible arrival is the seismo-electric conversion from a Sv to TM a TM at the interface, that arrives at the one-way seismic travel time for the shear wave. Below this one we see other weaker arrivals with a clear hyperbolic shape resulting from being seismic-seismic reflections that carry an electric field inside. These arrivals are a fast-P-fast-P reflection followed shortly by a Pf-Sv reflection. In the right graph we see three events, a seismo-electric conversion from a Sv to TM a TM at the interface, and the electric fields inside the three different seismic reflections, i.e. fast-P-fast-P, fast-P-Sv and Sv-Sv reflections. In this case the seismo-electric conversion at the interface is much

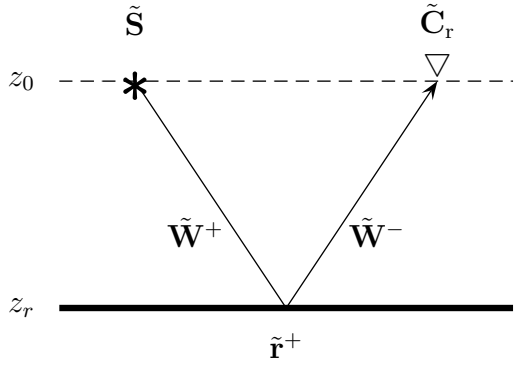

Figure 3.15: *Two-way reflection model*

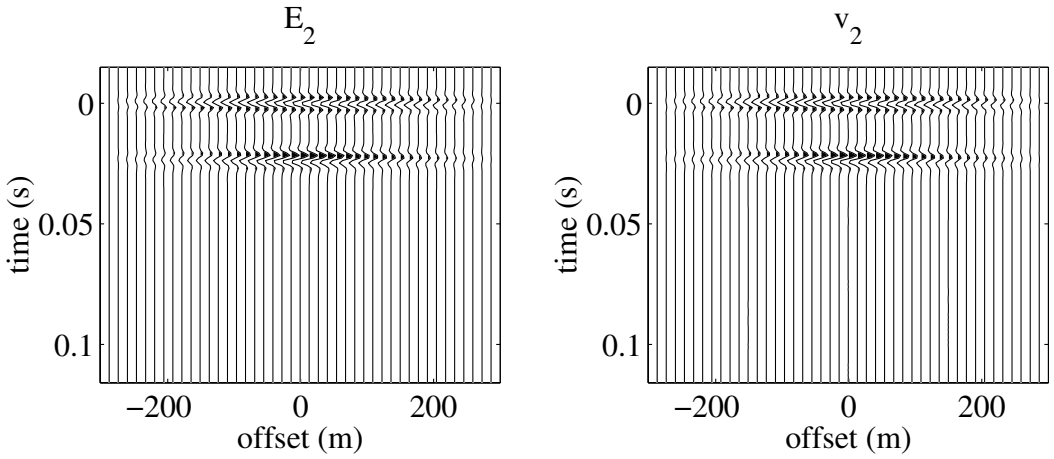

Figure 3.16: *Seismo-electric conversion of wavefields on the SH-TE coupling. Here we see the measurements of the E_2 receiver on the left and the v_2 receiver in the right graph. The sources are an external force applied to the bulk and fluid f_2^b and f_2^f on the left graph and $\tilde{J}_2^e$ on the right graph.*

weaker and barely shows.

If we look at the composition matrix in equation (3.13), the fifth row in $\tilde{\mathbf{b}}_{\mathrm{m}}^{\pm}$ and $\tilde{\mathbf{b}}_{\mathrm{n}}^{\pm}$ gives the E_1 component of the electric field contained in an up or downgoing fast-P wave and vertical shear wave respectively. And the first and last rows of $\tilde{\mathbf{b}}_{\mathrm{n}}^{\pm}$ give the contribution of the TM wave to the velocity fields $\tilde{v}_3$ and $\tilde{v}_1$ respectively. This explains the presence of those EM fields traveling with the seismic waves and the mechanical fields traveling with the EM waves. In fact, by looking at the composition matrix we see that almost all one-way wavefields have a contribution into all of the two-way wavefields, with two exceptions: the longitudinal waves do not carry a magnetic field along, and the transversal waves do not generate changes in the fluid pressure as they pass through a saturated porous medium. This makes sense since in the former case the electric field contained inside a longitudinal wave goes only in the direction of the compression and rarefaction of the medium, which is the direction of propagation. This is the reason why we cannot measure the conversion from fast-P waves with the H_2 receiver. In the latter case because fluids cannot hold shear stresses, there cannot be a contribution from a transversal wave to a pressure field inside a fluid.

In Figure 3.18 we see two graphs of seismo-electric conversion of wavefields for the P-SV-TM coupling, from left to right we see the measurements from H_2

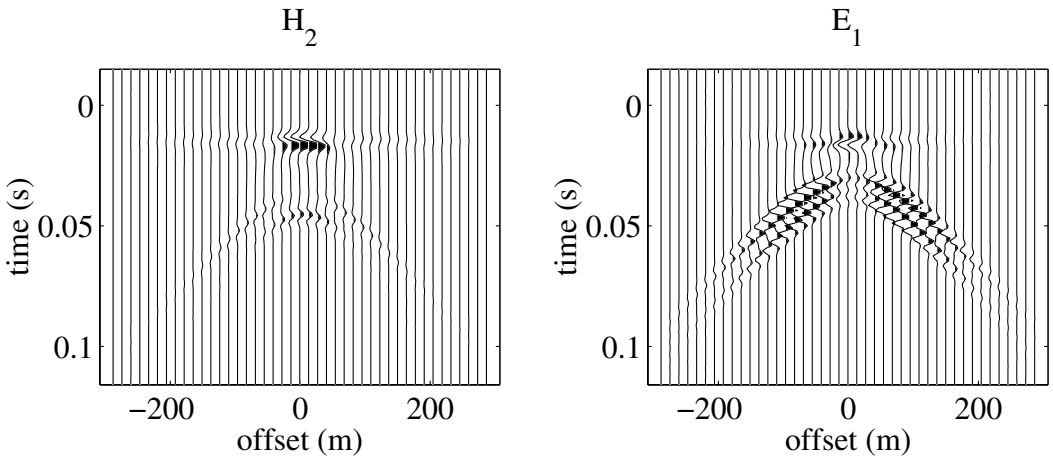

Figure 3.17: *Seismo-electric conversion of wavefields for the P-SV-TM coupling, left to right we see the measurements from the H_2 and E_1 receivers. The source is f_1^b and f_1^f in the x_1 direction.*

and E_1. The source is an external force applied to the bulk and fluid phases in the x_3 direction, $f_3^b = f_3^f$. In the left graph we see several events. The first visible arrival is the seismo-electric conversion at the source, next we find the conversion from a vertical shear to TM wave at the interface that arrives at the one way travel seismic time for the compressional wave. Note that in both of these arrivals the amplitude is zero for normal incidence. In the right graph we see again a seismo-electric conversion at the source and the conversion from a fast-P to TM at the interface. Below this one we see another arrival with a clear hyperbolic shape resulting from being a Pf-Pf reflection that carries an electric field inside, followed by a fast-P-Sv reflection.

In Figure 3.19 we use the current $\tilde{J}_1^e$ in the x_1 direction as a source and the receivers measure v_3 and v_1 respectively. In the left graph we see first the mechanical disturbance associated with the TM wave at time zero followed by the seismo-electric conversion from the TM to fast-P waves at one way travel time. Finally we find the two hyperbolas at two way travel time coming from the seismo-electric conversion at the source where a TM wave converted into a fast-P and vertical shear waves. In the right graph we find a similar case, the mechanical disturbance associated with the TM wave at time zero followed by a very weak seismo-electric conversion at the interface from the TM to vertical shear waves and at two way travel time we finally have two hyperbolas coming

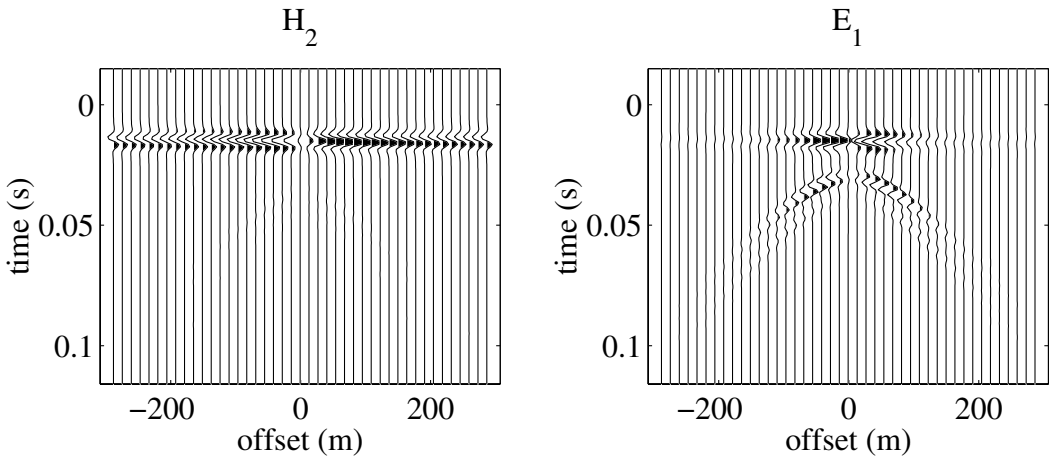

Figure 3.18: *Seismo-electric conversion of wavefields for the P-SV-TM coupling, left to right we see the measurements from the H_2 and E_1 receivers. The source is f_3^b and f_3^f in the x_3 direction.*

from the conversion at the source to fast-P and vertical shear waves. In Figure 3.20 we use v_3 and v_1 geophones, and the source is $\tilde{J}_2^m$. In the left graph we see first the mechanical field associated with the TM wave and the conversion from TM to fast-P wave at the interface at one way fast-P travel time. Note that since there is no conversion between TM and compressional waves at normal incidence when using a J_2^m source the amplitude of the v_3 geophone measurements of the seismo-electric conversions at normal incidence is zero. In the right graph we only find the mechanical field associated to the TM wave that travels down and up almost instantaneously.

Reciprocity theorem applied to the two-way Reflection model in the (x_1, t) domain

The two-way seismo-electric reflection from a horizontal interface follows the reciprocity theorem of the convolution type described in [19] and [28]. Here we are going to check the two-way reflection model for reciprocity. The theorem applied to the two-way reflection of the SH-TE coupling says that

$$E_{2,B}(\mathbf{x}_A,\omega)/s_B(\omega) = \left[\phi v^f_{2,A}(\mathbf{x}_B,\omega) + (1-\phi)v^s_{2,A}(\mathbf{x}_B,\omega)\right]/s_A(\omega), \quad (3.86)$$

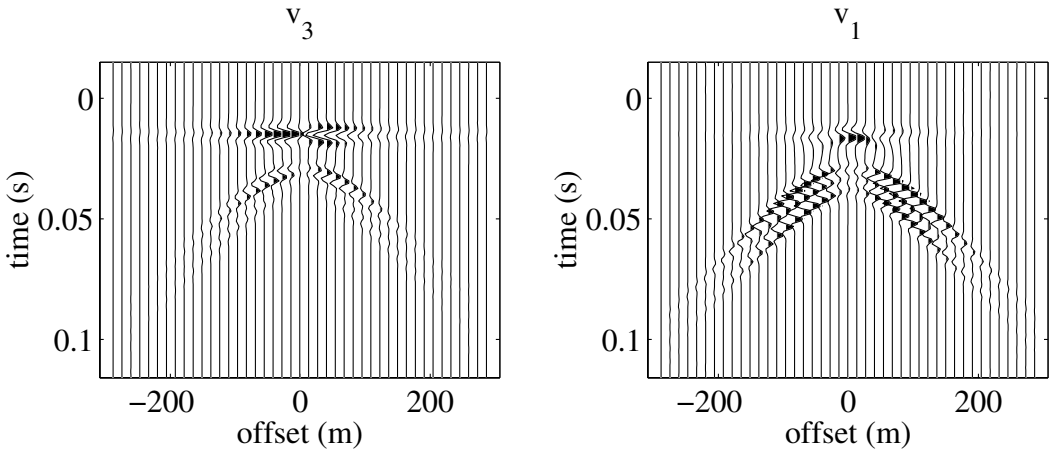

Figure 3.19: *Seismo-electric conversion of wavefields for the P-SV-TM coupling, left to right we see the measurements from the v_3 and v_1 receivers. The source is $\tilde{J}_1^e$ in the x_1 direction.*

where the left side of the equation is the electric field in the x_2 direction at $\mathbf{x}_A$ generated by a force in the x_2 direction at $\mathbf{x}_B$ divided by the source wavelet. The right side of the equation is the velocity in the x_2 direction at $\mathbf{x}_B$ generated by an electric current in the x_2 direction at $\mathbf{x}_A$ divided by the source wavelet of the current. Note that in the right side of the equation we have the fluid and solid particle velocities weighted by the porosity, this is the macroscopic velocity which is measured by the v_2 receiver. However in our theoretical model we are actually measuring v_2^s, so in order to check reciprocity theorem in our model we momentarily set to zero the seismic sources on the fluid $f_2^f = 0$ to eliminate the need for a v_2^f receiver. Then we have that for our model without mechanical force applied on the fluid the reciprocity theorem says

$$E_{2,B}(\mathbf{x}_A, \omega)/s_B(\omega) = (1-\phi)v_{2,A}^s(\mathbf{x}_B, \omega)/s_A(\omega), \tag{3.87}$$

and if we look at Figure 3.16 we see that the measurements from the E_2 and the v_2^s receivers give the same result. Note that we are comparing the graphs of Figure 3.16 where the source used was $f_2^b = f_2^f$, however both cases give a very similar result begin the only difference in the amplitude of the arrivals. If we apply the reciprocity theorem to the P-SV-TM coupling we have for example that

$$E_{1,B}(\mathbf{x}_A, \omega)/s_B(\omega) = \left[\phi v_{3,A}^f(\mathbf{x}_B, \omega) + (1-\phi)v_{3,A}^s(\mathbf{x}_B, \omega)\right]/s_A(\omega), \tag{3.88}$$

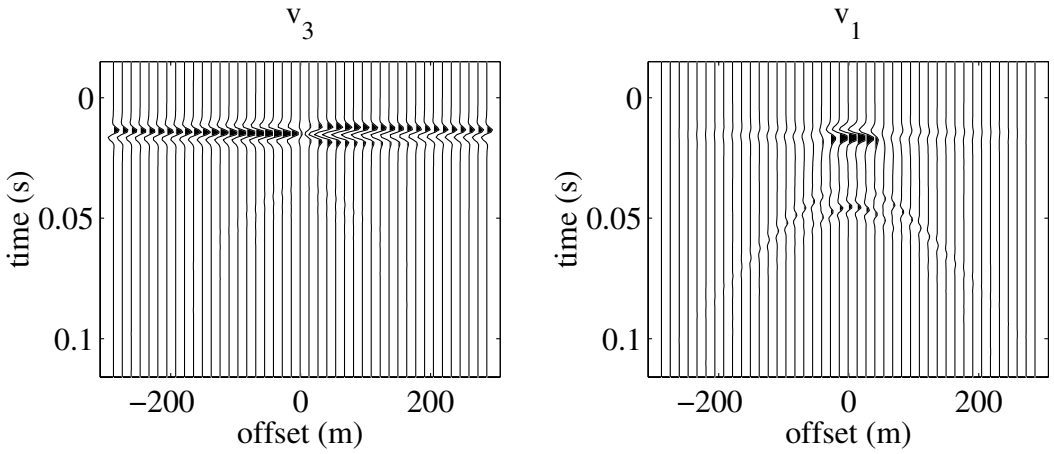

Figure 3.20: *Seismo-electric conversion of wavefields for the P-SV-TM coupling, left to right we see the measurements from the v_3 and v_1 receivers. The source is $\tilde{J}_2^m$ in the x_2 direction.*

and canceling the f_3^f source as in previous case leads to

$$E_{1,B}(\mathbf{x}_A, \omega)/s_B(\omega) = (1-\phi)v^s_{3,A}(\mathbf{x}_B, \omega)/s_A(\omega). \tag{3.89}$$

Comparing the E_1 receiver graph from Figure 3.18 with the v_3 receiver from Figure 3.19 we see the combinations of sources and receivers that equation (3.90) refers to, and how they follow the reciprocity theorem. Note that here in Figure 3.18 the source was $f_3^b = f_3^f$ instead of $f_3^f = 0$, but again there is little difference between both sources and Figure 3.18 serves well for comparison purposes.

The reciprocity theorem can also be applied to other combinations of sources and receivers as

$$H_{2,B}(\mathbf{x}_A, \omega)/s_B(\omega) = (1-\phi)v^s_{1,A}(\mathbf{x}_B, \omega)/s_A(\omega). \tag{3.90}$$

In this case we have to look at the H_2 receiver in Figure 3.18 and at the v_1 receiver of Figure 3.20 and see that again they give the same result.

3.8 Fieldwork

During this project we have done measurements at the fieldwork. However we faced several problems that kept us from measuring a clear seismo-electric arrival.

As mentioned in the published literature about seismo-electric fieldwork, only one of the two types of seismic to electromagnetic conversions is measurable with a good s/n ratio, we are refering to the electric field trapped inside a seismic wave. The other type of seismo-electric conversion, i.e. the EM pulse when a seismic wavefront hits an interface, is more difficult to detect. The reasons are two: first the coupling is very weak and typical signals range in the order of a few millivolts and second the steel electrodes used for picking up these signals do also pick up many other electromagnetic noise present in the field, and most of these are stronger than the sought after pulse. A good example of this is the 50 Hz radiation and its harmonics from the electric grid. It is not uncommon then to find in the measurements strong periodic peaks that complicate the processing.

The first of our serie of fieldwork tests took place at a landfill in the neighborhood of Boxtel, The Netherlands. There we used two parallel lines of electrodes and geophones arranged as in figure 3.21. The receivers are electrodes composed of two vertical steel rods spaced 1m, and a geophone placed in between the rods of each electrode. These sets have 2m separation between the center point of each other, and there are 32 in total. The source was placed at the center and at the ends of the line. The electrodes were oriented in the direction of the profile, thus they measured the E_1 component of the electric field. The source is a seismic shotgun buried .5m and pointed downwards.

We can see in Figure 3.22 a comparison between the electrode and geophone measurements taken. The source is at the left end of the line, 2m from the first geophone. The graph at the left shows the electrodes measurements and the one at the right the geophone measurements. The first thing we see is the remarkable similarity between the geophone and electrode measurements. This is due to the electric field traveling with the compressional wave generated at the explosive source. The geophones measure the vertical velocity of the ground while the electrodes measure the E_1, and this is why these two measurements differ, because the electric field inside the wave prolongs itself a bit further ahead of the wavefront, and therefore it is detected before by the electrodes than the actual seismic wavefront by the geophones.

There is an extra feature in most of the electrode recordings that is not present in the geophone measurements, it is the zero move out event arriving at the very beginning of the left graph, with changing polarity along the offset. Although this arrival looks like a potential seismo-electric conversion, there is a good reason for it not to be. Real seismo-electric conversions when measured with E_1 electrodes have opposite polarity on each side of the source, and remains constant at each side with increasing offset. So if this is not a seismo-electric

conversion, what is it? A. Kepic and K. Butler [11]-[3] have also described this effect on their field measurements, and they explain it as cross-talk from the trigger cable picked up by the electrodes. This explains the consistent occurring of this event at the first samples.

In the Figure 3.23 we see a comparison between the geophone and electrode measurements of traces 5, 8 and 12 from the previous shot. We see here that there is a trend followed by the recordings of both receivers, however the first oscilations of the geophones are not detected by the electrodes due to, possibly, their low electrical content.

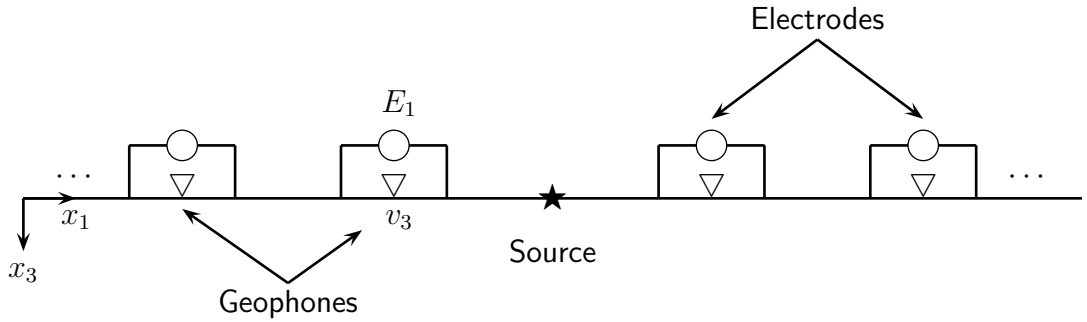

Figure 3.21: Fieldwork setup: The geophones measure v_3 and the electrodes measure E_1. The separation between the centres of pairs of electrodes is 2m.

In figure 3.24 we see another set of measurements of the E_1 electrodes recorded at the same location. In line AA' we have another example of cross-talk between the receivers and the source cable. Events BB' and CC' are the seismic waves that carry an electric field inside. Finally events DD' and EE' are another case of cross-talk, and although tempting cannot be taken for seismo-electric conversions. The reasons are two, in the first place, as well as with event AA' the polarity should be oposite at both sides of the source, and remain constant along the offset, and this is not the case. Second, the frequency content of this arrival should be close to the seismic frequency range, and we see here that this row of spikes has much higher frequencies than those typical of seismic events. This must be an interference from a distant source that was picked up by the electrodes.

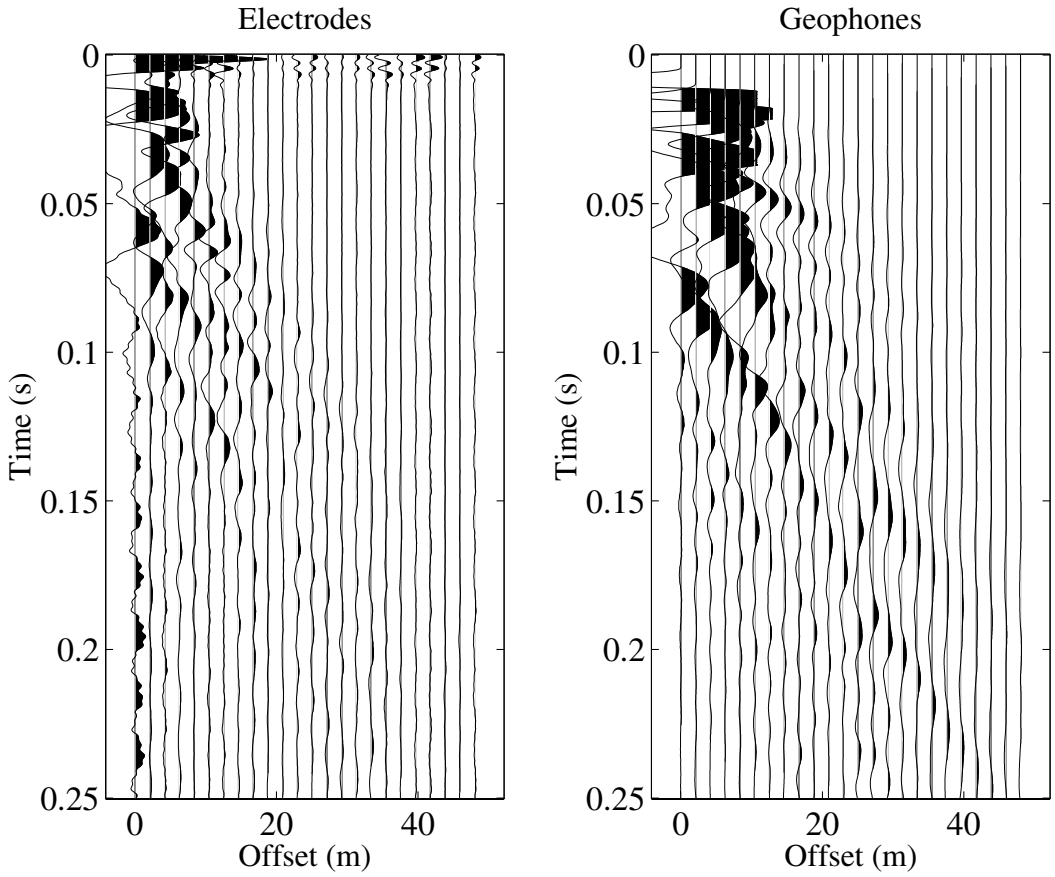

Figure 3.22: *Comparison between electrode and geophone measurements.*

3.9 Conclusions

In this chapter we have defined the one-way operators that are to be used in our seismo-electric survey simulations. We began defining the composition operator that composes the two-way wavefields from one-way wavefields and its inverse that decomposes the two-way wavefields back to one-way wavefields. This is done for the SH-TE and P-SV-TM couplings.

With the composition operator we have determined the reflection and transmission coefficients in the (p_1, ω) domain via a scattering matrix. This has been done for porous/porous and porous/vacuum interfaces. Next we have shown and discussed some results where we see the dependency of the coefficients with the horizontal slowness. We have seen how the conversion from different inci-

dent wavefields takes place and it strongly depends on p_1. We have also shown reflection coefficients depending on the contrasts in certain medium properties, namely ion concentration, porosity or permeability. From this we have seen how the seismo-electric response of an interface is proportional to the contrast in the media properties.

We have constructed a very simple one-way reflection model with the reflection coefficients and the wave extrapolation operators where we can already see the arrival times of reflections and conversions between different wavefields. This model is done in the (k_1, ω) domain, and via a Fourier transformation the results are shown in the (x_1, t) domain. This first step is a simplistic approach, yet it greatly helps understanding the seismo-electric reflection.

In the next section we have derived the composition and decomposition of wavefields at the source and receivers. In our next model the two-way source parameters were decomposed at the source into the one-way wavefields that propagate in our previous model. When these one-way wavefields are reflected back to the surface they are composed back to the two-way wavefields measured at the receivers. Via these operators we not only can simulate any receiver, but also swicht on and off certain wavefields to better study the interaction of different combinations of wavefields, as well as sources and receivers.

Finally we showed a couple of examples, one-way and two-way reflections from SH-TE and P-SV-TM couplings. From these we conclude that there are indeed multiple interactions between the seismic and electromagnetic wavefields in both directions, i.e. seismic to electromagnetic and vice versa, making this effect a more complicated case than just conversion from fast-P to electromagnetic waves.

In the coming chapter we will see how we organize the one-way operators to simulate a vertical seismo-electric profile and wellbore to wellbore seismo-electric measurements.

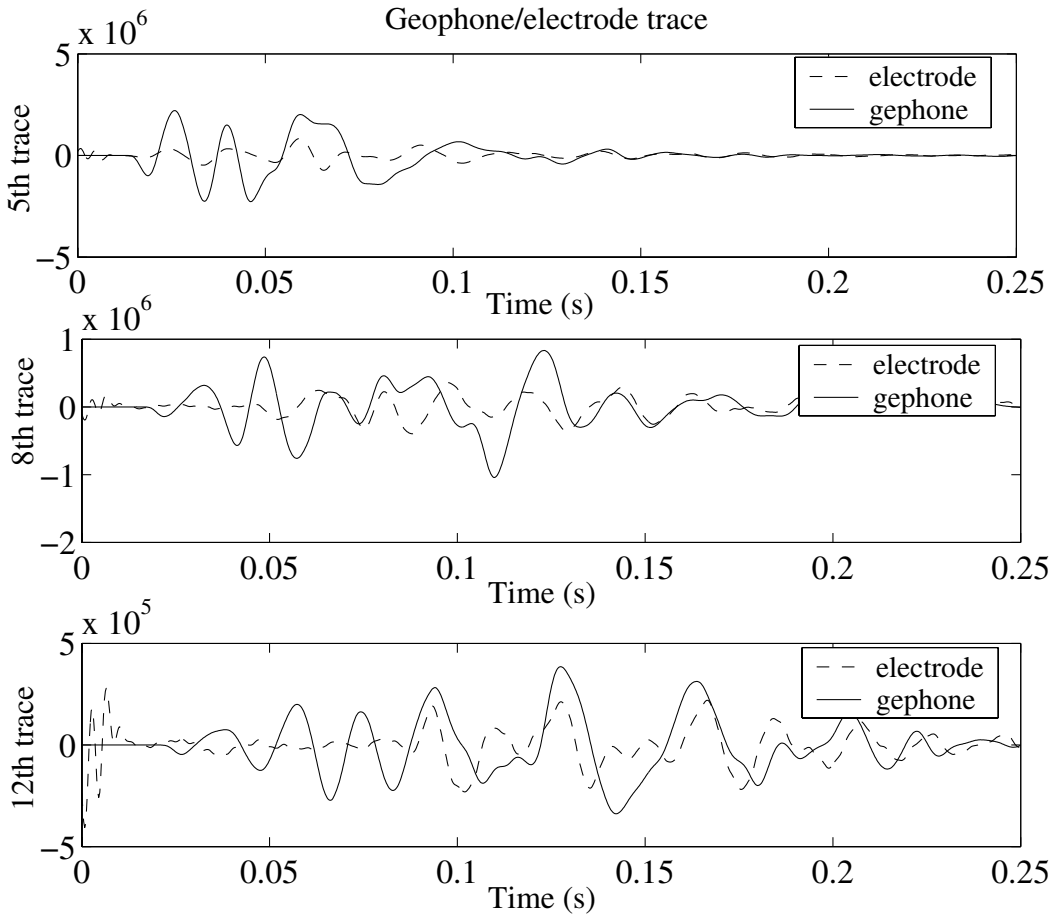

Figure 3.23: *Trace to trace Comparison between electrode and geophone measurements.*

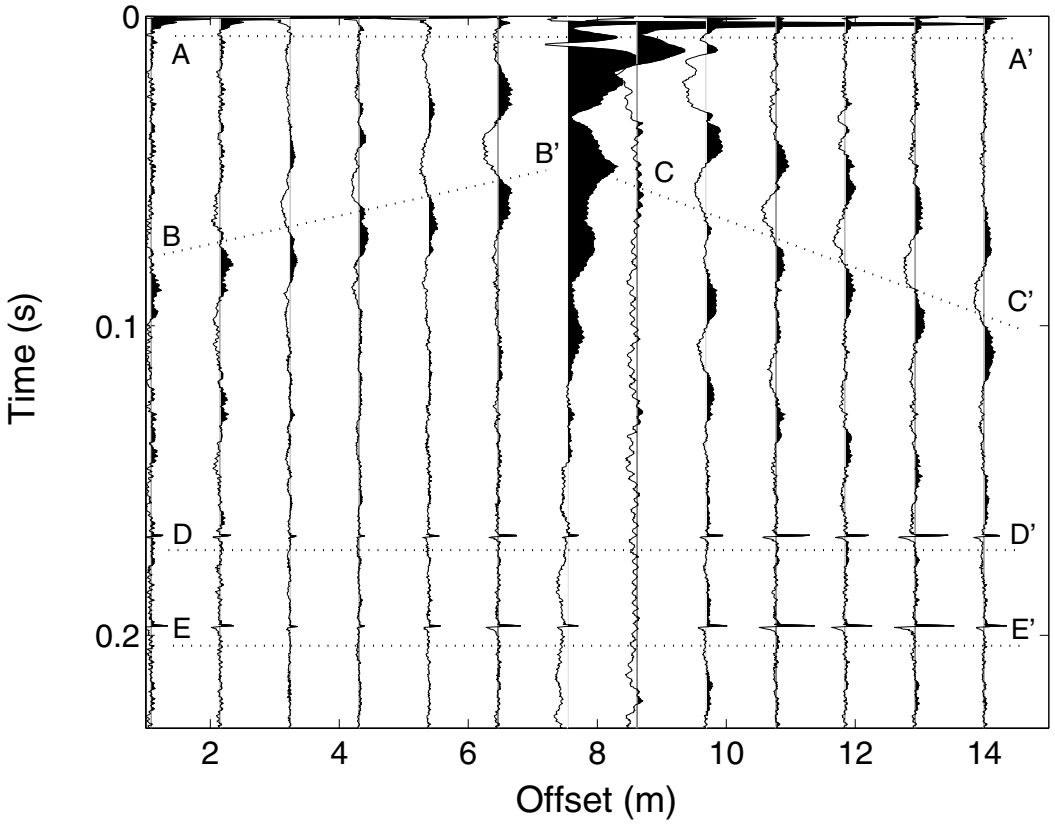

Figure 3.24: E_1 *electrodes measurements.*

Chapter 4

The Reflectivity method

4.1 Introduction

In the previous chapter we described the one-way operators to simulate a seismo-electric survey. In this chapter we describe further applications of the same one-way operators defined in the previous chapter. First we use these operators to derive global reflection and transmission coefficients in a similar way as Kennett [10] does, and in later sections of the chapter we use them to simulate a vertical seismo-electric profile (VSEP) and an electro-kinetic wellbore to wellbore survey.

4.2 Global reflection and transmission responses including internal multiples

In this section we derive recurrent relations for the global reflection and transmission coefficients. Local and global scattering matrices are defined by

$$\begin{pmatrix} \tilde{\mathbf{P}}^{u,-}_{\mathrm{a,n}} \\ \tilde{\mathbf{P}}^{l,+}_{\mathrm{a,n}} \end{pmatrix} = \begin{pmatrix} \tilde{\mathbf{r}}^{+}_{\mathrm{a,n}} & \tilde{\mathbf{t}}^{-}_{\mathrm{a,n}} \\ \tilde{\mathbf{t}}^{+}_{\mathrm{a,n}} & \tilde{\mathbf{r}}^{-}_{\mathrm{a,n}} \end{pmatrix} \begin{pmatrix} \tilde{\mathbf{P}}^{u,+}_{\mathrm{a,n}} \\ \tilde{\mathbf{P}}^{l,-}_{\mathrm{a,n}} \end{pmatrix} \tag{4.1}$$

and

$$\begin{pmatrix} \tilde{\mathbf{P}}^{-}_{\mathrm{a,0}} \\ \tilde{\mathbf{P}}^{l,+}_{\mathrm{a,n}} \end{pmatrix} = \begin{pmatrix} \tilde{\mathbf{R}}^{+}_{\mathrm{a,n}} & \tilde{\mathbf{T}}^{-}_{\mathrm{a,n}} \\ \tilde{\mathbf{T}}^{+}_{\mathrm{a,n}} & \tilde{\mathbf{R}}^{-}_{\mathrm{a,n}} \end{pmatrix} \begin{pmatrix} \tilde{\mathbf{P}}^{+}_{\mathrm{a,0}} \\ \tilde{\mathbf{P}}^{l,-}_{\mathrm{a,n}} \end{pmatrix} \tag{4.2}$$

where $\tilde{\mathbf{r}}^{\pm}_{n}$ and $\tilde{\mathbf{t}}^{\pm}_{n}$ are the local reflection and transmission coefficients at interface n respectively, and $\tilde{\mathbf{R}}^{\pm}_{n}$ and $\tilde{\mathbf{T}}^{\pm}_{n}$ are the global reflection and transmission coefficients for the complete stack of layers from z_0 to z_n. The local coefficients

take into account only the properties of the media right above and below the interface, just like those calculated in the previous chapter, while the global coefficients take into account all the reflections and transmissions among the layers above the n^{th} interface, including the internal multiples.

4.2.1 Upgoing waves

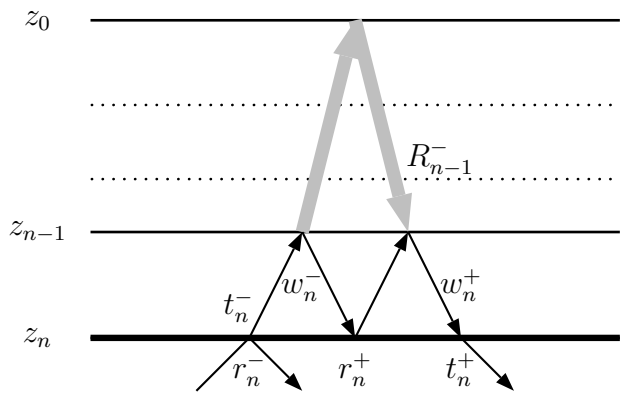

Figure 4.1: Global reflection coefficient

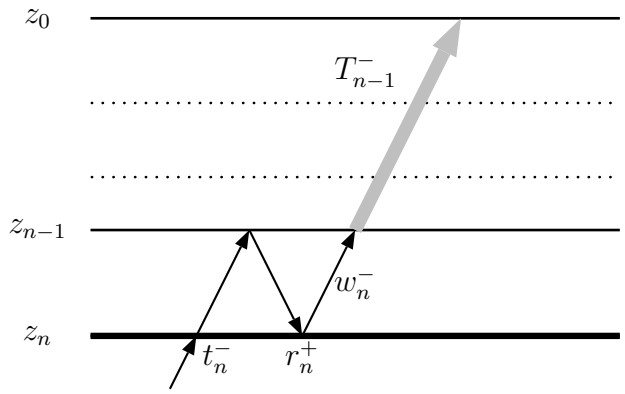

Figure 4.2: Global transmission coefficient

In the case of an upgoing source wavefield below interface z_n substituting

$\tilde{\mathbf{P}}_n^{l,+} = \tilde{\mathbf{R}}_n^- \tilde{\mathbf{P}}_n^{l,-}$ into equation (4.1) gives

$$\begin{pmatrix} \tilde{\mathbf{P}}_n^{u,-} \\ \tilde{\mathbf{R}}_n^- \tilde{\mathbf{P}}_n^{l,-} \end{pmatrix} = \begin{pmatrix} \tilde{\mathbf{r}}_n^+ & \tilde{\mathbf{t}}_n^- \\ \tilde{\mathbf{t}}_n^+ & \tilde{\mathbf{r}}_n^- \end{pmatrix} \begin{pmatrix} \tilde{\mathbf{M}}_n \tilde{\mathbf{P}}_n^{u,-} \\ \tilde{\mathbf{P}}_n^{l,-} \end{pmatrix} \tag{4.3}$$

where $\tilde{\mathbf{M}}_n$ is

$$\tilde{\mathbf{M}}_n = \tilde{\mathbf{w}}_n^+ \tilde{\mathbf{R}}_{n-1}^- \tilde{\mathbf{w}}_n^- \tag{4.4}$$

From the upper row of equation (4.3) we have

$$\tilde{\mathbf{P}}_n^{u,-} = \left(\tilde{\mathbf{I}} - \tilde{\mathbf{r}}_n^+ \tilde{\mathbf{M}}_n\right)^{-1} \tilde{\mathbf{t}}_n^- \tilde{\mathbf{P}}_n^{l,-} \tag{4.5}$$

If we substitute this into the lower row of equation (4.3) we obtain an equation that holds for any $\tilde{\mathbf{P}}_n^{l,-}$ and yields the upgoing global reflection coefficient

$$\tilde{\mathbf{R}}_n^- = \tilde{\mathbf{r}}_n^- + \tilde{\mathbf{t}}_n^+ \tilde{\mathbf{M}}_n \left(\tilde{\mathbf{I}} - \tilde{\mathbf{r}}_n^+ \tilde{\mathbf{M}}_n\right)^{-1} \tilde{\mathbf{t}}_n^- \tag{4.6}$$

To obtain the global upgoing transmission coefficient we will assume we know the one for level z_{n-1}, $\tilde{\mathbf{T}}_{n-1}^-$. Then we can define $\tilde{\mathbf{P}}_0^-$ as

$$\tilde{\mathbf{P}}_0^- = \tilde{\mathbf{T}}_{n-1}^- \tilde{\mathbf{w}}_n^- \tilde{\mathbf{P}}_n^{u,-} \tag{4.7}$$

and substituting $\tilde{\mathbf{P}}_{u,n}^-$ from equation (4.5) into equation (4.7) gives

$$\tilde{\mathbf{P}}_0^- = \tilde{\mathbf{T}}_{n-1}^- \tilde{\mathbf{w}}_n^- \left(\tilde{\mathbf{I}} - \tilde{\mathbf{r}}_n^+ \tilde{\mathbf{M}}_n\right)^{-1} \tilde{\mathbf{t}}_n^- \tilde{\mathbf{P}}_n^{l,-} \tag{4.8}$$

Applying equation (4.2) to interface z_n gives $\tilde{\mathbf{P}}_0^- = \tilde{\mathbf{T}}_n^- \tilde{\mathbf{P}}_n^{l,-}$, then substituting $\tilde{\mathbf{P}}_0^-$ into equation (4.8) gives us an expression for $\tilde{\mathbf{T}}_n^-$ as a function of the upgoing global transmission coefficient of the previous interface

$$\tilde{\mathbf{T}}_n^- = \tilde{\mathbf{T}}_{n-1}^- \tilde{\mathbf{w}}_n^- \left(\tilde{\mathbf{I}} - \tilde{\mathbf{r}}_n^+ \tilde{\mathbf{M}}_n\right)^{-1} \tilde{\mathbf{t}}_n^-. \tag{4.9}$$

4.2.2 Downgoing waves

For a source downgoing wavefield at z_0, equation (3.19) together with $\tilde{\mathbf{P}}_n^{l,+} = \tilde{\mathbf{T}}_n^+ \tilde{\mathbf{P}}_0^+$ reads

$$\begin{pmatrix} \tilde{\mathbf{P}}_n^{u,-} \\ \tilde{\mathbf{T}}_n^+ \tilde{\mathbf{P}}_0^+ \end{pmatrix} = \begin{pmatrix} \tilde{\mathbf{r}}_n^+ & \tilde{\mathbf{t}}_n^- \\ \tilde{\mathbf{t}}_n^+ & \tilde{\mathbf{r}}_n^- \end{pmatrix} \begin{pmatrix} \tilde{\mathbf{w}}_n^+ \tilde{\mathbf{T}}_{n-1}^+ \tilde{\mathbf{P}}_0^+ + \tilde{\mathbf{M}}_n \tilde{\mathbf{P}}_n^{u,-} \\ 0 \end{pmatrix} \tag{4.10}$$

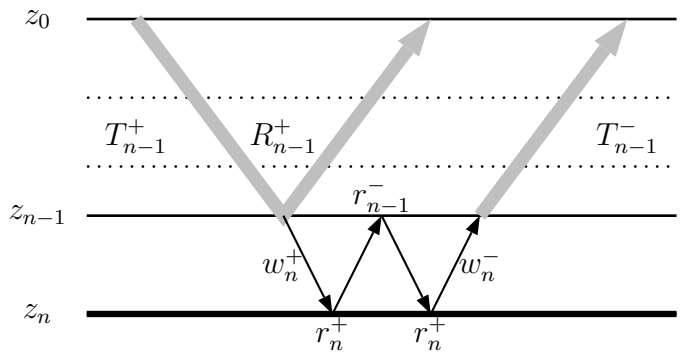

Figure 4.3: Global reflection coefficient

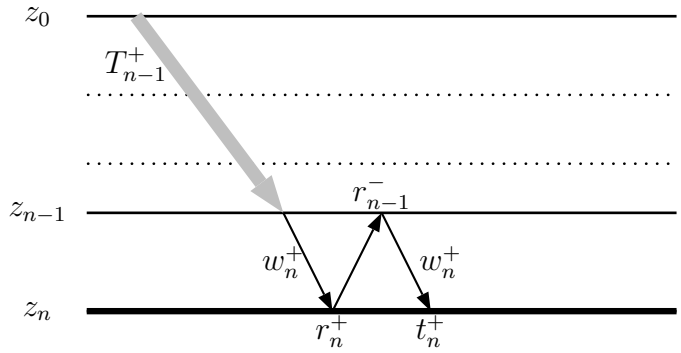

Figure 4.4: Global transmission coefficient

From the upper row of (4.10) we have

$$\tilde{\mathbf{P}}_n^{u,-} = \left(\tilde{\mathbf{I}} - \tilde{\mathbf{r}}_n^+ \tilde{\mathbf{M}}_n\right)^{-1} \tilde{\mathbf{r}}_n^+ \tilde{\mathbf{w}}_n^+ \tilde{\mathbf{T}}_{n-1}^+ \tilde{\mathbf{P}}_0^+. \tag{4.11}$$

If we substitute this in the lower row of (4.10) we obtain an expression that holds for any $\tilde{\mathbf{P}}_0^+$. From that expression we can extract the downgoing global transmission coefficient

$$\tilde{\mathbf{T}}_n^+ = \tilde{\mathbf{t}}_n^+ \tilde{\mathbf{w}}_n^+ \left(\tilde{\mathbf{I}} + \tilde{\mathbf{R}}_{n-1}^- \tilde{\mathbf{w}}_n^- \left(\tilde{\mathbf{I}} - \tilde{\mathbf{r}}_n^+ \tilde{\mathbf{M}}_n\right)^{-1} \tilde{\mathbf{r}}_n^+ \tilde{\mathbf{w}}_n^+\right) \tilde{\mathbf{T}}_{n-1}^+ \tag{4.12}$$

$$= \tilde{\mathbf{t}}_n^+ \left(\tilde{\mathbf{I}} + \tilde{\mathbf{w}}_n^+ \tilde{\mathbf{R}}_{n-1}^- \tilde{\mathbf{w}}_n^- \sum_{k=1}^{\infty} (\mathbf{r}_n^+ \tilde{\mathbf{w}}_n^+ \tilde{\mathbf{R}}_{n-1}^- \tilde{\mathbf{w}}_n^-)^k \tilde{\mathbf{r}}_n^+\right) \tilde{\mathbf{w}}_n^+ \tilde{\mathbf{T}}_{n-1}^+ \tag{4.13}$$

$$= \tilde{\mathbf{t}}_n^+ \left(\tilde{\mathbf{I}} - \tilde{\mathbf{M}}_n \tilde{\mathbf{r}}_n^+\right)^{-1} \tilde{\mathbf{w}}_n^+ \tilde{\mathbf{T}}_{n-1}^+. \tag{4.14}$$

Applying the upper row of equation (3.31) to the $(n-1)^{th}$ interface, and substituting $\tilde{\mathbf{P}}^{l,-}_{n-1} = \mathbf{w}^{-}_{n}\tilde{\mathbf{P}}^{u,-}_{n}$ yields

$$\tilde{\mathbf{P}}^{-}_{0} = \tilde{\mathbf{R}}^{+}_{n-1}\tilde{\mathbf{P}}^{+}_{0} + \tilde{\mathbf{T}}^{-}_{n-1}\mathbf{w}^{-}_{n}\tilde{\mathbf{P}}^{u,-}_{n}. \tag{4.15}$$

Substituting $\tilde{\mathbf{P}}^{u,-}_{n}$ from equation (4.11) gives us an expression that holds for any $\tilde{\mathbf{P}}^{+}_{0}$ and therefore gives the downgoing global reflection coefficient

$$\tilde{\mathbf{R}}^{+}_{n} = \tilde{\mathbf{R}}^{+}_{n-1} + \tilde{\mathbf{T}}^{-}_{n-1}\tilde{\mathbf{w}}^{-}_{n}\tilde{\mathbf{r}}^{+}_{n}\left(\tilde{\mathbf{I}} - \tilde{\mathbf{M}}_{n}\tilde{\mathbf{r}}^{+}_{n}\right)^{-1}\tilde{\mathbf{w}}^{+}_{n}\tilde{\mathbf{T}}^{+}_{n-1}. \tag{4.16}$$

In the expressions for both the global reflection and transmission coefficients we find the term $(\tilde{\mathbf{I}} - \tilde{\mathbf{M}}_{n}\tilde{\mathbf{r}}^{+}_{n})^{-1}$. If we use the series expansion

$$(1-\varepsilon)^{-1} = 1 + \varepsilon + \varepsilon^{2} + \varepsilon^{3} + \varepsilon^{4} + ... \tag{4.17}$$

then we have that

$$(\tilde{\mathbf{I}} - \tilde{\mathbf{M}}_{n}\tilde{\mathbf{r}}^{+}_{n})^{-1} = \tilde{\mathbf{I}} + \tilde{\mathbf{M}}_{n}\tilde{\mathbf{r}}^{+}_{n} + \tilde{\mathbf{M}}_{n}\tilde{\mathbf{r}}^{+}_{n}\tilde{\mathbf{M}}_{n}\tilde{\mathbf{r}}^{+}_{n} + \tilde{\mathbf{M}}_{n}\tilde{\mathbf{r}}^{+}_{n}\tilde{\mathbf{M}}_{n}\tilde{\mathbf{r}}^{+}_{n}\tilde{\mathbf{M}}_{n}\tilde{\mathbf{r}}^{+}_{n} + ... \tag{4.18}$$

Taking into account that $\tilde{\mathbf{M}}_{n} = \tilde{\mathbf{w}}^{+}_{n}\tilde{\mathbf{R}}^{-}_{n-1}\tilde{\mathbf{w}}^{-}_{n}$, then

$$\begin{aligned}(\tilde{\mathbf{I}} - \tilde{\mathbf{M}}_{n}\tilde{\mathbf{r}}^{+}_{n})^{-1} = \tilde{\mathbf{I}} &+ \tilde{\mathbf{w}}^{+}_{n}\tilde{\mathbf{R}}_{n-1}\tilde{\mathbf{w}}^{-}_{n}\tilde{\mathbf{r}}^{+}_{n} + \tilde{\mathbf{w}}^{+}_{n}\tilde{\mathbf{R}}_{n-1}\tilde{\mathbf{w}}^{-}_{n}\tilde{\mathbf{r}}^{+}_{n}\tilde{\mathbf{w}}^{+}_{n}\tilde{\mathbf{R}}_{n-1}\tilde{\mathbf{w}}^{-}_{n}\tilde{\mathbf{r}}^{+}_{n} + \\ &\tilde{\mathbf{w}}^{+}_{n}\tilde{\mathbf{R}}_{n-1}\tilde{\mathbf{w}}^{-}_{n}\tilde{\mathbf{r}}^{+}_{n}\tilde{\mathbf{w}}^{+}_{n}\tilde{\mathbf{R}}_{n-1}\tilde{\mathbf{w}}^{-}_{n}\tilde{\mathbf{r}}^{+}_{n}\tilde{\mathbf{w}}^{+}_{n}\tilde{\mathbf{R}}_{n-1}\tilde{\mathbf{w}}^{-}_{n}\tilde{\mathbf{r}}^{+}_{n} + ...\end{aligned} \tag{4.19}$$

We see now how the series expansion of this term describes the internal multiples reflecting on each layer.

In the next sections we make use of these global coefficients for a VSEP simulation, a multilayered medium and a wellbore to wellbore survey.

4.3 Vertical Seismo-Electric Profile

In this section we describe the use of the global coefficients to model a VSEP survey. Unlike in the previous chapter, this forward simulation will be calculated in the (k_1, x_3, ω) domain, and then Fourier transformed to the (x_1, x_3, t) domain in which the results are shown.

4.3.1 One-way Vertical Seismo-Electric Profile

In the Vertical Seismo-electric Profile we use electrodes along the well as receivers and a seismic source at the surface, or the other way around, geophones in the well as receivers and an electromagnetic source at the surface.

In the previous sections we have calculated the global coefficients for a generic stack of n layers. In the present section we derive an expression for the up and downgoing wavefields in a VSEP survey. To do this we need to know all the global reflection and transmission coefficients of all the different stacks of layers in a multilayered medium.

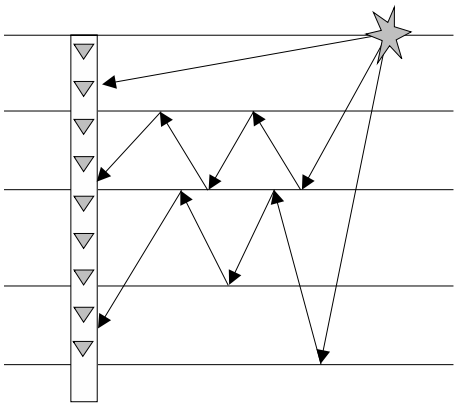

Figure 4.5: *Vertical seismo-electric profile*

We will use the index m to denote the level from which we are calculating the coefficients, and move it from top to bottom and back to top. This way we obtain the coefficients from all different levels. Next we can calculate the up and downgoing wavefields for the VSEP model.

Two wavefields arrive at each receiver, up and downgoing, denoted as

$$\tilde{\mathbf{P}}_l(z_m) = \tilde{\mathbf{P}}_l^+(z_m) + \tilde{\mathbf{P}}_l^-(z_m) \tag{4.20}$$

where these two are

$$\tilde{\mathbf{P}}^+(z_m) = \left(\tilde{\mathbf{I}} - \tilde{\mathbf{R}}^-(z_{m-1})\tilde{\mathbf{R}}^+(z_m)\right)^{-1} \tilde{\mathbf{T}}^+(z_m) \tag{4.21}$$

$$\tilde{\mathbf{P}}^-(z_m) = \left(\tilde{\mathbf{I}} - \tilde{\mathbf{R}}^+(z_m)\tilde{\mathbf{R}}^-(z_{m-1})\right)^{-1} \tilde{\mathbf{R}}^+(z_m)\tilde{\mathbf{T}}^+(z_m) \tag{4.22}$$

where the coefficients $\tilde{\mathbf{R}}^{\pm}(z_m)$ and $\tilde{\mathbf{T}}^{\pm}(z_m)$ are the global coefficients from level z_m and they correspond to the complete stack of layers between the level z_m and the bottom of the multilayered medium for $\tilde{\mathbf{R}}^{+}(z_m)$ and $\tilde{\mathbf{T}}^{+}(z_m)$, or between the level z_m and the top for $\tilde{\mathbf{R}}^{-}(z_m)$ and $\tilde{\mathbf{T}}^{-}(z_m)$. At this stage we no longer use the subscript with the set of layers to which the coefficients are calculated since it is always done between the layer z_m and the top or bottom and it is redundant.

Looking at figure 4.6 we understand these equations if we follow the direction of the arrows in the figure and look at the equations from right to left. On the left graph we see the wavefields taken into account for $\tilde{\mathbf{P}}_n^+$ in equation (4.21), i.e. the downgoing wavefield recorded at level z_m. In the first place we use $\tilde{\mathbf{T}}_n^+$, the global transmission coefficient from the surface where the source is, to the level where the receiver is followed by the multiples on that level $\left(\tilde{\mathbf{I}} - \tilde{\mathbf{R}}_n^+ \tilde{\mathbf{R}}_{n-1}^-\right)^{-1}$. This is similar to equation (4.17), but in this case the propagators are already included in the global coefficients.

We see on the right of figure 4.6 the wavefields taken into account for $\tilde{\mathbf{P}}_n^-$ in equation (4.22). We find the same elements as in the previous plus the global reflection coefficient $\tilde{\mathbf{R}}_n^+$ that includes the reflection of the wavefield in the interface at z_m.

So far we obtain the one-way VSEP. In order to obtain the two-way VSEP we need to decompose the two-way source and compose back at the receivers. For that we need the source decomposition and receiver composition operators. In this model we simulate neither the effects of the wellbore nor the waves that propagate inside the wellbore itself.

4.3.2 Two-way Vertical Seismo-Electric Profile

In this section we include the effects of the source and receivers into the previously derived one-way VSEP wavefields. This way we obtain the results of the simulation in measurable two-way wavefields.

In the previous chapter we derived an expression of the source decomposition operator and receiver composition operator for the seismo-electric coupling. In this chapter we use the expressions derived there and we specify them for this case in particular.

In a vertical seismo-electric profile we put the source on the surface and the receivers along the wellbore. This means that the wavefields coming out of the source are all downgoing while the receivers at the wellbore measure wavefields coming from above and below their level.

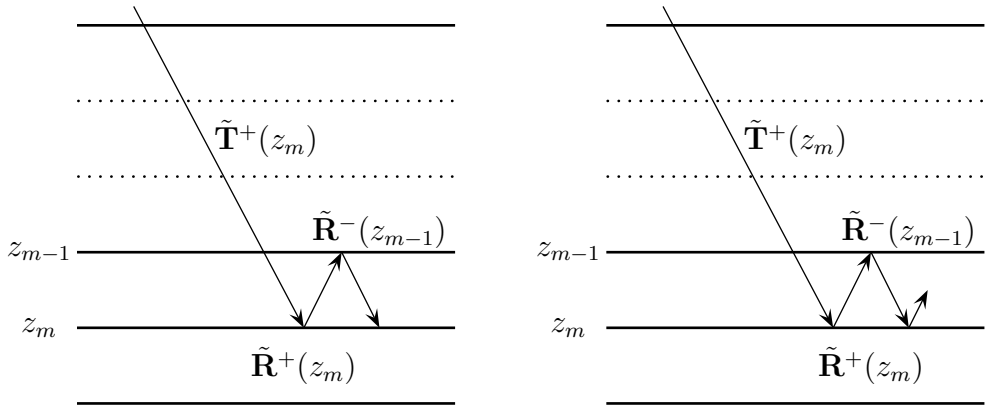

Figure 4.6: *Left and right we see a scheme of the up and downgoing wavefields, respectively in the vertical seismo-electric profile as described by equations (4.21) and (4.22).*

This survey setup allows to use the same source decomposition operator we defined in section 3.7.2. When it comes to using a receiver composition operator for a VSEP survey simulation things are different since we need to compose the up and downgoing waves separately. Therefore we use two operators, $\tilde{\mathbf{C}}_r^-$ for upgoing and $\tilde{\mathbf{C}}_r^+$ for downgoing wavefields.

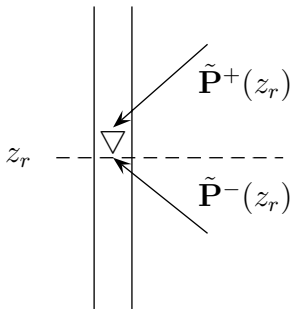

Figure 4.7: *Receiver in a well in a VSEP setup*

The receiver composition operator we use comes from section 3.6,

$$\tilde{\mathbf{Q}}'_{2,\mathrm{a}}(z_r) = \tilde{\mathbf{C}}^{-}_{\mathrm{r,a}}(z_r)\tilde{\mathbf{P}}^{-}_{\mathrm{a}}(z_r) + \tilde{\mathbf{C}}^{+}_{\mathrm{r,a}}(z_r)\tilde{\mathbf{P}}^{+}_{\mathrm{a}}(z_r), \tag{4.23}$$

where $\tilde{\mathbf{C}}_r^{\pm}$ are defined in equation (3.78).

4.3.3 Results

In this section we show the results of our vertical seismo-electric profile simulations. First we present the results of the one-way VSEP models in the (x_3, t) and (x_1, x_3, t) domains followed by the results of the two-way VSEP models again in both domains. As mentioned before we performed all the calculations in the (x_3, ω) and (k_1, x_3, ω) domains and the results were Fourier transformed to the (x_3, t) and (x_1, x_3, t) domains respectively.

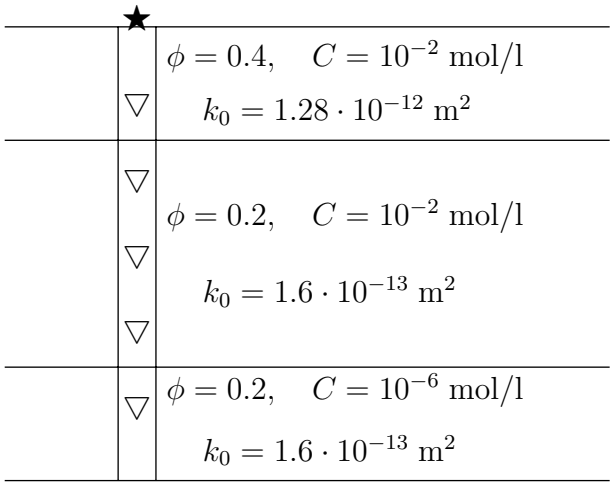

Figure 4.8: *VSEP setup, we use this configuration for all of the models.*

We apply all the VSEP propagation models and later, all wellbore to wellbore models to the same medium, so they can be easily compared and referred. A sketch of this medium can be seen in figure 4.8. This medium is composed of three layers and two interfaces in between. The first interface between the upper and the middle layer is a contrast in porosity, from $\phi = 0.4$ to $\phi = 0.2$. The second interface, between the second and the third layer is a contrast in pore fluid ion concentration, from $C = 10^{-2}$M to $C = 10^{-6}$M. Table 4.1 contains the rest of the medium parameters, these parameters remain constant in all directions of space. There are 30 receivers placed along the wellbore every 5m and the source is at the surface. The interfaces are located at depths of 40m and 120m, where the receivers 8 and 24 are.

Parameter	value
ρ^{s}	$2.5 \cdot 10^3\ \mathrm{kg/m^3}$
η	$10^{-3}\ \mathrm{Pa \cdot m}$
K^{s}	$4 \cdot 10^{10}\ \mathrm{Pa}$
K^{fr}	$4 \cdot 10^{9}\ \mathrm{Pa}$
G^{fr}	$9 \cdot 10^{9}\ \mathrm{Pa}$
K^{f}	$2.2 \cdot 10^{9}\ \mathrm{Pa}$
α_∞	3
m	8
ϵ_r^f	80
ϵ_r^s	4

Table 4.1: *Medium parameters for the VSEP and wellbore to wellbore simulations*

One way VSEP simulations in the (x_3, t) domain.

In this section we present the results of the one-way vertical seismo-electric profile simulations in the (x_3, t) domain.

Although the interactions between different seismic wavefields is not within the scope of this research, in the coming one-way results the complete range of posible reflections between different wavefields are shown. This is done to help identifying the different arrivals in the VSEP two-way results where, for simplicity, we have selected the most relevant results of each case, i.e. those that contain the seismo-electric conversion.

In Figure 4.9 we see the one-way vertical seismo-electric profile of the SH-TE coupling wavefields in the (x_3, t) domain. There are four graphs, in the upper two graphs we see the horizontal shear waves reflected from incident horizontal shear and TE waves, respectively, and in the lower two graphs we see the reflected TE waves from incident horizontal shear and TE waves, respectively.

In the first graph we see the downgoing horizontal shear wave and very lightly the reflection from the first interface. The reflections take place at the 8^{th} receiver and 0.02s and at the 24^{th} receiver and 0.06s. On the upper right graph we see the horizontal shear waves generated at both interfaces when a TE wave travels down from the surface. Because this wave travels at very high velocities the up and down horizontal shear waves generated appear to be generated simultaneously.

In the lower left graph we see the TE waves generated when a horizontal shear wave travels down from the surface and crosses the two interfaces where con-

version takes place and up and downgoing electromagnetic waves are generated at both spots. The times and receivers where the conversion takes place are the same as in the upper left graph, which is logical since both cases are reflections from downgoing horizontal shear waves. In the lower right graph we see a TE wave reflected when a TE wave travels down along the receivers. Due to the velocity of the electromagnetic wave this arrival appears to be instantaneous.

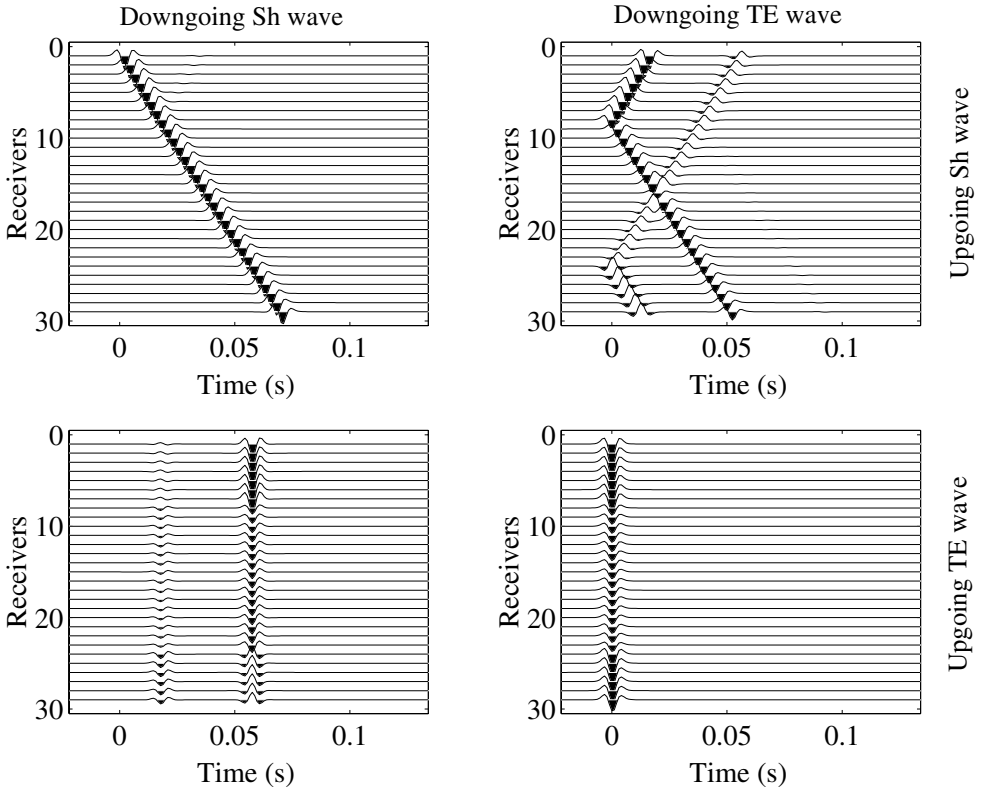

Figure 4.9: *Plane wave response for the one-way VSEP simulation of the SH-TE coupling.*

In figure 4.10 we see the one-way vertical seismo-electric profile of the P-SV-TM coupling. This is a similar arrangement as the one in previous figure: there are three columns of graphs. On the first column we find the Sv and TM wavefields generated as a fast-P wave travels down the wellbore. On the second column we see the same as an Sv wave travels down the wellbore, and in the

last column we find the fast-P and Sv wavefields generated as a TM wavefield travels down the wellbore and hits the interfaces. Note that in the third graph of the second row there are indeed two conversions from TM to Sv, but the second one is weaker than the first and therefore it does not show so clearly. Note also how the polarity changes when the shear wave generates a TM wavefield, same as in the SH-TE coupling, but not when the incident wave is a fast-P wave.

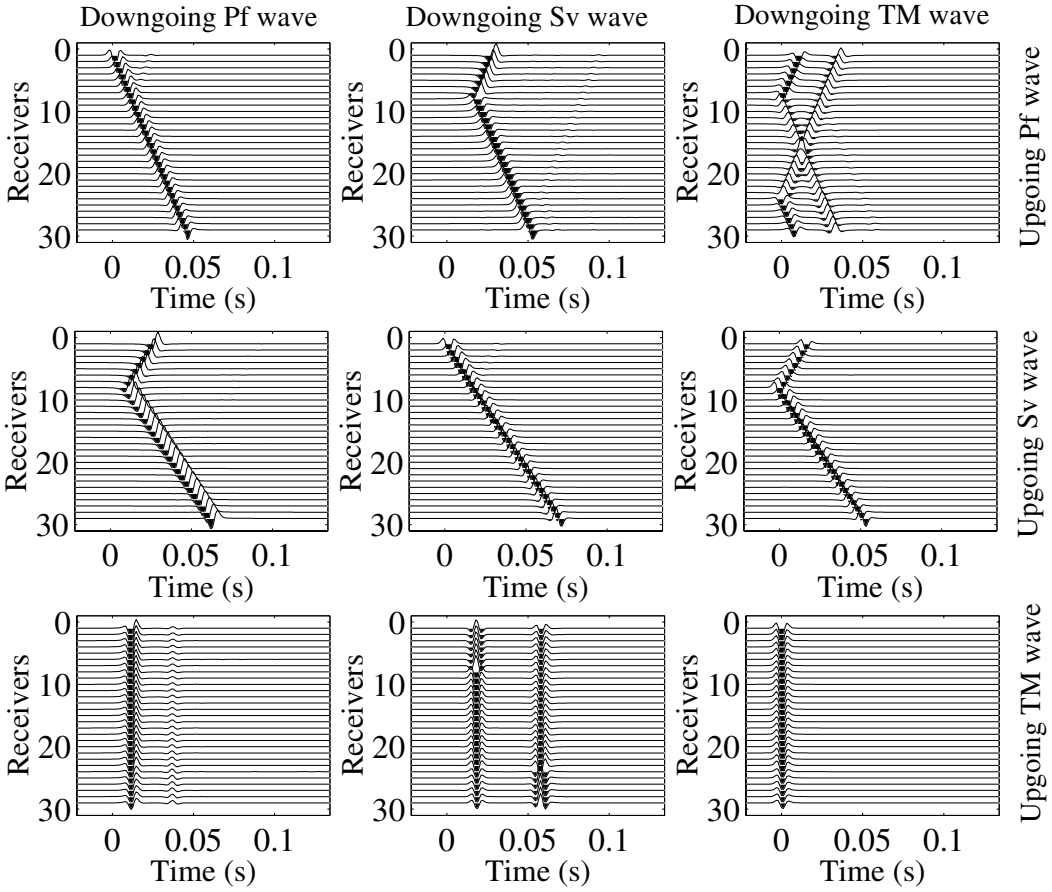

Figure 4.10: *Plane wave response for the one-way VSEP simulation of the P-SV-TM coupling.*

One-way VSEP simulations in the (x_1, x_3, t) domain

In this section we present the results of the VSEP simulation in the (x_1, x_3, t) domain. We have included the propagation in the x_1 direction to the previous simulation. This way the model gives us information on the direction perpendicular to the wellbore. Effectively this will be as if we placed a line of receivers in the x_1 direction for each x_3 level as can be seen in figure 4.11. This extra dimension implies that we do the calculation in the (k_1, x_3, ω) domain, and from there we Fourier transform to the (x_1, x_3, t) domain. The solution comes finally as a datacube in x_1, x_3 and t where we see how the wavefields propagate through the x_1, x_3 plane with time. Since we take x_1 into account the wavefields are no longer plane waves, but cylindrical waves with geometrical spreading that propagate through the x_1, x_3 plane and show attenuation due to the geometrical spreading.

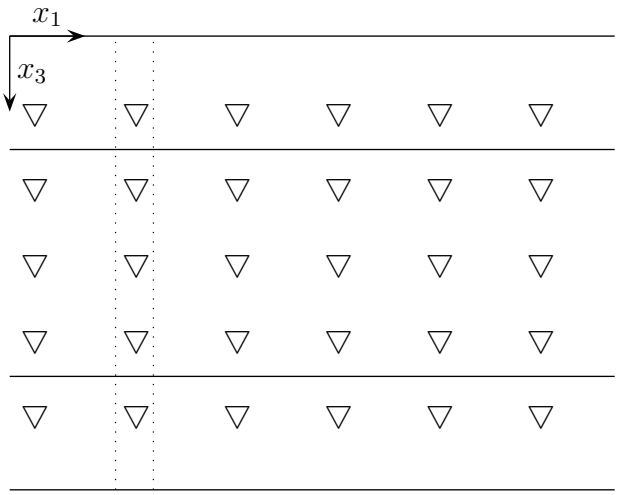

Figure 4.11: *Setup for the (x_1, x_3, t) VSEP simulation.*

In Figure 4.12 we present results similar to Figures 4.9 and 4.10, but in this case, as we said before, we are looking at the (x_3, t) slice of a (x_1, x_3, t) datacube. The main difference between the previous VSEP and the current VSEP results is the attenuation of the arrivals in the vertical direction. This is due to the fact that we take the propagation of the wave into account in two direcctions of space x_1 and x_3.

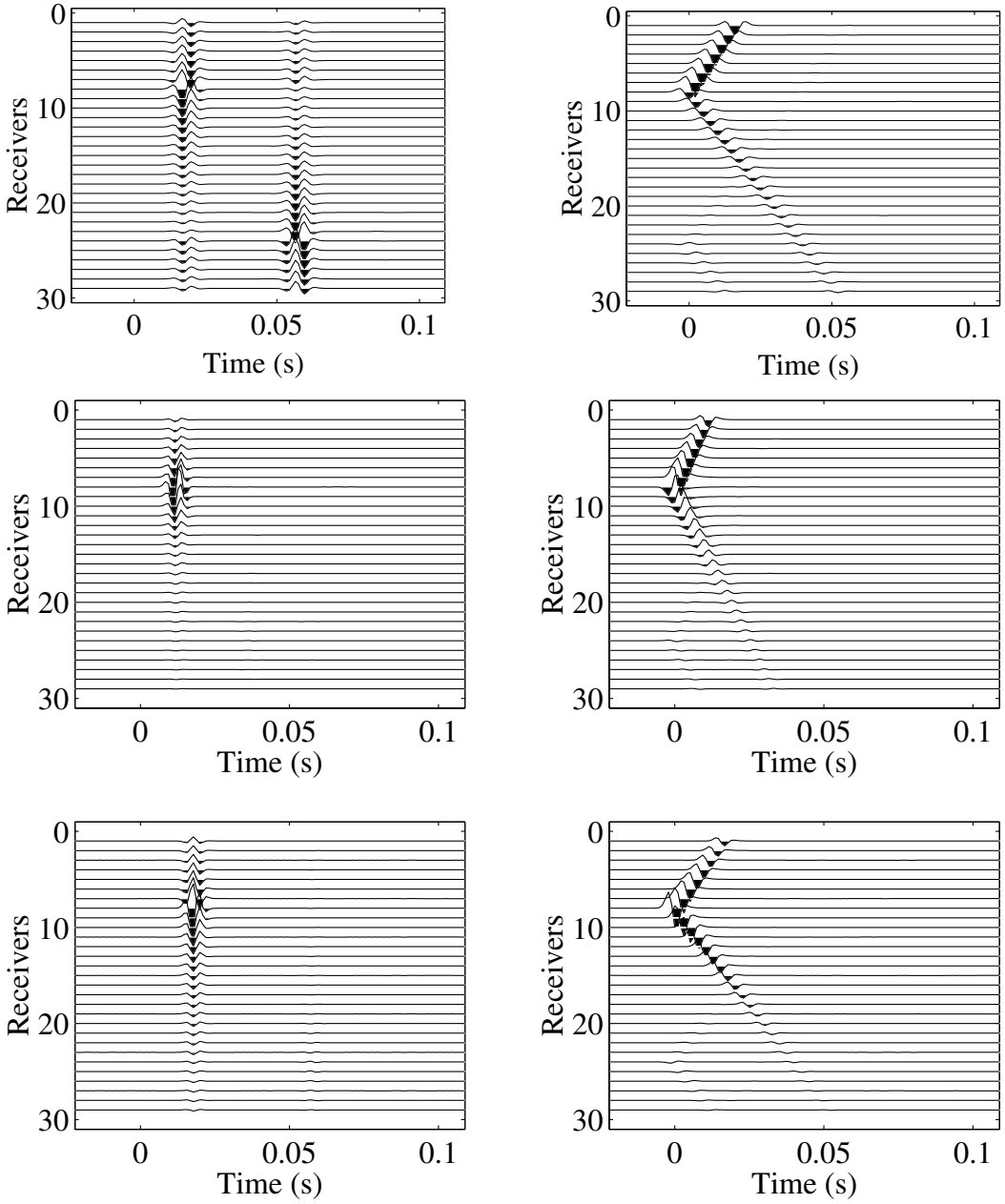

Figure 4.12: *Line source response for the one-way VSEP simulation. Upper graphs: Left: conversions from Sh to TE wave and vice versa. Middle graphs: conversions from Pf to Tm and vice versa. Lower graphs: conversions from Sv to Tm and vice versa.*

One-way VSEP Timeslices

In this section we show some images of the x_1x_3 plane of the one-way VSEP datacube. The x_1x_3 planes can be seen as a series of snapshots of the one-way wavefields propagating along this plane. We have chosen the timeslices of certain interesting wave conversions, like between horizontal shear and TE waves, or between fast-P and TM waves. There are other interesting conversions to be looked at like those from electromagnetic to seismic waves where seismic plane waves are reflected back to the surface, but to keep things simple we show just the two conversions first mentioned.

In Figure 4.13 we show a serie of x_1x_3 snapshots of the VSEP datacube in the SH-TE coupling. The pictures show when the conversion from horizontal shear to TE wave takes place. Note how after the wavefront touches the interface a headwave develops and progressively moves away along the interface. Note also that there is conversion of energy all the time at the interface, but only when the wavefront hits most of the energy of the conversion is radiated up and down. Note also how the polarity of the TE waves oscilates, this is due to the source wavelet used for the seismic wavefield, a Ricker's wavelet composed of a peak between two valleys. It is also important here that the polarity of the downgoing wavefield is opposite to the one of the upgoing wavefield. This happens with conversions among transversal waves, but not with compressional waves.

In Figure 4.14 we show x_1, x_3 snapshots of the VSEP datacube in the P-SV-TM coupling. The picture shows when the conversion from fast-P to TM wave takes place. Contrary to what we saw in the previous case, here the polarity of the generated electromagnetic wavefield is equal above and below the interface, but it is opposite at both sides of the source. Here we also see that most of the energy is converted when the fast-P wavefront touches the interface; later there is only conversion at the headwave that moves away along the interface, but no radiating fields are generated after the initial conversion.

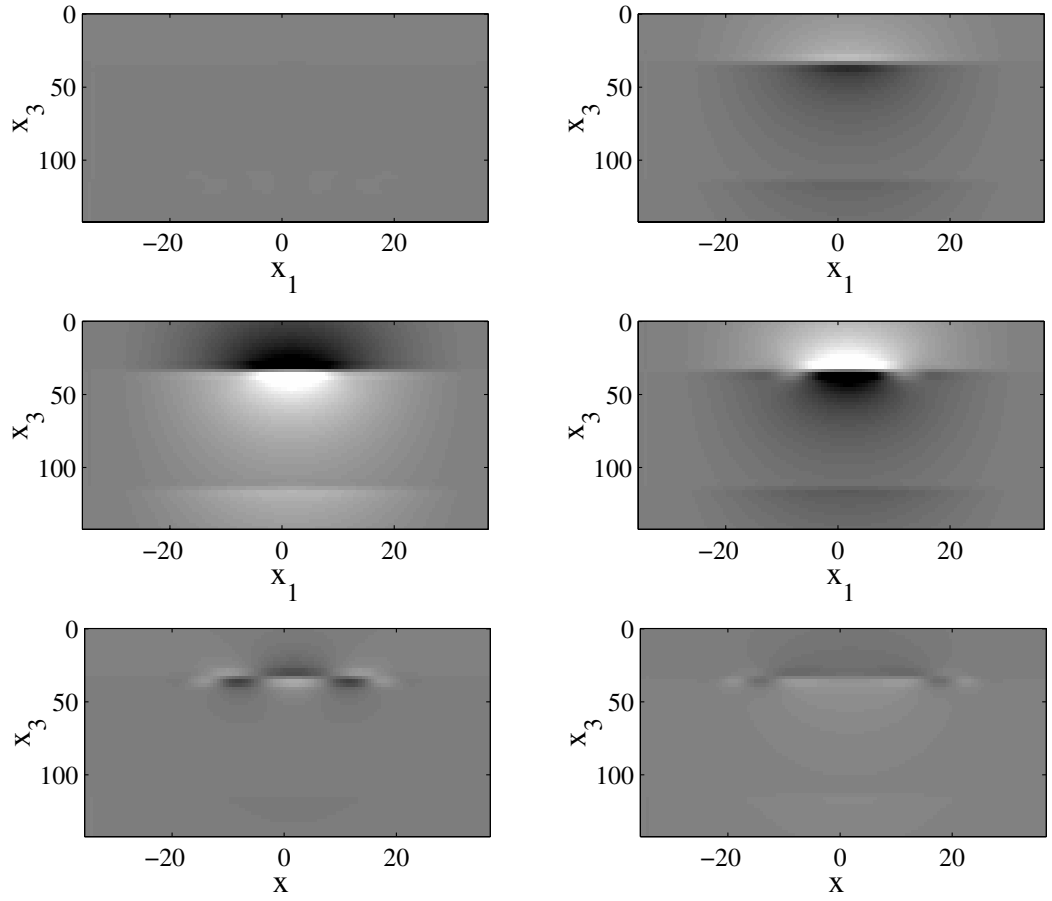

Figure 4.13: *Timeslice simulation for the VSEP in the SH-TE coupling. We see the TE wave generated when the horizontal shear wave encounters the upper interface. The snapshots are taken from 0.009 s to 0.025 s.*

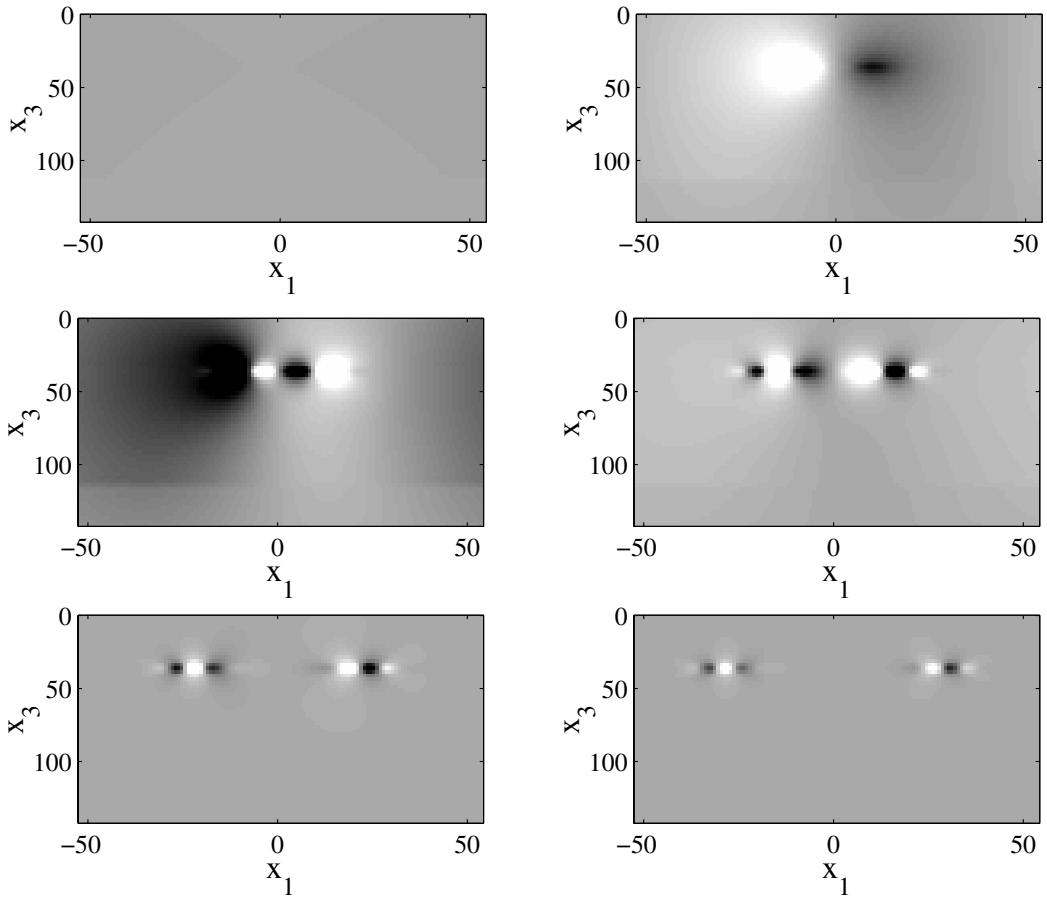

Figure 4.14: *Timeslice simulation for the VSEP in the P-SV-TM coupling. We see the TM wave generated when the fast-P wave encounters the upper interface. The snapshots are taken from 0.006 s to 0.022 s.*

Two-way VSEP simulations in the (t) domain

In this section we include the decomposition at the source and composition at the receiver to the results from the previous subsections. The source composition operators will decompose the two-way wavefields into the one-way wavefields, and the receiver operators will compose them back to two-way wavefields.

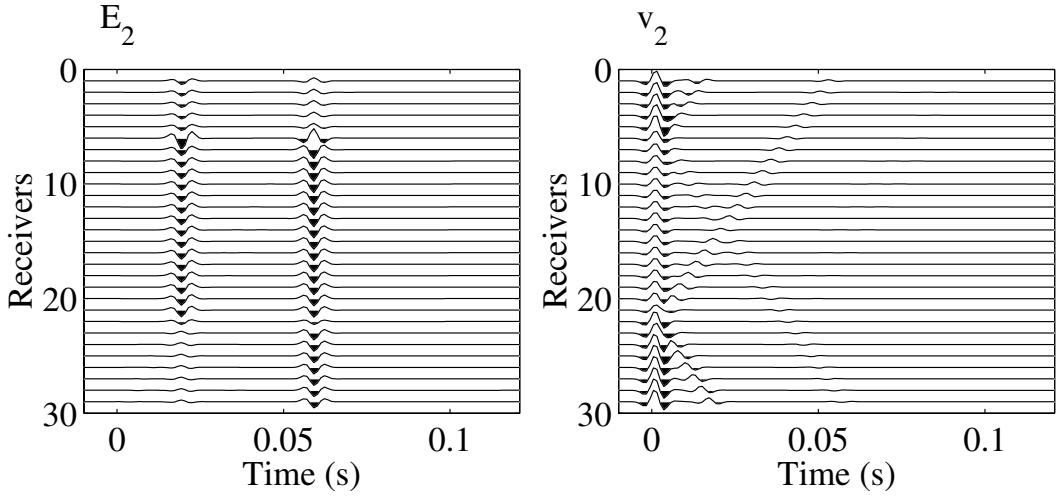

Figure 4.15: *Plane wave response for the two-way VSEP simulation of the SH-TE coupling. Left graph: the sources are external forces in the x_2 direction and the receivers measure E_2. Right graph: the source magnetic source currents in the x_1 direction respectively and the receivers measure v_2.*

In Figure 4.15 we see the two-way VSEP simulation of the SH-TE coupling. In the left graph the receivers measure E_2 and the source are an external force applied to the bulk and fluid phases in the x_2 direction, f_2^b and f_2^f. Note that following the scheme of previous section, in the remaning part of this chapter when using seismic sources the forces applied to blulk and fluid are equal, therefore $f_2^b = f_2^f$. In this graph we see two events at 0.02s and 0.06s that are TE waves reflected from the upper and lower interfaces. Note that the polarity of the generated TE waves changes when crossing an interface in the medium properties. However when these wavefields are generated have the same polarity at both sides of the interface.

In the right graph of Figure 4.15 the receivers measure v_2 and the source are the magnetic source functions in the x_1 direction, J_1^m. We see a straight event at 0s that corresponds to a mechanical disturbance that travels with the

electromagnetic wave and leaves such a trace on the v_2 receiver. Right after this event we see the Sh waves generated at both interfaces just as in figure 4.9. There is also the possibility in this coupling of using a J_3^m source. Both sources give the same result with a difference in polarity of the generated wavefields due to the different orientation in space of the sources J_1^m and J_3^m.

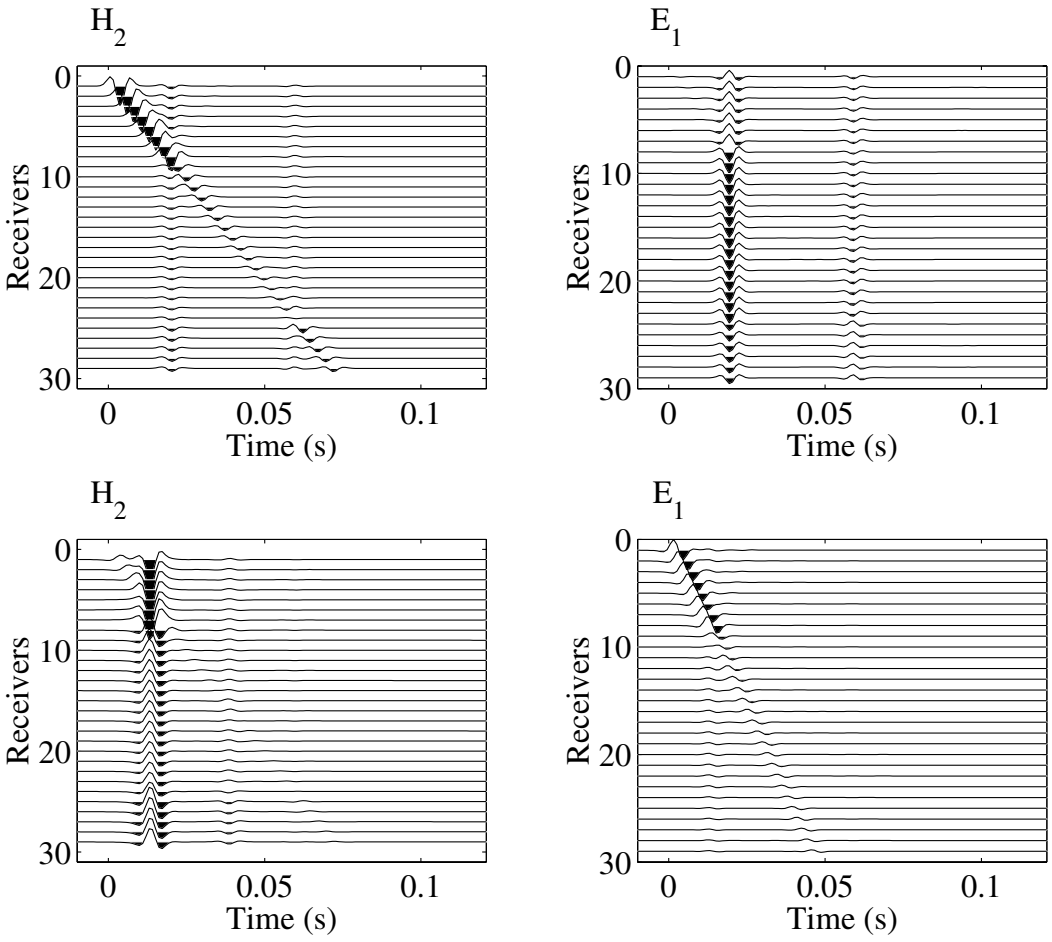

Figure 4.16: *Plane wave response for the two-way VSEP simulation of the P-SV-TM coupling. The source is an external force applied to the bulk and fluid phases, f_1^b and f_1^f on the upper graph, and f_3^b and f_3^f on the lower one. The receivers measure H_2 and E_1.*

In figure 4.16 we see the two-way VSEP simulation of the P-SV-TM coupling. The source is an external force applied to the bulk and fluid phases, f_1^b and f_1^f

in the upper graphs and f_3^b and f_3^f in the lower graphs. The receivers measure H_2 for the two left graphs and E_1 for the two right ones.

In the upper left graph we see the magnetic field contained in the traveling Sv wave. When this wave hits the interfaces two TM waves are generated and are shown in the graph together with the very close conversion from fast-P to TM. In the upper right graph we see clearly the TM reflection from both interfaces when a fast-P waves hits them.

In the lower left graph we see the conversion from an incident vertical shear wave, in this case the conversion from the first interface is much stronger than the one on the second interface. Finally in the lower right graph we just see the electric field travelling with the fast-P wave recorded in the E_1 electrodes.

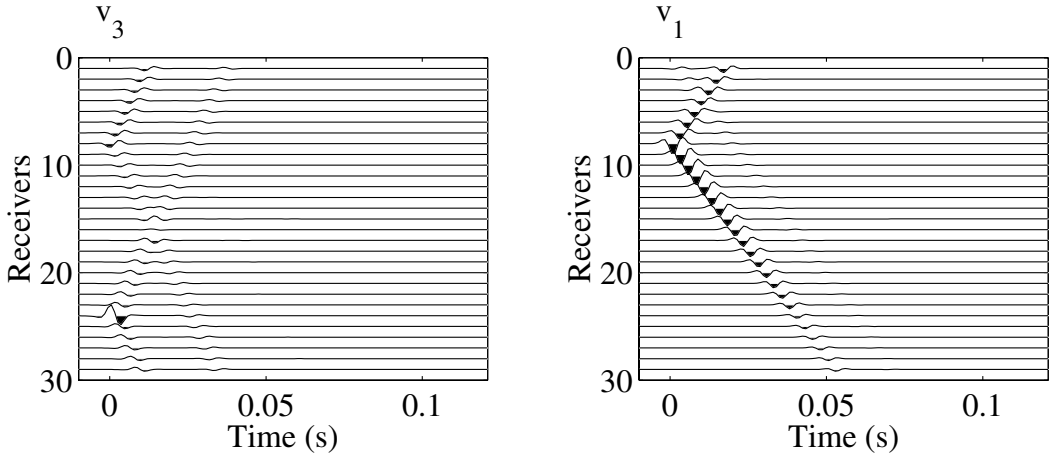

Figure 4.17: *Plane wave response for the two-way VSEP simulation of the P-SV-TM coupling. The source is electric current densities J_1^e. The receivers measure v_3 and v_1.*

In figure 4.17 we see two similar graphs: two-way VSEP simulation of the P-SV-TM coupling. In both graphs the source is electric current densities J_1^e. The receivers measure v_3 in the left graph and v_1 in the right graph. In both graphs we see a clear TM-TM electromagnetic reflection source that carries along a mechanical disturbance that is recorded in the v_3 and v_1 geophones. This arrival almost eclipses further seismo-electric events, except the conversion of these TM waves from the source into vertical shear waves.

Two way VSEP simulations in the (x_1, x_3, t) domain

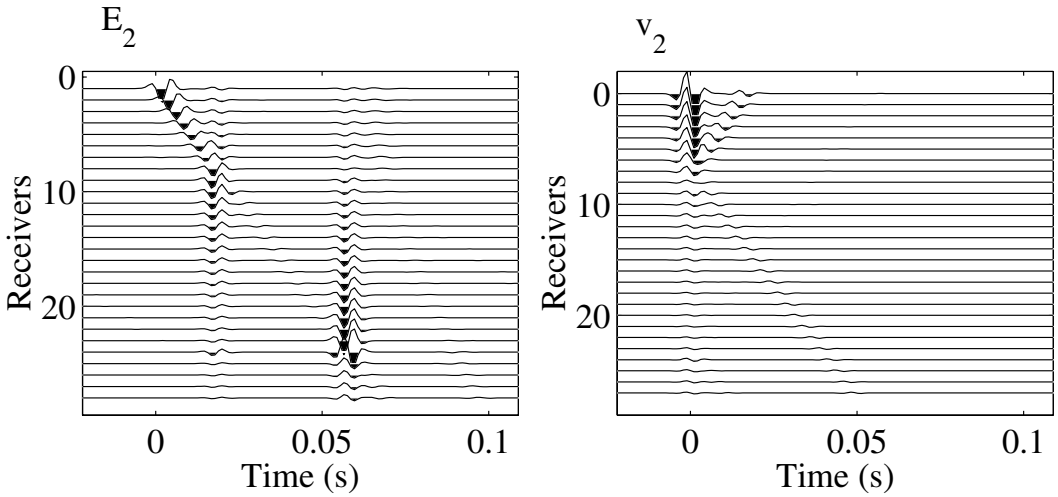

Figure 4.18: *Line source response for the two-way VSEP simulation of the SH-TE coupling. In the left graph the source is an external force in the x_2 direction, $f_2^{\mathrm{b,f}}$. In the right graph the source is a magnetic current in the x_1 direction, J_1^m. The receivers measure E_2 in the left graph and v_2 in the right one.*

In Figures 4.18 to 4.19 we see the x_1, t slices of the two-way VSEP simulation in the (x_1, x_3, t) domain. Figure 4.18 shows two wiggel graphs, in the left graph we see the measurement from a E_2 receiver of a seismic source f_2^{b} and f_2^{f} in the x_2 direction. The first arrival we see is the electric field contained in the horizontal shear wave. As this wave hits the upper interface it generates a TE electromagnetic wave that shows weakly in the graph.

In the right graph of Figure 4.18 we see the seismo-electric response to the electromagnetic source J_1^m. The graph show the seismic disturbance traveling with the TE electromagnetic wave, but we can barely see the conversion from TE to horizontal shear wave at the upper interface. In Figure 4.19 we see the two-way VSEP simulation of the P-SV-TM coupling. In the upper left graph we see the measurement from a H_2 receiver of a seismic source $f_1^{\mathrm{b,f}}$ in the x_1 direction. The only seismoelectric conversion we see here is the magnetic field traveling with the horizontal shear wave, other seismo-electric conversion are not shown due to the difference in amplitude. In the right upper graph we have the measurements of the E_1 receivers of the same source, but in this case the

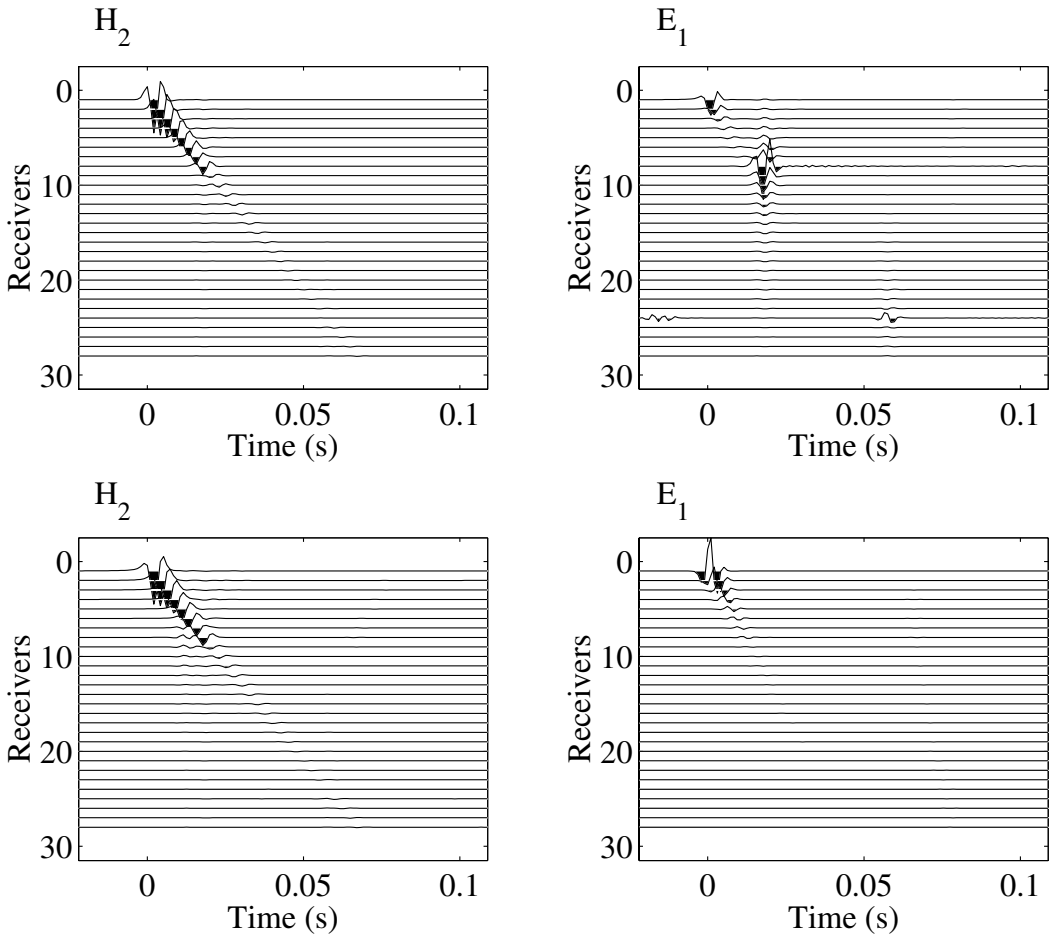

Figure 4.19: *Line source response for the two-way VSEP simulation of the P-SV-TM coupling. The source is an external force in the x_1 and x_3 directions, $f_1^{\mathrm{b}} = f_1^{\mathrm{f}}$ in the two upper graphs and $f^{\mathrm{b}} = f_3^{\mathrm{f}}$ in the two lower graphs. The receivers measure H_2 in the left graphs and E_1 in the right graphs.*

conversion at the interfaces is strong enough to appear. Note that we also see the conversion at the lower interface.

In the lower graphs of Figure 4.19 we see the electric and magnetic fields traveling inside the fast-P wave created at the source.

In Figure 4.20 we see the two-way VSEP simulation of the P-SV-TM coupling in the (x_1, t) domain. The receivers are geophones measuring v_3 and v_1 respectively. The source is and electromagnetic source J_1^{e} in the x_1 direction. The

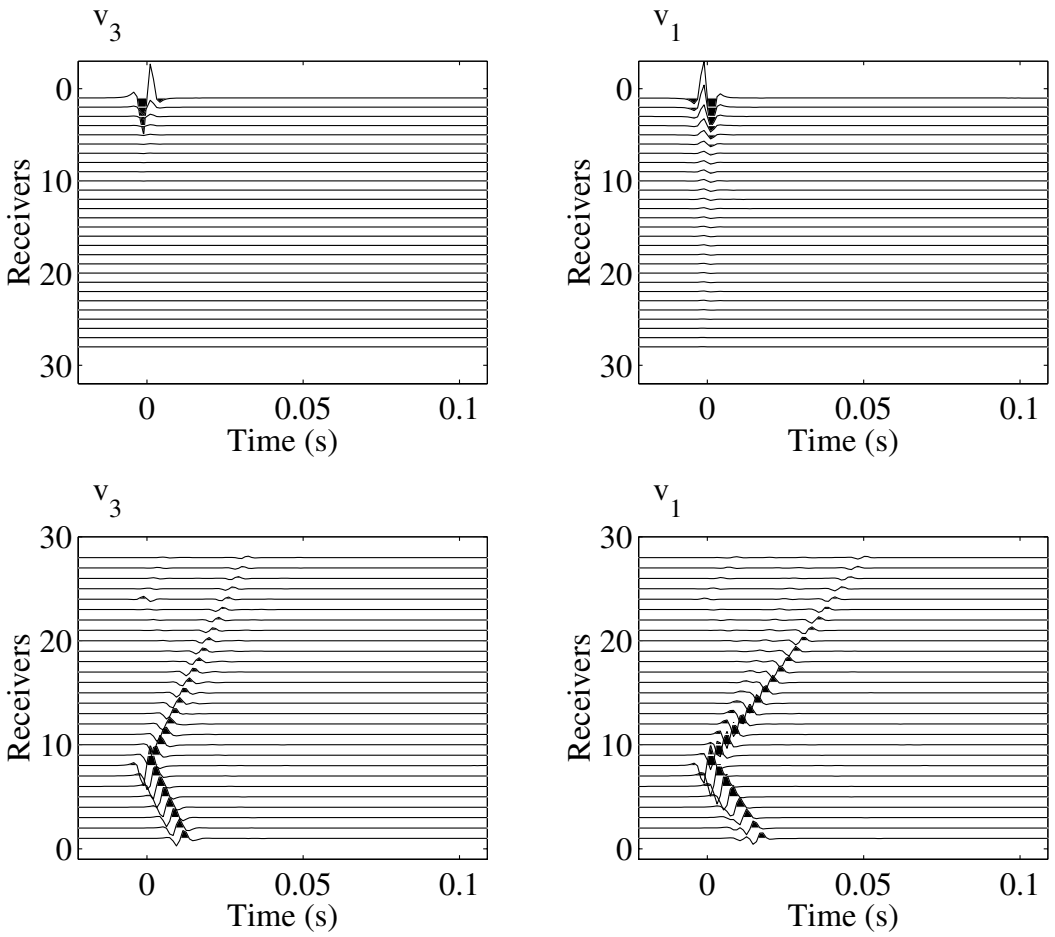

Figure 4.20: *Above: Line source response for the two-way VSEP simulation of the P-SV-TM coupling in the (x_1, t) domain. The source is an electric current in the x_1 directions, J_1^{e}. The geophones measure v_3 in the left graph and v_1 in the right graph. Below: Same case as above with the TM wave arriving to the receivers filtered out to show later arrivals.*

upper graphs show mainly the mechanical disturbance induced from the source's electromagnetic blast, and that is the only feature we see. In the lower graph we have set to zero the elements in the receiver composition operator responsible for processing the TM electromagnetic wavefield. By doing this we remove the seismo-electric conversion at the receivers and we can see the seismo-electric conversion at the interface from the incident TM wave.

Two-way VSEP Timeslices

We have previously seen the one-way timeslices where the evolution of certain one-way wavefields along the x_1x_3 plane was presented. Here we look at the two-way wavefields along the same plane. We have chosen images of the electric, magnetic and particle velocity fields moments before and after the seismo-electric conversion at the upper interface of the medium defined in figure 4.8. In the coming figures we will see the electric field traveling inside seismic waves, as well as the plane seismic wave generated at an interface when an electromagnetic wave is incident.

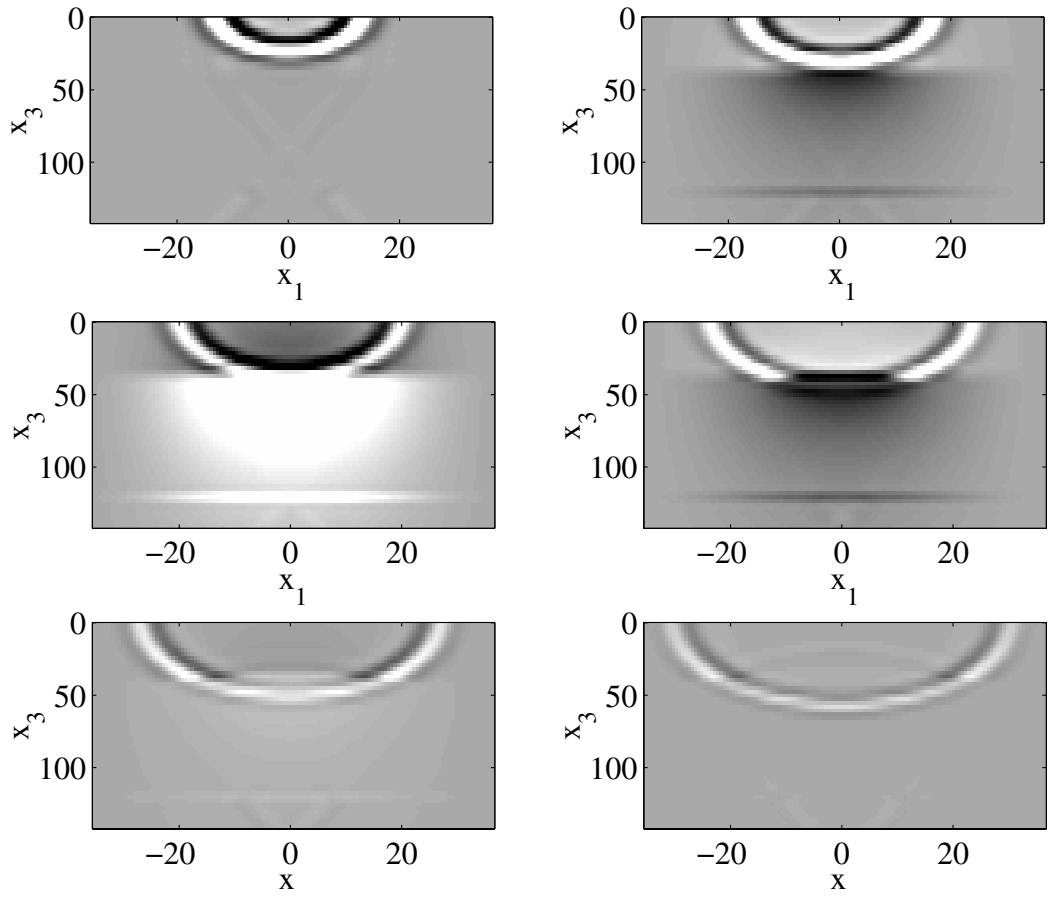

Figure 4.21: x_1, x_3 *timeslice simulation of the SH-TE coupling. Graphs show the propagation of the two-way wavefield* E_2 *with time.*

In Figure 4.21 we show x_1, x_3 snapshots of the datacube when the horizontal shear wave generates a TE wave at the upper interface. What we see here is the E_2 component of the electric field. We find the electric field is carried inside the horizontal shear wave as it propagates downwards, but also as the wave encounters an interface there is a conversion and part of the wavefield's energy is radiated as an electromagnetic diffusive field. Note how the polarity of the converted TE field matches with the polarity of the part of the wavefront crossing at that moment the interface, and how the TE wave radiated upwards has opposite polarity than the one radiated downwards.

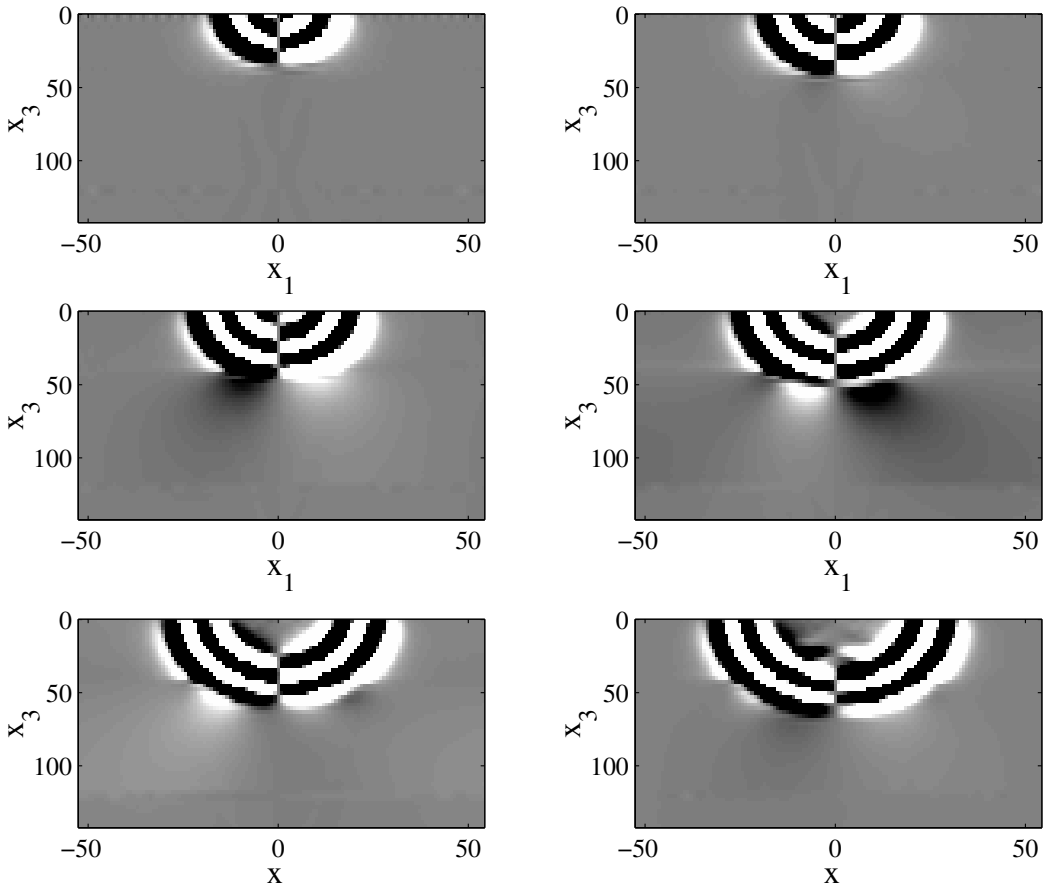

Figure 4.22: *Timeslice simulation of the P-SV-TM coupling. Graphs show the propagation of the two-way wavefield E_1 from a f_3 source with time.*

In Figure 4.22 we show x_1, x_3 snapshots of the datacube when the conversion from fast-P to TM wave takes place at the upper inerface. In this figure we see the E_1 component of the electric field traveling inside a fast-P wave. When the seismic wavefield hits the interface there is a conversion and a TM electromagnetic wave is generated. Note that also in this case the polarity of the generated electromagnetic field has the same polarity as the lobe of the seismic wavefront that generated it. Note also that the polarity of the electric field traveling inside the fast-P wave has opposite polarities at both sides of the source in the x_1 direction. The special color that the electric field inside the fast-P wave has in these graphs is due to the difference in amplitude of the two conversions, the grey scale of the much stronger E field inside the fast-P wave has been saturated to black and white to allow the weaker TM wave to be seen.

In Figure 4.23 we show x_1, x_3 snapshots of the datacube when the conversion from fast-P and vertical shear to TM wave takes place at the upper inerface. This figure shows the H_2 component of the magnetic field from a f_3 source. Similarly to the previous figure, here we see the magnetic field generated at a seismoelectric conversion as well as traveling inside the vertical shear wave. Although it doesn't show here, there is a fast-P wave ahead of this vertical shear wave. When the fast-P wave hits the interface there is a conversion and a TM electromagnetic wave is generated before the shear wave reaches the interface. Naturally, there is also a conversion from the vertical shear wave as we have already seen in the one-way timeslices. In the last two graphs of this serie we also find the head wave generated by the fast-P wave due to the H_2 component of the magnetic field in them.

In Figure 4.24 we show x_1, x_3 snapshots of the datacube when the conversion from TM to fast-P wave takes place at the upper inerface. In this figure we see the v_3 component of the particle velocity across the x_1, x_3 plane when the source is J_1^e. Note how in the first snapshot we can see the electromagnetic source disturbing the mechanical field for the time the source wavelet lasts, and note also the odd polarity of the source and the generated seismic waves along the offset x_1. At time zero there is a generation at the interface of up and downgoing compressional plane waves.

In Figure 4.25 we show x_1, x_3 snapshots of the conversion from TM to shear wave taking place at the upper inerface. In this figure we see the v_1 component of the particle velocity across the x_1, x_3 plane when the source is J_2^m. Note the similarities with previous figure, and how in this case the wavefields have an even polarity along the offset x_1. Note also that at time zero, as soon as the source is triggered, there is a generation of a plane shear wave at the upper

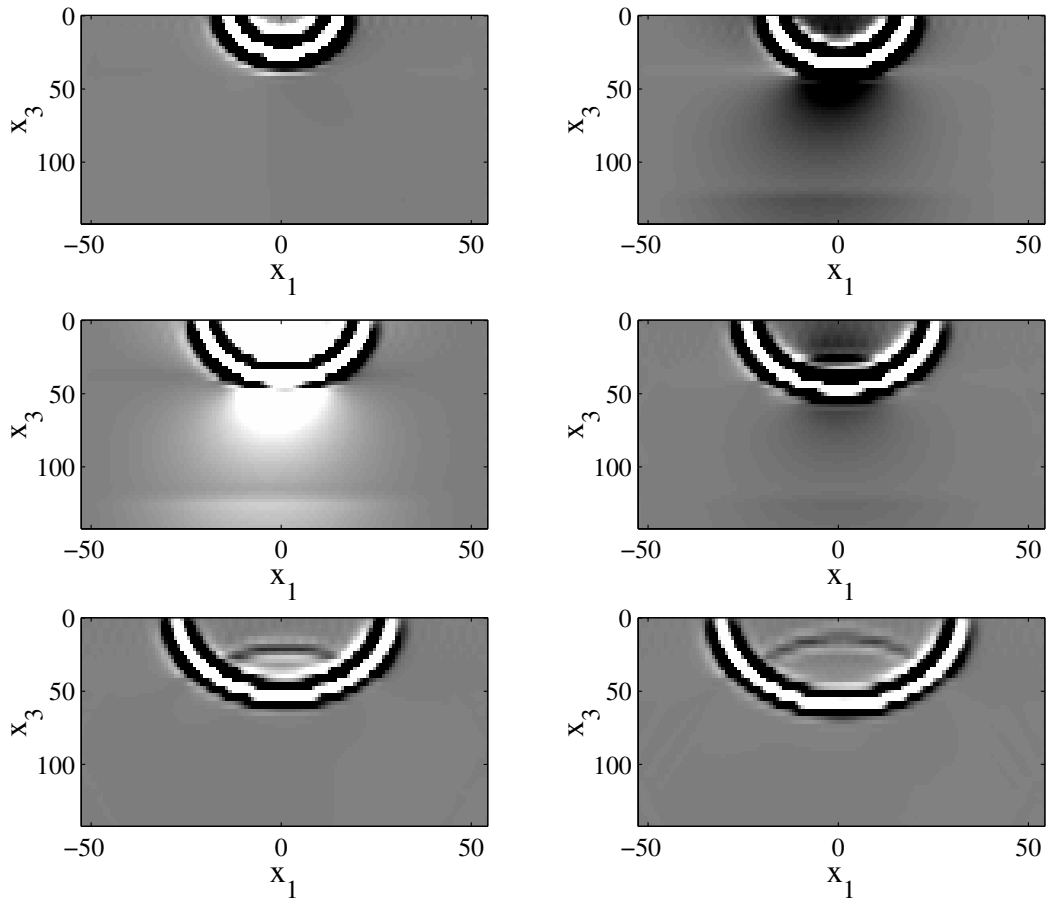

Figure 4.23: *Timeslice simulation of the P-SV-TM coupling. Graphs show the propagation of the two-way wavefield H_2 from a f_1 source with time.*

interface. In theory, since the J_2^m reaches both interfaces at the same time there is also a generation of shear waves at the lower interface, but it is of much lower amplitude and it does not show on the graph.

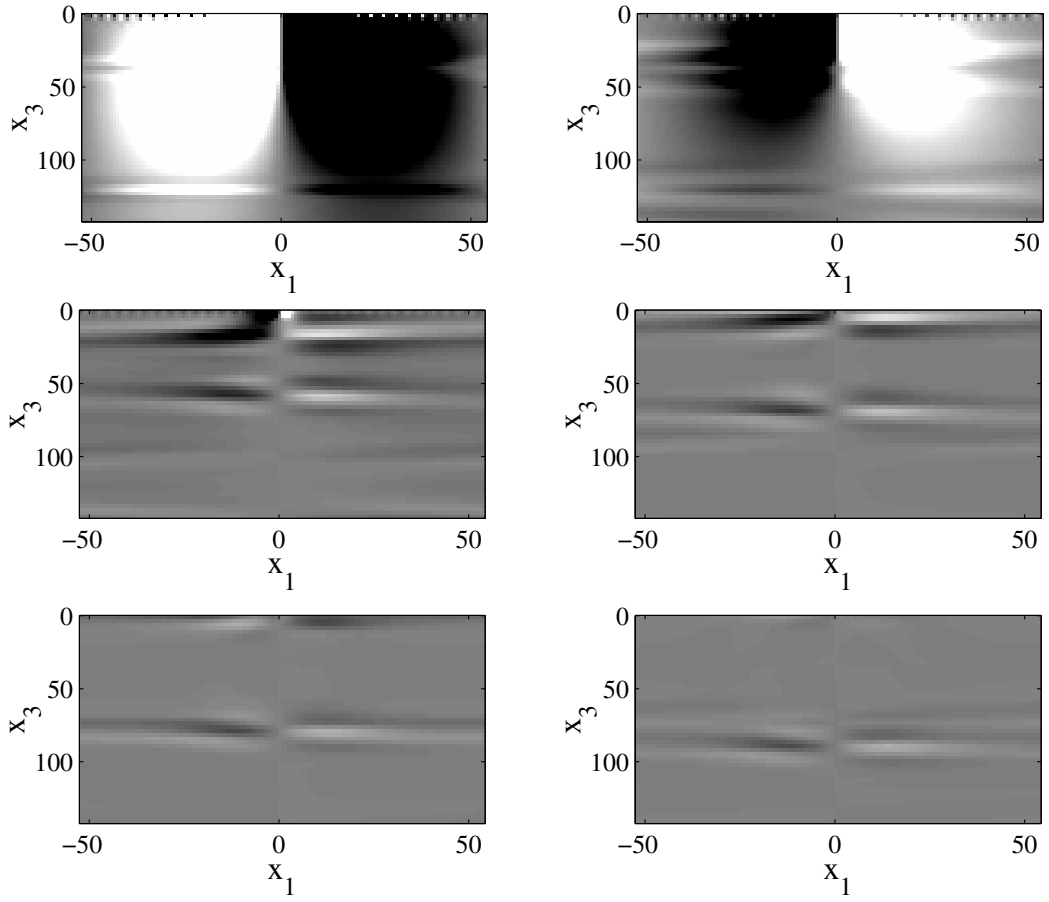

Figure 4.24: *Timeslice simulation of the P-SV-TM coupling. Graphs show the propagation of the two-way wavefield v_3 from a J_1^e source with time.*

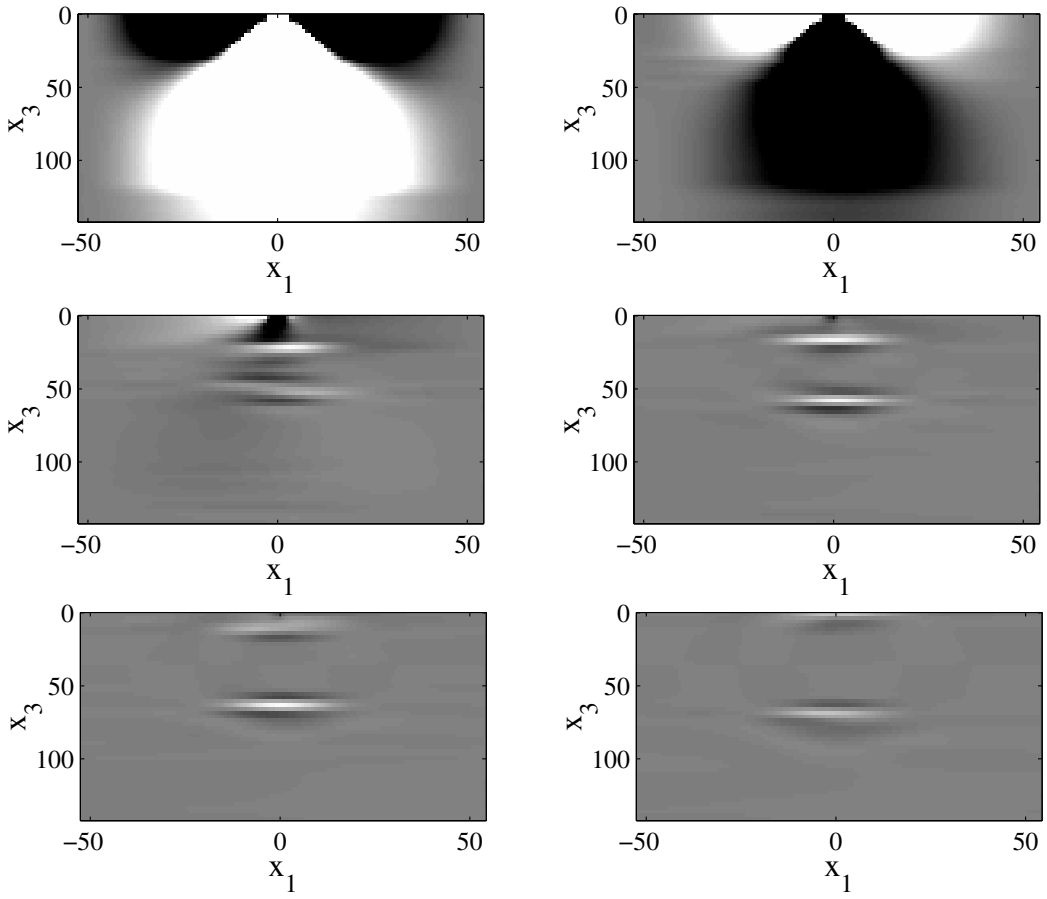

Figure 4.25: *Timeslice simulation of the P-SV-TM coupling. Graphs show the propagation of the two-way wavefield v_1 from a J_2^m source with time.*

4.4 Wellbore to wellbore seismo-electric survey

In this section we describe a seismo-electric wellbore to wellbore model. In this type of survey receivers are placed along a wellbore and the source is in a different nearby wellbore at a certain depth. This allows us to study the properties of layers that are too deep to be studied with sources at the earth's surface.

In the previous sections we have derived all the operators and coefficients for the VSEP survey. In this section we base our wellbore to wellbore model on the previously derived VSEP model.

4.4.1 One way wellbore to wellbore seismo-electric survey

The model we present for the wellbore to wellbore survey is composed by two VSEP problems interconnected in an iterative expression. We separate the medium in which we need to model the wellbore to wellbore survey into two auxiliary media as in figure 4.26. In medium U we have all the layers that originally were above the source level plus a homogeneous porous halfspace below the source level z_s whose medium properties are those of the layer right below the interface. In medium L we have all the layers that originally were below z_s plus a homogeneous porous halfspace above it whose medium properties are those of the layer right above the interface.

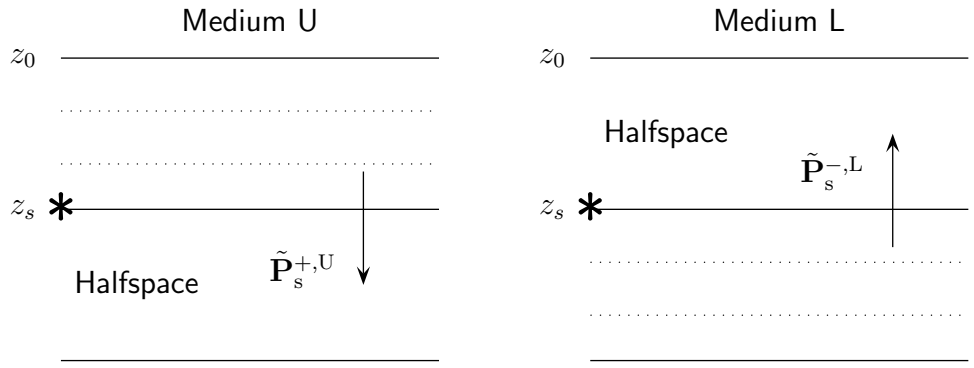

Figure 4.26: *wellbore to wellbore auxiliary mediums U and L.*

On each step of the iteration we feed each medium's outgoing wavefields into the opposite medium. This way we ensure the continuity of all wavefields

across the source level. The iterated VSEP simulation on medium U will model the upper half of the wellbore to wellbore simulation while the iterated VSEP simulation on medium L will model the lower half of it. Finally both wavefields are summed to yield the full wellbore to wellbore model.

Applying the equations for the VSEP problem (4.20-4.22) to these two media provide us with all the up and downgoing wavefields at all the layers. From those we can extract the up and downgoing wavefields that propagate across z_s. These two wavefields are important because they serve as "source wavefields" for the opposite medium on the next iteration. After running the algorithm once we obtain $\tilde{\mathbf{P}}_{\mathrm{s}}^{+,\mathrm{U}}$ that will be propagated into medium L and $\tilde{\mathbf{P}}_{\mathrm{s}}^{-,\mathrm{L}}$ that will be propagated in medium U.

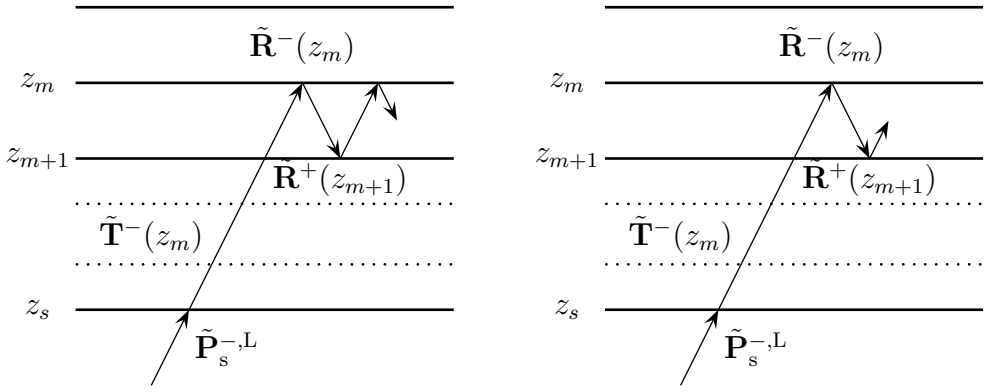

Figure 4.27: *Left and right we see a scheme of the up and downgoing wavefields respectively at the medium U.*

All this is done inside the first iteration loop. The first time we run this algorithm we use equations (4.21-4.22) as they are defined in the previous section. From those wavefields we extract $\tilde{\mathbf{P}}^{+,U}(z_s)$ and $\tilde{\mathbf{P}}^{-,L}(z_s)$ and we use them into the second step as the starting wavefields according to

$$\tilde{\mathbf{P}}_2^{+,\mathrm{U}}(z_m) = \left(\tilde{\mathbf{I}} - \tilde{\mathbf{R}}^{+}(z_{m+1})\tilde{\mathbf{R}}^{-}(z_m)\right)^{-1} \tilde{\mathbf{T}}^{-}(z_m)\tilde{\mathbf{P}}_1^{-,\mathrm{L}}(z_s) \tag{4.24}$$

$$\tilde{\mathbf{P}}_2^{-,\mathrm{U}}(z_m) = \left(\tilde{\mathbf{I}} - \tilde{\mathbf{R}}^{-}(z_m)\tilde{\mathbf{R}}^{+}(z_{m+1})\right)^{-1} \tilde{\mathbf{R}}^{-}(z_m)\tilde{\mathbf{T}}^{-}(z_m)\tilde{\mathbf{P}}_1^{-,\mathrm{L}}(z_s) \tag{4.25}$$

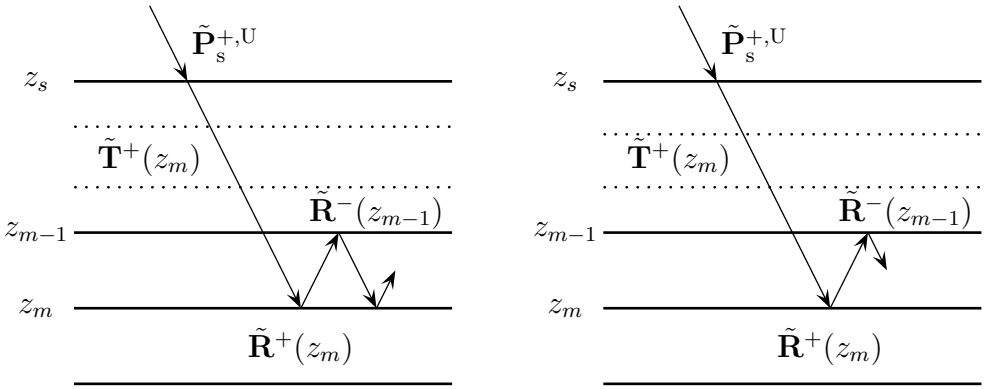

Figure 4.28: *Left and right we see a scheme of the up and downgoing wavefields, respectively in medium L*

and

$$\tilde{\mathbf{P}}_2^{+,\mathrm{L}}(z_m) = \left(\tilde{\mathbf{I}} - \tilde{\mathbf{R}}^{-}(z_{m-1})\tilde{\mathbf{R}}^{+}(z_m)\right)^{-1} \tilde{\mathbf{T}}^{+}(z_m)\tilde{\mathbf{P}}_1^{+,\mathrm{U}}(z_s) \tag{4.26}$$

$$\tilde{\mathbf{P}}_2^{-,\mathrm{L}}(z_m) = \left(\tilde{\mathbf{I}} - \tilde{\mathbf{R}}^{+}(z_m)\tilde{\mathbf{R}}^{-}(z_{m-1})\right)^{-1} \tilde{\mathbf{R}}^{+}(z_m)\tilde{\mathbf{T}}^{+}(z_m)\tilde{\mathbf{P}}_1^{+,\mathrm{U}}(z_s) \tag{4.27}$$

where the subscripts $_1$ and $_2$ are the iteration indexes and the superscripts $^{\mathrm{U}}$ or $^{\mathrm{L}}$ denote the auxiliary field in which the wavefields are propagating.. Using equation (4.20) we have for the second iteration

$$\tilde{\mathbf{P}}_2^{\mathrm{U}}(z_m) = \left(\tilde{\mathbf{P}}_1^{+,\mathrm{U}}(z_m) + \tilde{\mathbf{P}}_1^{-,\mathrm{U}}(z_m)\right) \tilde{\mathbf{P}}_1^{-,\mathrm{L}}(z_s) \tag{4.28}$$

$$\tilde{\mathbf{P}}_2^{\mathrm{L}}(z_m) = \left(\tilde{\mathbf{P}}_1^{+,L}(z_m) + \tilde{\mathbf{P}}_1^{-,\mathrm{L}}(z_m)\right) \tilde{\mathbf{P}}_1^{+,\mathrm{U}}(z_s). \tag{4.29}$$

We can write this in a more compact form

$$\tilde{\mathbf{P}}_l^{\mathrm{U}}(z_m) = \tilde{\mathbf{P}}_1^{\mathrm{U}}(z_m) \sum_{i=1}^{l} \tilde{\mathbf{P}}_{\mathrm{i-1}}^{-,\mathrm{L}}(z_s) \tag{4.30}$$

$$\tilde{\mathbf{P}}_l^{\mathrm{L}}(z_m) = \tilde{\mathbf{P}}_1^{\mathrm{L}}(z_m) \sum_{i=1}^{l} \tilde{\mathbf{P}}_{\mathrm{i-1}}^{+,\mathrm{U}}(z_s) \tag{4.31}$$

and finally we sum all the wavefields as

$$\tilde{\mathbf{P}}_{\mathrm{l}}(z_m) = \tilde{\mathbf{P}}_{\mathrm{l}}^{\mathrm{U}}(z_m) + \tilde{\mathbf{P}}_{\mathrm{l}}^{\mathrm{L}}(z_m) \tag{4.32}$$

4.4.2 Two-way wellbore to wellbore seismo-electric survey

In this section we introduce into our wellbore to wellbore simulation the effects of the source and receivers. To do that we use the composition and decomposition operators defined in sections 3.5 and 3.6.

In this case we use the source decomposition operator for the up and downgoing wavefields, since we assume the source is placed in the middle of the wellbore. We also use the receiver composition operator for up and downgoing wavefields arriving to the receivers since the receivers are place along the wellbore.

$$\tilde{\mathbf{Q}}_{\mathrm{l}}^{\mathrm{U}}(z_m) = \tilde{\mathbf{C}}_{\mathrm{r}}^{\mathrm{U}}(z_m)\tilde{\mathbf{P}}_{\mathrm{l}}^{\mathrm{U}}(z_m)\tilde{\mathbf{S}}^{-,\mathrm{U}}(z_m) \tag{4.33}$$

$$\tilde{\mathbf{Q}}_{\mathrm{l}}^{,\mathrm{L}}(z_m) = \tilde{\mathbf{C}}_{\mathrm{r}}^{\mathrm{L}}(z_m)\tilde{\mathbf{P}}_{\mathrm{l}}^{\mathrm{L}}(z_m)\tilde{\mathbf{S}}^{+,\mathrm{L}}(z_m) \tag{4.34}$$

where $\tilde{\mathbf{C}}_{\mathrm{r}}^{\mathrm{U}}(z_m)$ are the receiver composition operators and $\tilde{\mathbf{C}}_{\mathrm{s}}^{+,\mathrm{L}}(z_m)$ and $\tilde{\mathbf{C}}_{\mathrm{s}}^{-,\mathrm{U}}(z_m)$ are the source decomposition operators. We have to apply the composition and decomposition operators to the up and downgoing waves separately, since both will be different for up or downgoing waves. After applying the composition and decomposition to the wavefields, we substitute $\tilde{\mathbf{P}}_{\mathrm{l}}^{\mathrm{U}}(z_m)$ and $\tilde{\mathbf{P}}_{\mathrm{l}}^{,\mathrm{L}}(z_m)$ into (4.32) to obtain the full two-way wavefield.

4.4.3 Results

In this section we show the results of our wellbore to wellbore simulations. First we show the plane wave one-way wavefields, i.e. the interaction among diferent pairs of wavefields along the wellbore. In the next section we include the two-way to one-way decomposition at the source and the one-way to two-way composition at the receiver. We apply all the wellbore to wellbore propagation models to the same medium configuration as the VSEP.

Note that due to the fact that we can consider VSEP as a particular case of wellbore to wellbore survey in which the source is at the top of the well, many of the figures shown on this section do resemble those shown in section 4.3.3.

One-way wellbore to wellbore simulations in the (x_3, t) domain

Here we show the results of the one-way wellbore to wellbore simulations in the (t) domain. Although this is not properly a wellbore to wellbore simulation (source and receivers are in the same well), we call it this way because it serves as a first step for later, proper wellbore to wellbore simulations. The model is

applied to the same medium as the vertical seismo-electric profile, the data of this setup can be found in Figure 4.8 and Table 4.1.

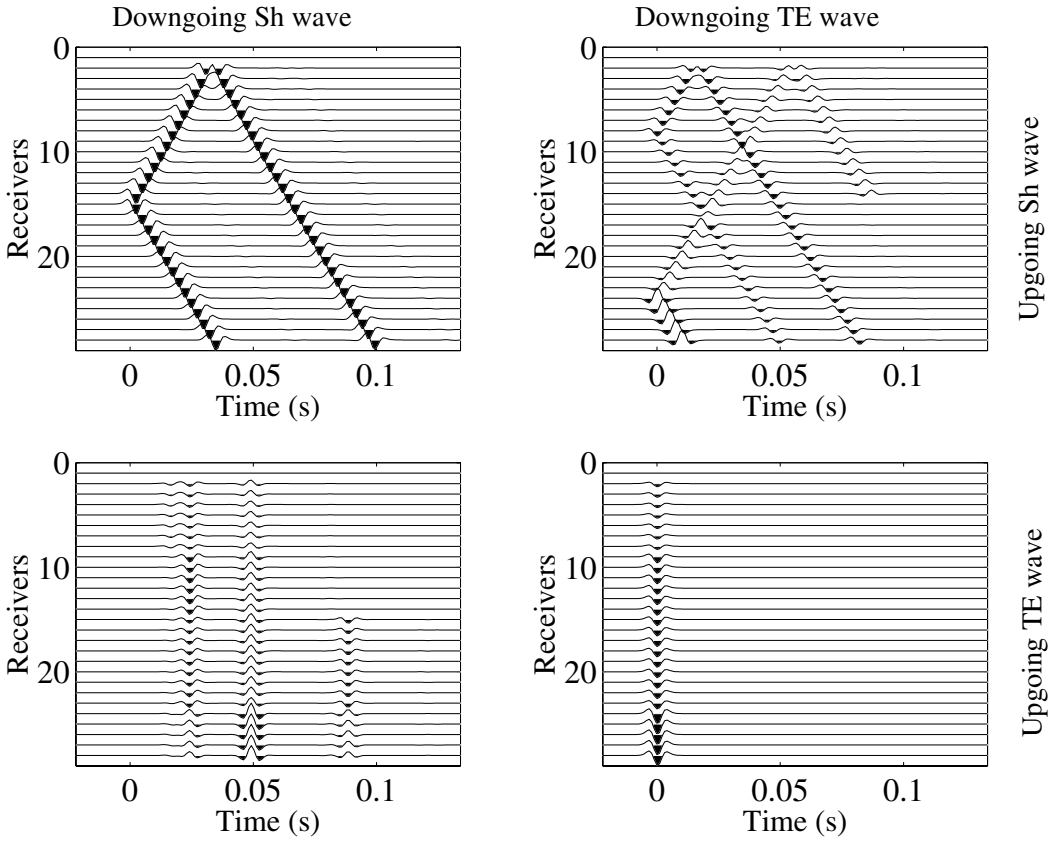

Figure 4.29: *Plane wave response for the one-way wellbore to wellbore simlation of the SH-TE coupling*

In figure 4.29 we see the one-way wellbore to wellbore simulation of the SH-TE coupling. Similarly to the results of the VSEP simulation the graphs are organized in a matrix. In the left column we see the up and downgoing wavefields generated as a horizontal shear wave hits both interfaces from the source point which is at receiver 15. In the lower left graph we see four conversions, two from the horizontal shear wave from the source, and two more from the horizontal shear wave reflected from the surface and propagated back to the interfaces. We can also see how the upgoing wavefields are reflected back from the surface, in this model we have added the reflection from the source using the reflection

coefficients derived in Section 3.3.2.

At the right column of graphs we see the two wavefields generated as a downgoing TE hits both interfaces, horizontal shear and TE electromagnetic respectively. In the upper graph it can be seen clearly how horizontal shear waves are generated at the same time on both interfaces and are reflected at the surface. Finally in the lower graph we have the TE wave reflected from the incident TE wave.

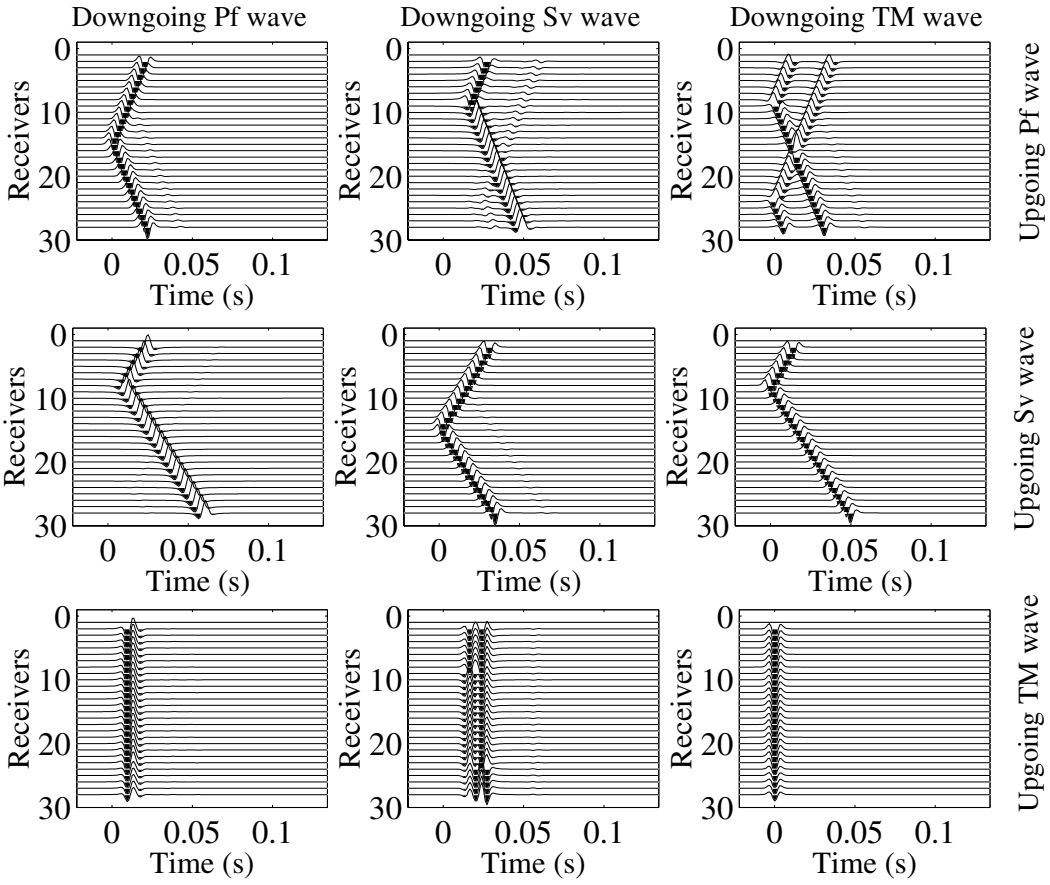

Figure 4.30: *Plane wave response for the one-way wellbore to wellbore simlation of the P-SV-TM coupling*

In figure 4.30 we see the one-way wellbore to wellbore simulation of the P-SV-TM coupling. These graphs are organized similarly to figure 4.10. In the left column of graphs we see the three wavefields generated as an up and downgoing

fast-P wave hits the interfaces, fast-P, vertical shear and TM electromagnetic waves respectively are generated. It is specially interesting to see how the conversion between seismic waves takes place only at the upper interface, while the seismo-electric conversion occurs at both interfaces. Although in the lower graph we see only one conversion from fast-P to TM wave, there is a second one that doesn't show because the interface is of a different type and the amplitude of the reflection is much weaker.

In the three graphs of the middle column we see the wavefields generated as an up and downgoing vertical shear wave hits the interfaces, fast-P, vertical shear and TM electromagnetic waves respectively. Note the similarities with the wavefields generated by the fast-P wave. Note also how the conversions at both interfaces from vertical shear to TM have similar amplitudes, unlike when the incident wave is a fast-P wave.

In the rigth column of graphs we see the three wavefields generated as an up and downgoing vertical TM wave hits the interfaces. It is important to see here how the incident TM wave generates at both interfaces fast-P waves of comparable amplitude, but not vertical shear waves.

One-way wellbore to wellbore simulations in the (x_1, x_3, t) domain

In this section we present the results of the wellbore to wellbore simulation in which we have included the dependency on the offset as well as the effects from the source and receivers. As in previous cases of two-way simulations we have seen how the composition and decomposition operators combine the already known one-way wavefields into the two-way wavefields that are actually measurable by the receivers.

We see in Figures 4.31 and 4.32 the seismo-electric conversion at a wellbore. In Figure 4.31 we find the conversion at interfaces from a seismic source along a wellbore. We saw at Chapter 3 that for a seismic incident wave only angles close to normal incidence will generate an homogeneous seismo-electric conversion, therefore in this case only points at the interface very close to the wellbore will generate electromagnetic waves that will be radiated to all the receivers in the opposite well. As the seismic wave continues propagating it will generate a headwave at any interface that will propagate forward in the x_1 direction. This headwave does not radiate but it contains an electric field that will be picked up by the receivers place along the opposite well.

In Figure 4.32 we find the conversion at interfaces from an electromagnetic source along a wellbore. We saw at Chapter 3 that for this case any angle of

incidence will generate a normally reflected seismic wave, so in this case plane up and downgoing waves will be detected by the geophones placed along the left wellbore.

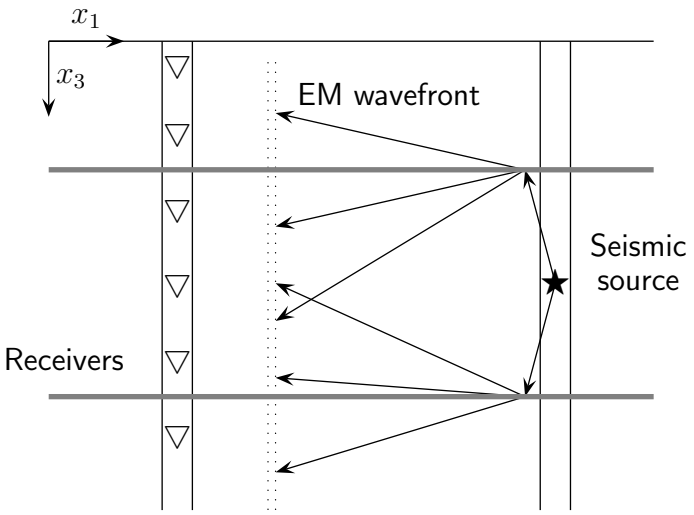

Figure 4.31: *Seismic to electromagnetic conversion in a wellbore to wellbore simulation. We assume that both wells are drilled in the same medium.*

In figure 4.33 we see a one-way wellbore to wellbore simulation of the SH-TE coupling, with the media parameters described in Table 4.1 and for a wellbore separation of 30m. In the left graphs: the incident wavefield is seismic and the reflected wavefields are seismic above and electromagnetic below. In the right graphs: the incident wavefield is electromagnetic and the reflected wavefields are seismic above and electromagnetic below.

If we compare these results with those in the (x_3, t) domain from Figure 4.29 we find several differences, on the first place there is a geometrical spreading in this case that logically is not present in the (x_3, t) domain. Besides, the current case has the source in a different wellbore 30 m apart. This makes the times of the first seismic arrival to be delayed proportionally to the wellbore separation, and the shape of the seismic arrival turns into a hyperbola. Since we assume that both wells are in the same set of media, this delay does not affect to the seismoelectric arrivals, regardless the separation between wellbores since it only depends on the vertical distance between the source and the interface.

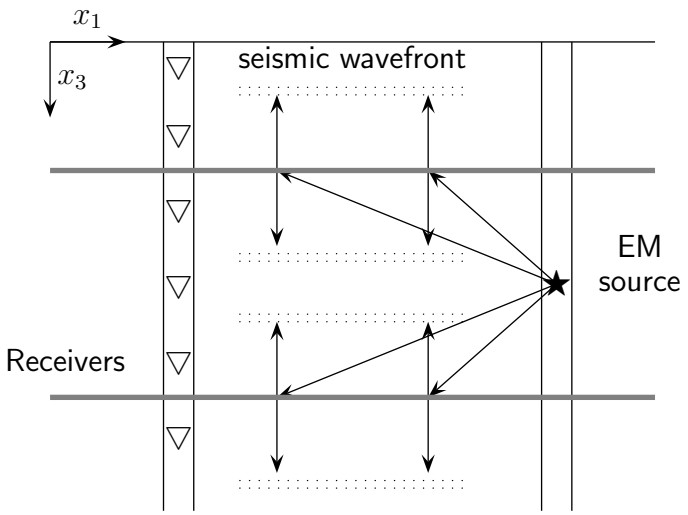

Figure 4.32: *Electromagnetic to seismic conversion in a wellbore to wellbore simulation. We assume that both wells are drilled in the same medium.*

Bear in mind that our model only considers discontinuities along x_3, but in a realistic medium, if there was a discontinuity along x_1 there would be a seismo-electric conversion at that interface that would naturally affect the arrival time of the converted wavefields.

In figure 4.36 we see the results of the one-way wellbore to wellbore simulation of the P-SV-TM coupling, with the media parameters described in Table 4.1 and for a wellbore separation of 30m. In the left graphs the incident wavefield is a fast-P wave and the reflected wavefields are from top to bottom fast-P, vertical shear and TM electromagnetic waves. In the middle and right columns of graphs the incident wavefields are a vertical shear and a TM electromagnetic wave respectively. The reflected wavefields are arranged as in the left column of graphs. If we compare this figure with Figure 4.30 we find again the same similarities as in the SH-TE case.

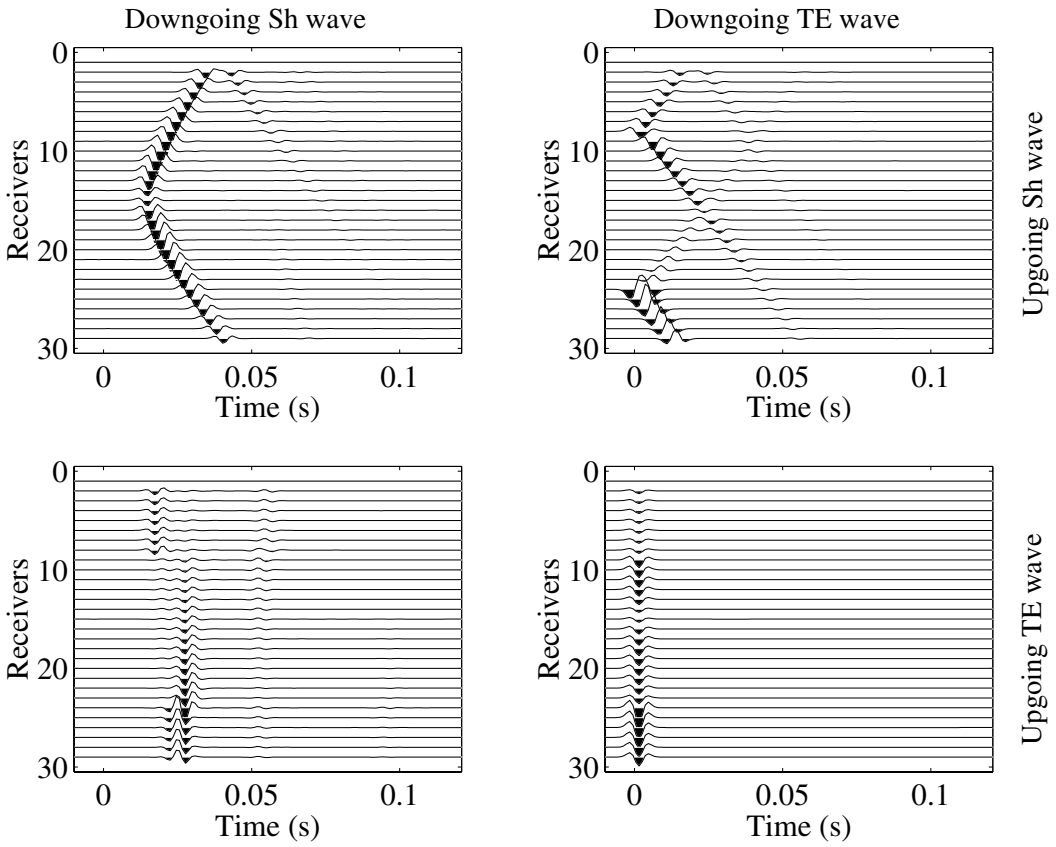

Figure 4.33: *Line source response for the one-way wellbore to wellbore simulation of the SH-TE coupling in the (x_1,x_3,t) domain. The wellbore separation is 30 m and the media parameters are those of Table 4.1.*

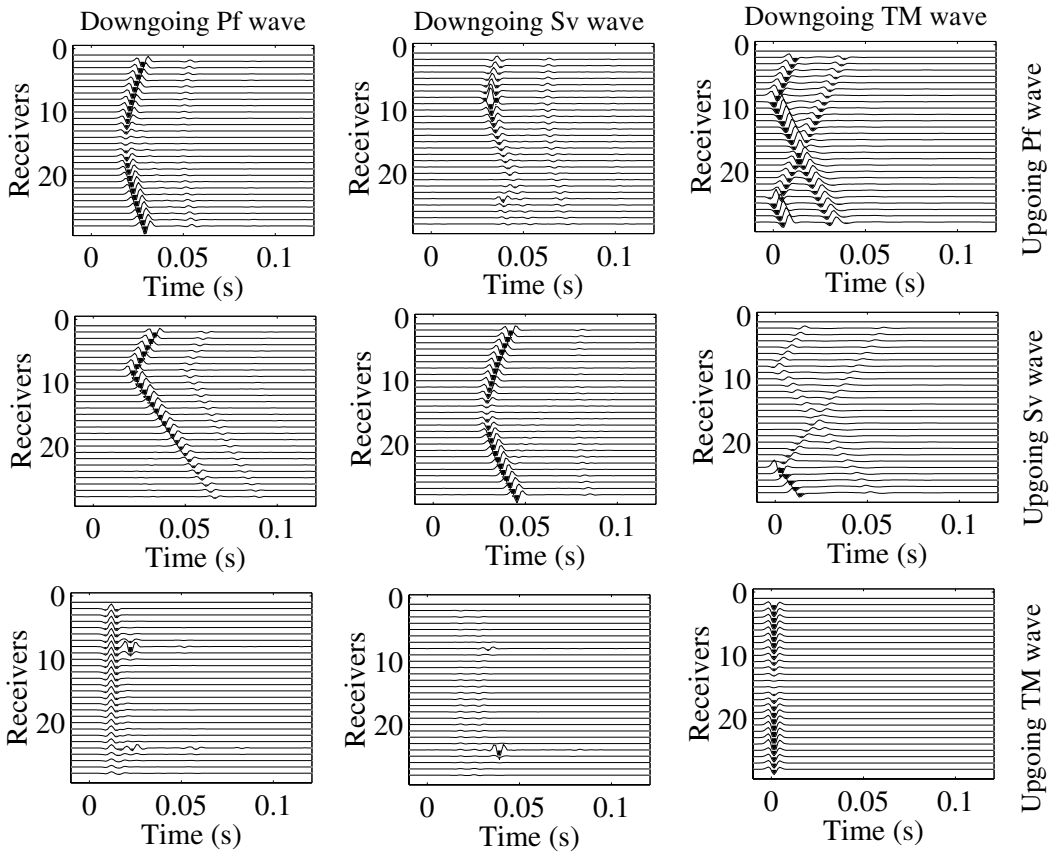

Figure 4.34: *Line source response for the one-way wellbore to wellbore simulation of the P-SV-TM coupling in the (x_1,x_2,t) domain. The wellbore separation is 30 m and the media parameters are those of Table 4.1.*

Two-way wellbore to wellbore simulations in the (x_1, x_3, t) domain

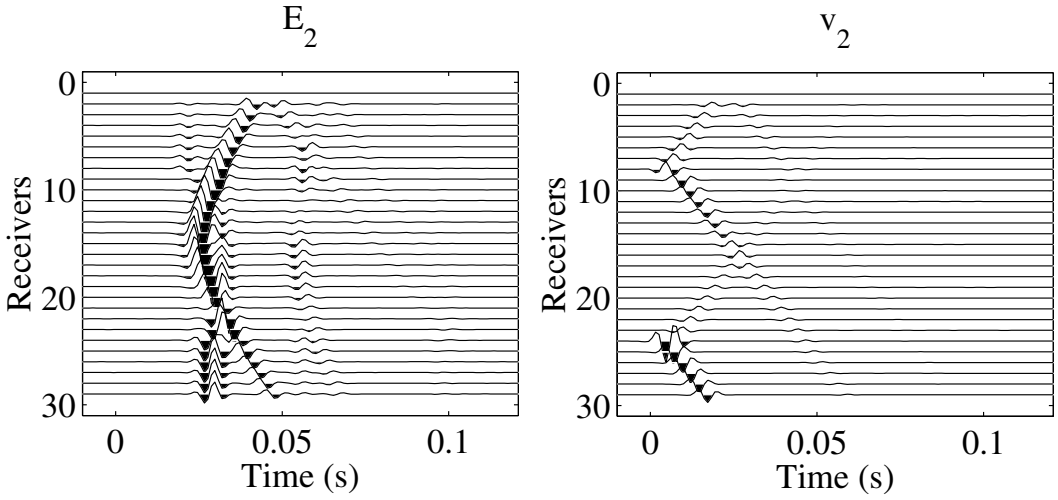

Figure 4.35: *Line source response for the two-way wellbore to wellbore simulation of the SH-TE coupling in the (x_1,x_2,t) domain. The wellbore separation is 30 m and the media parameters are those of Table 4.1. Left graph: the receivers measure E_2 and the source is a bulk and fluid force in the x_2 direction, f_2^b and f_2^f. Right graph: the receivers measure v_2 and the source is an electric current in the x_2 direction, J_2^e.*

In Figure 4.35 we see the two-way wellbore to wellbore simulation of the SH-TE coupling in the (x_1,x_3,t) domain. The wellbore separation is 30 m and the media parameters are those of Table 4.1. In the left graph the receivers measure E_2 and the source is a bulk and fluid force in the x_2 direction, f_2. In the right graph the receivers measure v_2 and the source is a electric source current in the x_2 direction, J_2^e. We can see on the left graph the electric field contained in the horizontal shear wave as an hyperbola. The arrival time of this wavefield to the receiver at the source level is the wellbore separation divided by the shear wave velocity. As this horizontal shear wave crosses both interfaces there are seismo-electric conversions that generate TE waves that are recorded in the E_2 receivers as the one at the lower interface that arrives at 0.02s.

On the right graph of Figure 4.35 we show the measurements of the v_2 receivers. Here we see first the seismic disturbance that is propagated with the electromagnetic wave. When this TE wave crosses the interfaces two horizontal

shear waves are generated. These can be seen in the right graph as the wavefields generated at the interface level and propagating up and downgoing.

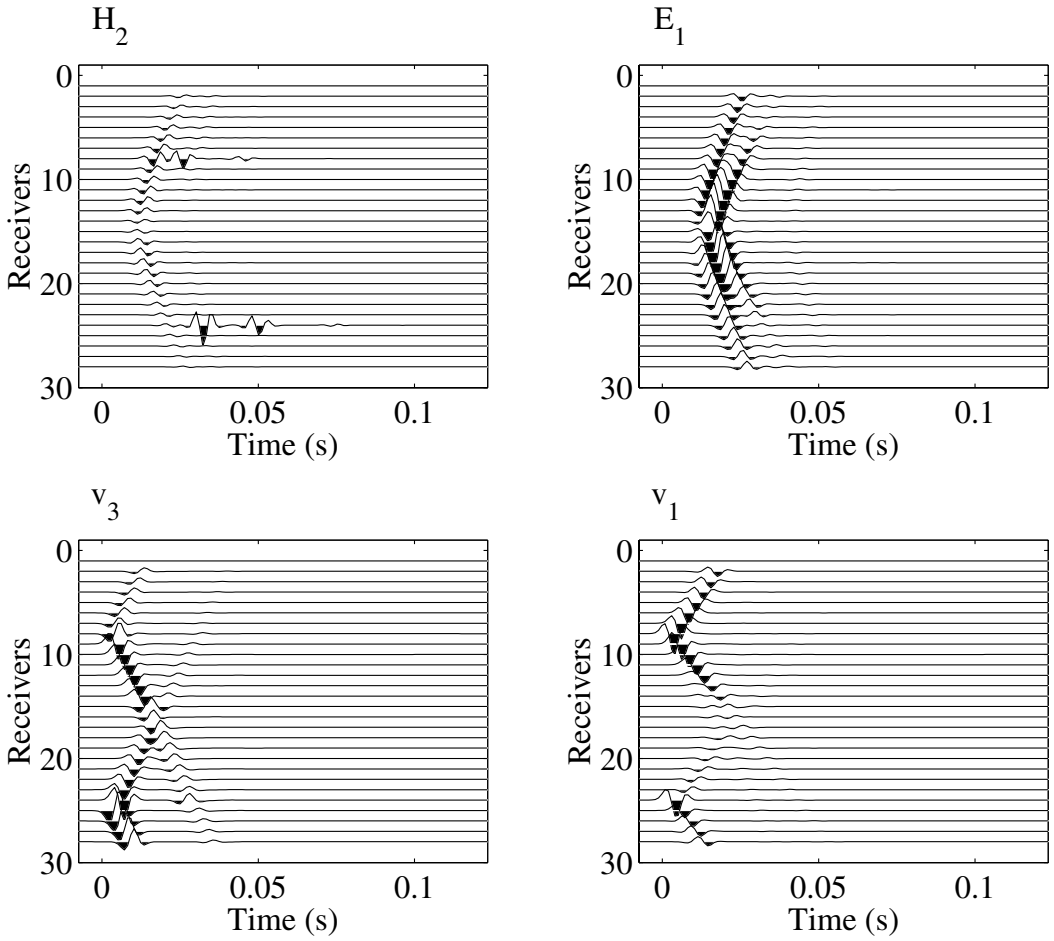

Figure 4.36: *Line source response for the two-way wellbore to wellbore simulation of the P-SV-TM coupling in the (x_1,x_2,t) domain. The wellbore separation is 30 m and the media parameters are those of Table 4.1. Upper graphs: the receivers measure H_2 and E_1, and the source is a bulk and fluid force in the x_1 direction, f_1^b and f_1^f. Lower graphs: the receivers measure v_3 and v_1, and the source is an electric current in the x_1 direction, J_1^e.*

In Figure 4.36 we have the two-way wellbore to wellbore simulation of the P-SV-TM coupling in the (x_1,x_3,t) domain. The wellbore separation is 30 m and the media parameters are those of Table 4.1. In the upper graphs we show

the measurements from the receivers H_2 and E_1 respectively, while the source is a bulk and fluid force in the x_1 direction. In the lower graphs we show the measurements from the receivers v_3 and v_1 respectively, while the source is an electric current in the x_1 direction, J_1^e.

In the upper left graph we have the H_2 field measured from a f_1 source. Here we see several arrivals. The first one is the electromagnetic pulse from the mechanical source that arrives to all the receivers at the same time. Next arrival is the electric field contained inside the fast-P wave and finally the seismo-electric conversion at both interfaces from the shear wave, although the vertical shear wave is not visible with this receiver.

In the upper right graph we have the E_1 field measured when using a f_1 source. Here we see two very close arrivals, these are the electric field travelling with both seismic waves, vertical shear and fast-P waves. Note that when the shear waves encounters the interfaces at receivers 8 and 24 there is a conversion that can be seen in the previous graph.

In the lower left graph we have the v_3 field measured from a J_1^e source. In this case the amplitudes of the traces have been normalized in order to show the fast-P waves generated at the interfaces. What we find here without the normalization is just two strong pulses at the receivers close to the interfaces, and from there the fast-P waves attenuate very rapidly.

In the lower right graph we have the v_1 field measured from a J_1^e source. Here we see the mechanical disturbance that travels along with the electromagnetic wave generated at the source. In this case there are seismic waves generated at the interfaces, but due to the difference of amplitude they don't show on the graph.

4.5 Conclusions

In this chapter we have derived global reflection and transmission coefficients, and based on them we have built models for VSEP (vertical seismo-electric profile) and wellbore to wellbore surveys.

In the second section we have derived the global reflection and transmission coefficients for the seismo-electric effect based on the work by Kennett. Unlike the local reflection coefficients derived in the previous chapter, these coefficients take into account all the reflections and transmissions among the layers above and below the n^{th} interface, including the internal multiples.

In the following section we have used the global coefficients to derive ex-

pressions to model a vertical seismo-electric profile (VSEP), where we see how wavefields travel down a wellbore and are measured by different types of receivers after being reflected and refracted in the interfaces between media. This simulation has been done in the (x_1, x_3, t) domain, this means that the result is a x_1, x_3, t datacube that we can slice in different directions. One interesting result is to study the evolution of the one-way and two-way wavefields along the x_1, x_3 plane with time, as shown in section 4.3.3.

In the next section we have developed a wellbore to wellbore model. This model has been contructed as two VSEP one on top of the other. The upper one has the source at the bottom and the lower one has the source at the top. These two VSEP setups are connected using the outgoing wavefields of one as input fields in the other in an iterative loop. This model has also been done in the (x_1, x_3, t) domain.

By comparing the results of the VSEP and the wellbore to wellbore simulations we logically find similarities. One of them is that the arrival time for a seismo-electric conversion is the same in both cases (assuming that both wells are in the same media and both sources at the same depth), since this will be produced as soon as the incident wave crosses the interface. This means that the wellbore to wellbore seismo-electric survey, or a walk-away VSEP would not give better results than a normal VSEP setup for a horizontally layered medium where the only discontinuities are among the layers. If we have to consider discontinuities in the x_1 direction then the wellbore to wellbore setup could improve the measurements.

In the next chapter we will analyze the information we can actually extract from the subsurface in a seismo-electric survey and what kind of medium parameter contrasts we can detect better than others.

Chapter 5

Sensitivity analysis of inverted reflection coefficients

5.1 Introduction

In the previous chapters we have seen simulations of different kinds of seismo-electric surveys. Each of them has certain advantages and disadvantages, and the reason to choose one over the another configuration is to optimize the information about the medium parameters we can extract of the surrounding area. However this is obviously not as easy as it sounds and there are actually very strong limitations in this method. In this chapter we analyze the information we can actually extract from the subsurface in a seismo-electric survey and its limitations as a geophysical tool. We look at the reflections we obtain from different types of interfaces, and the different sensitivities the seismo-electric coupling has to those contrasts in the medium parameters.

First we compare the reflection coefficients with their inverted counterparts as functions of the ray parameter p. There we see how only for low values of the ray parameter there is a match between both coefficients.

Next we use a cost function to compare the forward and the inverted coefficients for different types of interfaces. There we see the dependency of the cost function with the type and magnitude of the medium parameter contrast.

Finally we try to reconstruct a reflection coefficient from synthetic measurements. For this we use an optimization routine that searches for the medium parameters that give the minimum difference between the coefficient calculated from the field data and the modeled one.

5.2 Inversion of the seismo-electric reflection coefficient

In this section we compare the inverted reflection coefficients with the forward reflection coefficients. This way we check the reliability of the inverted seismo-electric reflection coefficients.

In Section 3.7 we presented a one-way reflection model that will be the basis of our inversion. This model describes the one-way wavefields that arrive to the surface after a reflection at a shallow interface. It is described by equation (3.80) and can be seen in Figure 3.11,

$$\tilde{\mathbf{P}}^{-} = \tilde{\mathbf{W}}^{-}\tilde{\mathbf{r}}^{+}\tilde{\mathbf{W}}^{+}. \tag{5.1}$$

Writing the coefficient $\tilde{\mathbf{r}}^{+}$ as a function of the one-way wavefield arriving to the surface $\tilde{\mathbf{P}}^{-}$ yields

$$\tilde{\mathbf{r}}^{\mathrm{i}} = \left(\tilde{\mathbf{W}}^{-}\right)^{-1}\tilde{\mathbf{P}}^{-}\left(\tilde{\mathbf{W}}^{+}\right)^{-1} \tag{5.2}$$

where the superscript $^{\mathrm{i}}$ denotes inverted reflection coefficient, opposed to the superscript $^{\mathrm{f}}$ for the forward reflection coefficient, which calculation has been described in section 3.3. In the coming expressions we skip the use of the $+$ or - superscript in $\tilde{r}^{\mathrm{i}}$ since we only consider the reflection coefficients from downgoing incident waves. Equation (5.2) gives the reflection coefficient as a function of the one-way wavefield $\tilde{\mathbf{P}}^{-}$. This means that from the reflected wavefield arriving to the surface and assuming that we know the depth of the interface we can derive the reflection coefficient from that interface, and since we know the medium parameters from the layer above it, we can derive the properties of the layer below the interface.

Next we calculate the forward and inverted coefficients of different types of contrasts. For this we choose a setup similar to the one used in Section 3.7, where there are two porous media separated by a horizontal interface. All the medium properties are the same for both media and equal to those of medium 2 in Table 3.1 except the contrast property. In a porosity contrast $\phi^{\mathrm{u}} = 0.4$, in an ion concentration contrast $C^{\mathrm{u}} = 10^{-6}$ N and in a shear modulus contrast $G^{\mathrm{fr}} = 9 \cdot 10^{8}$ Pa.

Once we obtain the inverted reflection coefficients $\tilde{\mathbf{r}}^{\mathrm{i}}$ we compare them with their corresponding forward coefficients to see how well can they be reconstructed from measurements, and what contrasts are detectable in a reliable way.

After doing all this we see that in the inverted seismo-electric reflection coefficients match perfectly the corresponding forward coefficient for values of p corresponding with the homogeneous reflected wave.

5.3 Cost Function

In the previous section we have defined the inverted reflection coefficient from the arriving wavefield $\tilde{\mathbf{P}}^{-}$ in equation (5.2). In this section we study the behavior of the inverted reflection coefficients as functions of the medium parameters ϕ, C, and G^{fr}. To do this we use a cost function with L_2 norm where we compare the forward with the inverted coefficients

$$\tilde{C}_{\text{m,n}}(\phi, C, G^{\text{fr}}) = \left[\frac{\sum_{p_1,\omega} \left| \tilde{r}^{\text{f}}_{\text{m,n}}(p_1, \omega, \phi, C, G^{\text{fr}}) - \tilde{r}^{\text{i}}_{\text{m,n}}(p_1, \omega) \right|^2}{\sum_{p_1,\omega} \left| \tilde{r}^{\text{i}}_{\text{m,n}}(p_1, \omega) \right|^2} \right]^{1/2}, \qquad (5.3)$$

where $\tilde{r}^{\text{f}}_{\text{m,n}}(p_1, \omega, \phi, C, G^{\text{fr}})$ is the forward reflection coefficient derived in Section 3.3 and $\tilde{r}^{\text{i}}_{\text{m,n}}(p_1, \omega)$ is the reflection coefficient inverted from the synthetic data in previous section, equation (5.2). The letters of the subscripts $_{\text{m,n}}$ stand for $m, n = \{P_f, P_s, S_v, TM\}$ for the P-SV-TM coupling, or $m, n = \{S_h, TE\}$ for the SH-TE coupling. Therefore we obtain a cost function for every type of reflection, e.g. $\tilde{C}_{TM,S_v}(\phi, C, G^{\text{fr}})$ gives us the cost function of the reflection coefficients for an incident vertical shear wave and a reflected electromagnetic TM wave as a function of the porosity, ion concentration and shear modulus. In this L_2 norm we sum the reflection coefficients over p_1 and ω. The range of p_1 goes from normal incidence until the reflected wave becomes evanescent, while the range of ω goes from 100Hz till 1kHz. This way we use all the information available in all the useful incidence angles as well as in the different frequencies contained in the mentioned frequency range. We produce a cost function that is a function of the medium parameters ϕ, C and G^{fr} to study the sensitivity of the different reflection coefficients to contrasts in these medium properties.

In order to observe this we use a setup similar to the one used in section 3.3.1, but in this case we use a range of values for the lower medium while keeping the parameters in the upper medium constant to simulate a seismo-electric survey where we know the properties of the uppermost layer (the Earth's surface), but

certain properties of the layer below the interface are unknown. The values for these parameters can be found in Table 5.1. The forward reflection coefficient $\tilde{r}^{\mathrm{f}}(\phi, C, G^{\mathrm{fr}})$ is used in the cost function as a function of the medium parameter ranges found on the second column of Table 5.1, while the inverse reflection coefficient $\tilde{r}^{\mathrm{i}}$ is used with the medium parameter values found in the third and fourth columns of Table 5.1. The cost function is finally a function of ϕ, C and G^{fr}, and in the following figures we will show 2D slices of this function.

We expect the cost function to give us a measure of the difference between the forward and the inverted reflection coefficients. We assume that the parameter values for those used in $\tilde{r}^{\mathrm{i}}$ are inside the range used in $\tilde{r}^{\mathrm{f}}(\phi, C, G^{\mathrm{fr}})$. At the point where both coefficients are equal or their values are closest, there is a minimum in the cost function. The coordinates of this minimum give us the values of these parameters in the lower medium.

Parameter	Lower medium range	Lower medium value	Upper medium value
ϕ	$0.1 - 0.4$	0.17	0.25
C	$10^{-1} - 10^{-4}$ mol/l	$5 \cdot 10^{-3}$ mol/l	$5 \cdot 10^{-4}$ mol/l
G^{fr}	$10^{8} - 10^{11}$ Pa	$5.33 \cdot 10^{8}$ Pa	$1.15 \cdot 10^{9}$ Pa

Table 5.1: *medium parameters*

5.3.1 Cost functions for the reflection coefficient of the SH-TE coupling

In this section we present the cost functions of the SH-TE coupling reflection coefficients. The figures of the cost functions shown in this section only include the reflection coefficients of the conversion from seismic to electromagnetic. We show a series of figures composed of two graphs, the one in the left shows a grey scale image of the cost function as a function of two of the lower medium parameters, and the graph on the right shows a profile of the cost function across the minimum, so it is shown clearly where the minimum is. This is necessary in some cases where the position of the minimum that points to the lower medium parameter value is not clear.

These grey scale images in the coming graphs are shown in logarithmic scale to expose a position of the minimum that is not always visible. Similarly the

sampling for the shear modulus and the ion concentration are logarithmic. Although this hinders the easy reading of the axis, it makes sure that the sampling of the cost function is done in relevant steps. As mentioned before, at the point where $\tilde{\mathbf{r}}^{\mathrm{f}}(\phi, C, G^{\mathrm{fr}})$ equals $\tilde{\mathbf{r}}^{\mathrm{i}}$ the cost function is zero, and $\log(0) = -\infty$. This is the reason why there is a small gap at the minimum in the profile plots.

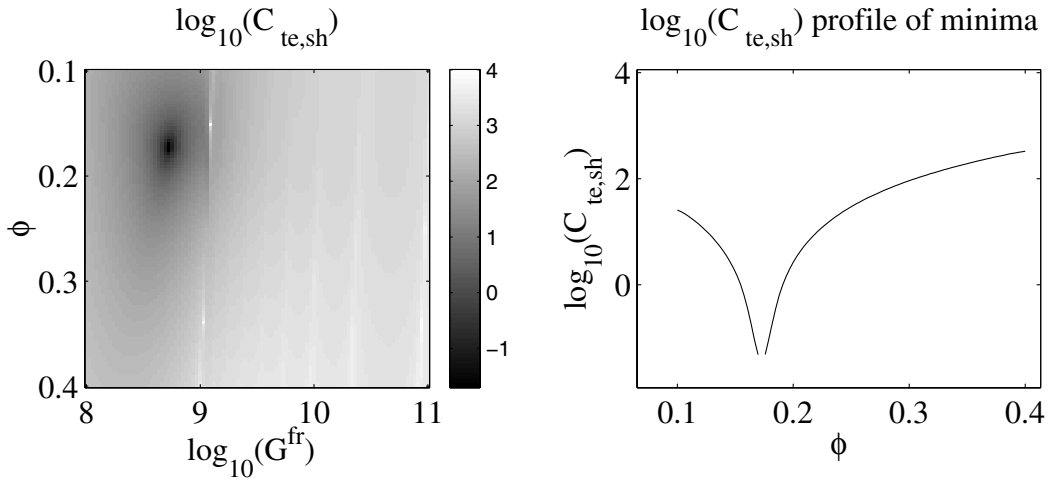

Figure 5.1: *Left: Cost function $C_{\mathrm{te,sh}}(\phi, G^{\mathrm{fr}})$. Right: Profile of the minima line of the left graph where we see the minimum of this line pointing to the porosity value of the lower medium.*

On the left graph of Figure 5.1 we see the cost function $C_{\mathrm{te,sh}}(\phi, G^{\mathrm{fr}})$ for a porosity and shear modulus contrast. The shear modulus and the grey scales are logarithmic. We see in this graph a very clear minimum that fits with the medium value shown in Table 5.1. On the right graph we see a profile of this cost function along the ϕ direction where it becomes clear where the minimum is located.

It must be noted here that the shape of the cost function around the minimum is not the same depending on the direction of the reflection. In this case the reflection occurs from high to low values of the porosity and the shear modulus. These results would be different if, for example the reflection was in the opposite direction, i.e. $\mathbf{R}^{-}$ instead of $\mathbf{R}^{+}$.

In the next case, the cost function for an ion concentration and shear modulus contrast $C_{\mathrm{te,sh}}(C, G)$ on figure 5.2, the area of the cost function around the minimum is extended into a trench rendering the minimum difficult to locate

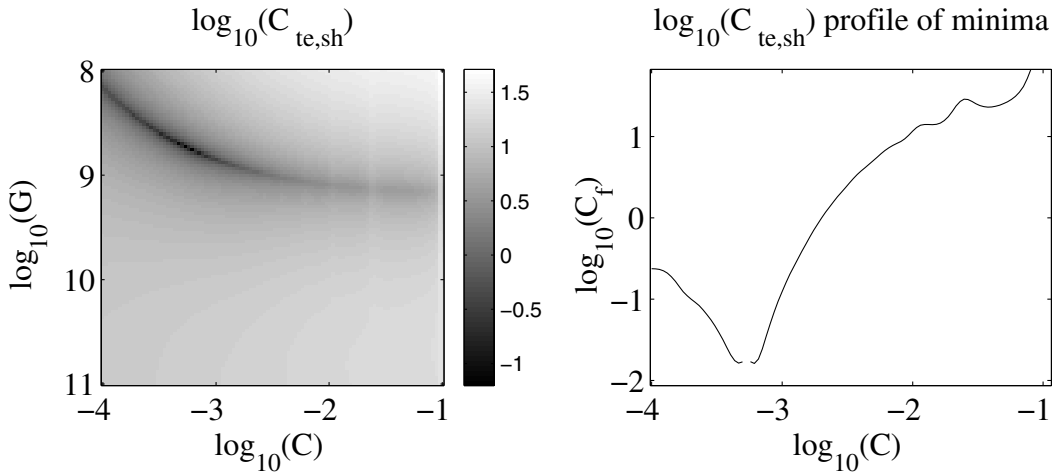

Figure 5.2: *Left: Cost function $C_{\mathrm{sh,te}}(C, G)$. Right: Profile of the minima line of the left graph where we see the minimum of this line pointing to the ion concentration value of the lower medium.*

among the aparent local minima. However if we look at the profile we can clearly find the minimum pointing at the corresponding lower medium value.

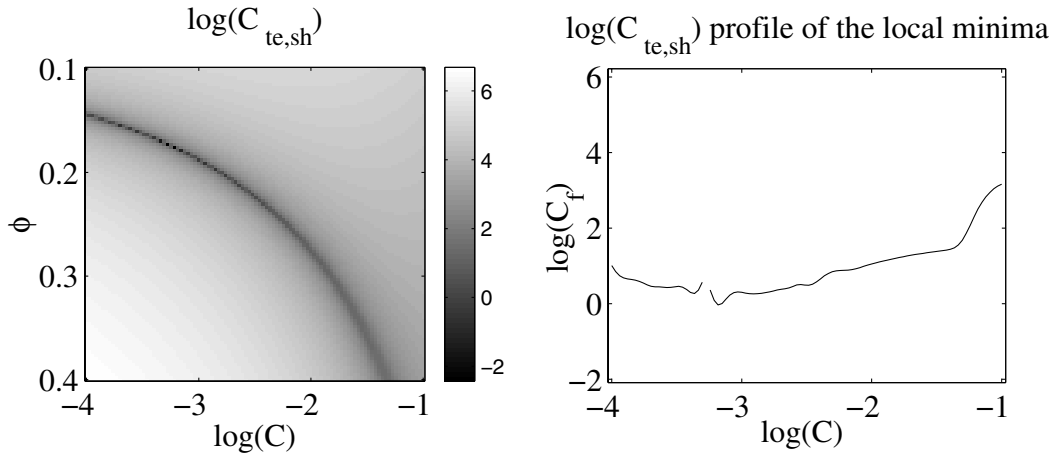

Figure 5.3: *Left: Cost function $C_{\mathrm{sh,te}}(\phi, C)$. Right:Profile of the minima line of the left graph where we see the minimum of this line pointing to the ion concentration value of the lower medium.*

In the last cost function of the SH-TE coupling $C_{\mathrm{te,sh}}(\phi, C)$, for a porosity

and ion concentration contrast, we see a similar structure around the minimum as in the previous case. On the left graph of Figure 5.3 we see a long trench connecting the low porosity and ion concentration with the high porosity and ion concentration values. In this case the location of the minimum in the left graph is impossible to identify due to the many local minima and we need to look at the plot in the right graph that points to the correspondent lower medium value. However note that even the profile doesn't point to the minimum as clearly as in previous figures, and the overall difference between the inverted and forward coefficients is less pronounced in the range.

5.3.2 Cost functions for the reflection coefficient of the P-SV-TM coupling

Here we present the cost functions of the P-SV-TM coupling reflection coefficients. In addition to the interaction between shear and electromagnetic waves, this coupling contains also conversion from and to compressional waves. Since compressional and shear waves have different sensitivity to certain medium parameters, this coupling gives us more information on the medium parameters than the previous where only two wave types were exchanging energy. Here we also choose the cost function to depend on ϕ, C, and G^{fr} for all the seismo-electric conversions. This way we compare the cost functions of both couplings.

In this coupling we have more wave types, thus more data to be fed into the cost function. We combine the cost functions as

$$\tilde{\mathbf{C}}_{\mathrm{PSVTM}} = \left[\frac{1}{2}|\tilde{\mathbf{C}}_{\mathrm{tm,pf}}|^2 + \frac{1}{2}|\tilde{\mathbf{C}}_{\mathrm{tm,sv}}|^2\right]^{1/2}, \tag{5.4}$$

where $\tilde{\mathbf{C}}_{\mathrm{tm,pf}}$ and $\tilde{\mathbf{C}}_{\mathrm{tm,sv}}$ are obtained as in equation (5.3). This way we produce a more accurate cost function that gives better results than the individual cost functions. In the coming figures there are some results for the same contrasts used for $\tilde{\mathbf{C}}_{\mathrm{SHTE}}$.

In figure 5.4 we find the cost function $C_{\mathrm{PSVTM}}(\phi, C)$ for the ranges of ϕ and C mentioned in table 5.1. At the right hand side we have the profile of this cost function that crosses the minimum as a function of the ion concentration. Note the similarity with Figure 5.3 where $\tilde{\mathbf{C}}_{\mathrm{SHTE}}$ is shown for the same type of interface. However, in this case the location of the minimum in the cost function is more defined.

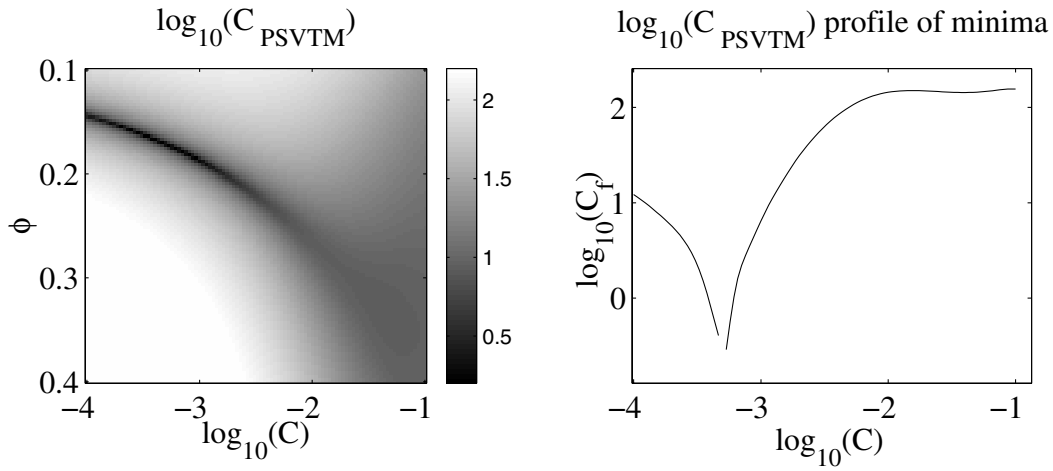

Figure 5.4: *Left: Cost function* $\tilde{\mathbf{C}}_{\mathrm{PSVTM}}(\phi, C)$ *for a contrast in porosity and ion concentration. Right: Profile of cost function across the minimum as a function of* $\log_{10}(C)$.

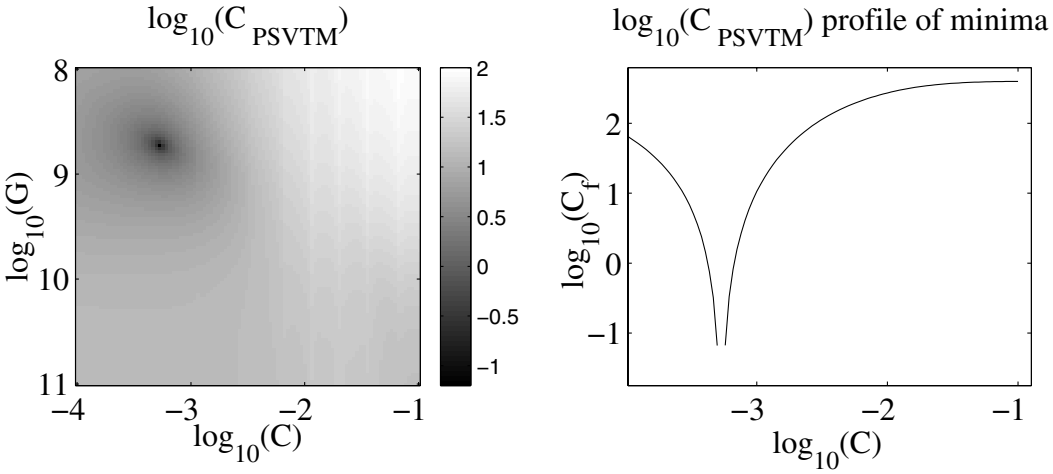

Figure 5.5: *Left: Cost function* $\tilde{\mathbf{C}}_{\mathrm{PSVTM}}(G^{\mathrm{fr}}, C)$ *for a contrast in porosity and ion concentration. Right: Profile of cost function across the minimum as a function of* $\log_{10}(C)$.

In figure 5.5 we have the cost function $\tilde{\mathbf{C}}_{\mathrm{PSVTM}}(G^{\mathrm{fr}}, C)$ for the ranges of G^{fr} and C shown on table 5.1, and its profile across the minimum as a function of $\log_{10}(C)$. According to our model, the minimum in the cost function should be

pointing to an ion concentration in the lower medium of 0.17 mol/l and a shear modulus of $5.33 \cdot 10^8$ Pa. The location of the minimum is very clear and without much correlation along any of the parameter's axis.

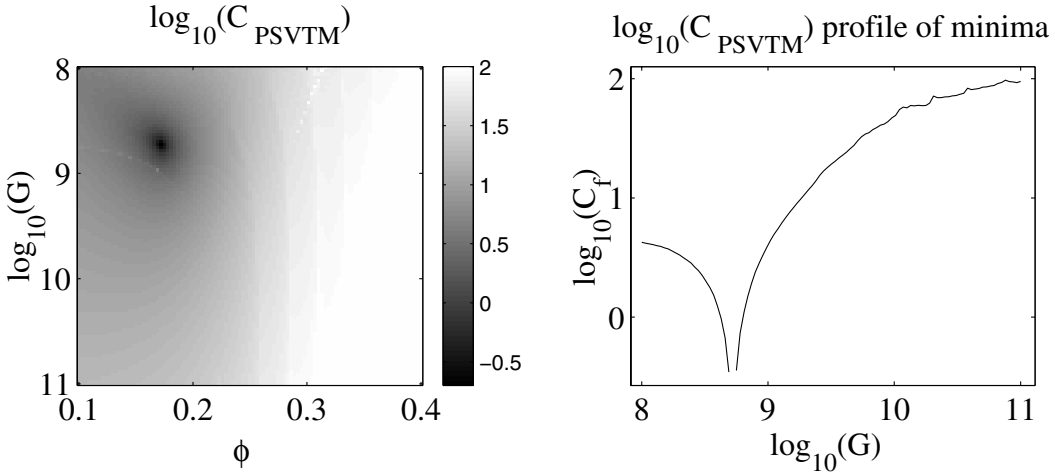

Figure 5.6: *Left: Cost function $\tilde{\mathbf{C}}_{\mathrm{PSVTM}}(\phi, G^{\mathrm{fr}})$ for a contrast in porosity and ion concentration. Right: Profile of cost function across the minimum as a function of ϕ.*

In figure 5.6 we have the cost function $\tilde{\mathbf{C}}_{\mathrm{PSVTM}}(\phi, G^{\mathrm{fr}})$. In both graphs we see a very clear minimum that points exactly to the values of Table 5.1. The results for this type of contrast are also very similar to those of the SH-TE coupling.

5.4 Simulated field data example

Finally we simulate the actual data process from the measurement on the field until we obtain the medium property value. We will show next how we can obtain the depth, porosity and ion concentration of a certain layer from seismo-electric measurements and what combination of sources and receivers are most suited for this purpose.

We assume we have a homogeneous medium saturated with water in which there is a contrast in the medium properties at a certain depth. We also assume that our measuring setup is split-spread with different kinds of sources, therefore

we use the results of Chapter 3 as our measurements. The reflection model we use is

$$\hat{\mathbf{Q}} = \hat{\mathbf{C}}_{\mathrm{r}}\hat{\mathbf{W}}^{-}\hat{\mathbf{r}}^{+}\hat{\mathbf{W}}^{+}\hat{\mathbf{S}} = \hat{\mathbf{C}}_{\mathrm{r}}\hat{\mathbf{P}}^{-}\hat{\mathbf{S}}, \tag{5.5}$$

where $\hat{\mathbf{Q}}$ and $\hat{\mathbf{P}}^{-}$ contain the two-way and one-way wavefields respectively, and $\hat{\mathbf{S}}$ and $\hat{\mathbf{Cr}}$ contain all the source and receiver types respectively. As we already saw, the result of this model comes in the form of a 4×4 matrix with the 16 combinations of source and receiver types defined in Chapter 3, Section 3.7.2.

In order to simulate real measurements we reduce the number of receiver positions to 64 and we truncate the computer model values of the measurements to 3 digits after the decimal point. Additionally we normalized the amplitudes coming from the different receivers in order to simulate the stacking of measurements, and finally we added noise to reduce the s/n ratio.

With this synthetic but realistic data set we pass to the processing stage. The dataset is Fourier transformed from (x_1,t) to the (k_x, ω) domain. Once in this domain we can invert and extrapolate the fields back to the interface. First we decompose the two-way wavefields into one-way wavefields as

$$\hat{\mathbf{P}}^{-} = \hat{\mathbf{C}}_{\mathrm{r}}^{-1}\hat{\mathbf{Q}} \quad \hat{\mathbf{S}}^{-1}, \tag{5.6}$$

and then we invert the wave extrapolation back to the interface level

$$\hat{\mathbf{r}}^{\mathrm{i}} = \left(\hat{\mathbf{W}}^{-}\right)^{-1}\hat{\mathbf{P}}^{-} \quad \left(\hat{\mathbf{W}}^{+}\right)^{-1}. \tag{5.7}$$

This could also be done in one step

$$\hat{\mathbf{r}}^{\mathrm{i}} = \left(\hat{\mathbf{W}}^{-}\right)^{-1}\hat{\mathbf{C}}_{\mathrm{r}}^{-1}\hat{\mathbf{Q}} \quad \hat{\mathbf{S}}^{-1}\left(\hat{\mathbf{W}}^{+}\right)^{-1}. \tag{5.8}$$

Once we obtain the reflection coefficient we use a cost function as we did in previous section. We combine the cost functions of the different reflection coefficients as

$$\tilde{C}^{\mathrm{es}}_{\mathrm{psvtm}} = \left[\frac{1}{2}|\tilde{C}_{\mathrm{tm,pf}}|^2 + \frac{1}{2}|\tilde{C}_{\mathrm{tm,sv}}|^2\right]^{1/2}, \tag{5.9}$$

$$\tilde{C}^{\mathrm{se}}_{\mathrm{psvtm}} = \left[\frac{1}{2}|\tilde{C}_{\mathrm{pf,tm}}|^2 + \frac{1}{2}|\tilde{C}_{\mathrm{sv,tm}}|^2\right]^{1/2}, \tag{5.10}$$

where $\tilde{C}$ inside previous expressions are the different cost functions for the different types of reflections denoted in the subscript, and the superscripts $^{\mathrm{se,es}}$ stand

for conversion from seismic to electromagnetic and vice versa respectively. These cost functions are obtained as in equation (5.3). This way we combine all the information available giving better results than the individual cost functions.

In the following figures we show the cost functions resulting from the derivation mentioned above. We assume a medium as the one described in Table 3.1. As a first approximation we use the full forward model without introducing noise or truncating the dataset. The figures contain two graphs, on the left we compare the conversions from seismic to electromagnetic and on the right vice versa.

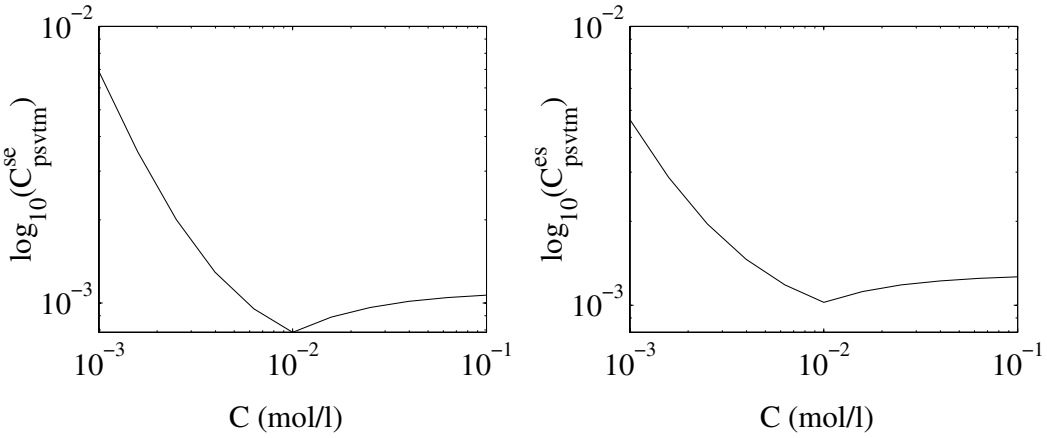

Figure 5.7: *Cost function $\hat{C}_{\mathrm{psvtm}}(c)$. The figure shows the cost functions as defined in equations (5.9) and (5.10) as a function of the ion concentration.*

In Figure 5.7 we have the cost functions of the P-SV-TM coupling reflection coefficients. These cost functions are expressed as functions of the ion concentration C. In this case the ion concentration at the lower medium is set to 10^{-2} mol/l, and we see how the minimum points to the correct value of the lower medium.

In Figure 5.8 we have again the cost functions corresponding with the P-SV-TM coupling reflection coefficients. These cost functions are expressed as function of the porosity ϕ. In this case the porosity at the lower interface is set to 0.2, and we see how the minima point to the right ϕ value of the lower medium.

As we have seen in Figures 5.7 and 5.8 as well as in the first sections of this chapter the properties of the medium under the interface can be in theory reconstructed. However there are many other factors playing a role in these cost functions and in the coming figures we show the effect of some of these factors

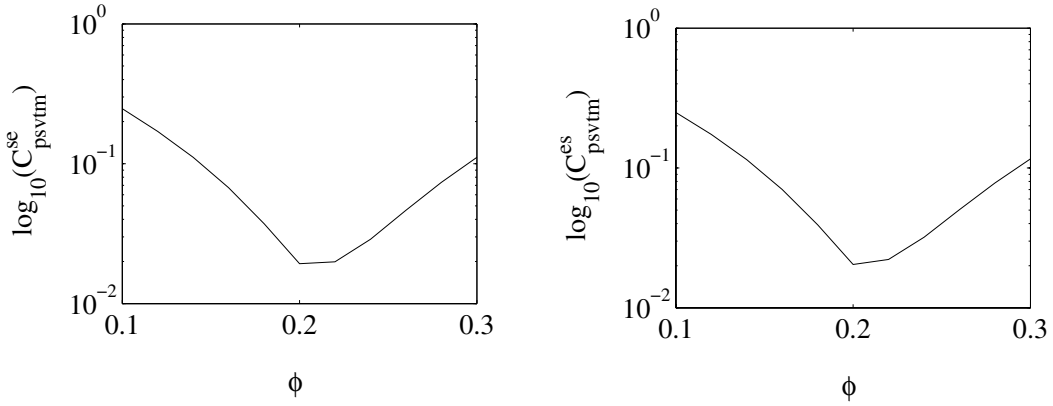

Figure 5.8: *Cost function $\hat{C}_{\mathrm{psvtm}}(\phi)$. The figure shows the cost functions as defined in equations (5.9 and 5.10) as a function of the porosity.*

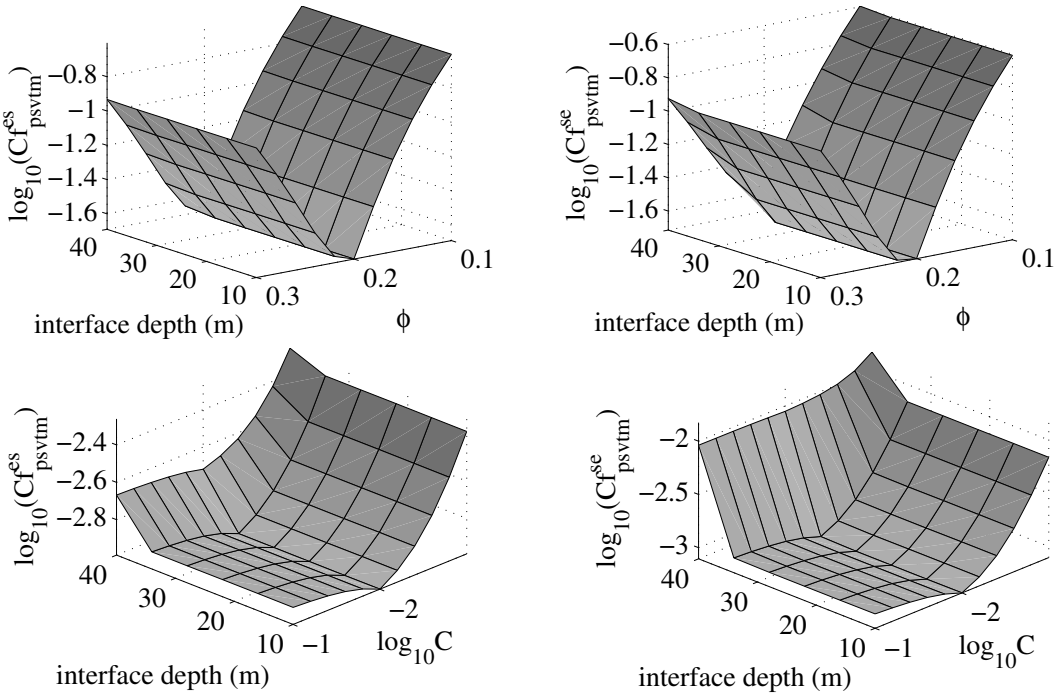

Figure 5.9: *Upper graphs: $\hat{C}(z, c)$. Lower graphs: $\hat{C}(z, \phi)$. The figure shows the P-SV-TM coupling cost functions as functions of the interface depth that ranges from 10 m to 40 m.*

like the depth of the interface, the truncation of the dataset or the noise in the measurements.

In figure 5.9 we see the cost functions $\hat{C}(z, c)$ and $\hat{C}(z, \phi)$ where the cost function is plotted as a function of the interface depth and the porosity ϕ in the upper graphs and the ion concentration c in the lower graphs. The two graphs on the left show the cost function for the conversion from electromagnetic to seismic and the two on the right for the opposite conversion. If we slice these 3D surfaces in the "interface depth" direction we would obtain plots as in Figures 5.7 or 5.8 where the cost function is shown for a fixed depth, in this case 20 m. If we look at $\hat{C}^{\mathrm{se,es}}_{\mathrm{psvtm}}(z, \phi)$ we see that the depth has not much effect on this cost function and that its shape remains very constant along the "interface depth" axis. If we look now at $\hat{C}^{\mathrm{se,es}}_{\mathrm{psvtm}}(z, c)$ we find that for the first 30 m the cost function does not change much with the interface depth, but afterwards rises about one order of magnitude for the seismic to electric conversion, and less for the opposite conversion.

Our next step is to fully simulate the fieldwork measurements by truncating, adding noise and filtering the results of the two-way reflection model. We begin simulating the limited amount of information the receivers can gather. Our computer simulations are done in double precision, this means the use of floating point for all computations, including the simulated measurements and their processing. Therefore we are going to reduce the sampling of the simulation results and truncate the number of decimal figures. With this we simulate the geophone spacing in the measuring line and the limited number of figures the receivers can record. In Figure 5.10 we see the effect the truncation of the data set has on the cost functions. Again these cost functions are presented as a function of the ion concentration and the porosity. We observe clearly in these figures how the cost functions increase as we use less decimal figures of the dataset.

The next stage in the simulation of the seismo-electric data acquisition is the introduction of noise. For this case we have used only white noise without a specific frequency content or harmonics assuming that we have eliminated it in the preprocessing. In Figure 5.11 we show the effect of the noise introduced in the dataset. We find that logically with decreasing signal to noise ratio the cost function increases, and the location of the minimum shifts towards higher values of the porosity or the ion concentration. It is interesting in this case to note that the conversion from seismic to electromagnetic resolves better the porosity of the ion concentration than the opposite conversion, from electromagnetic to seismic.

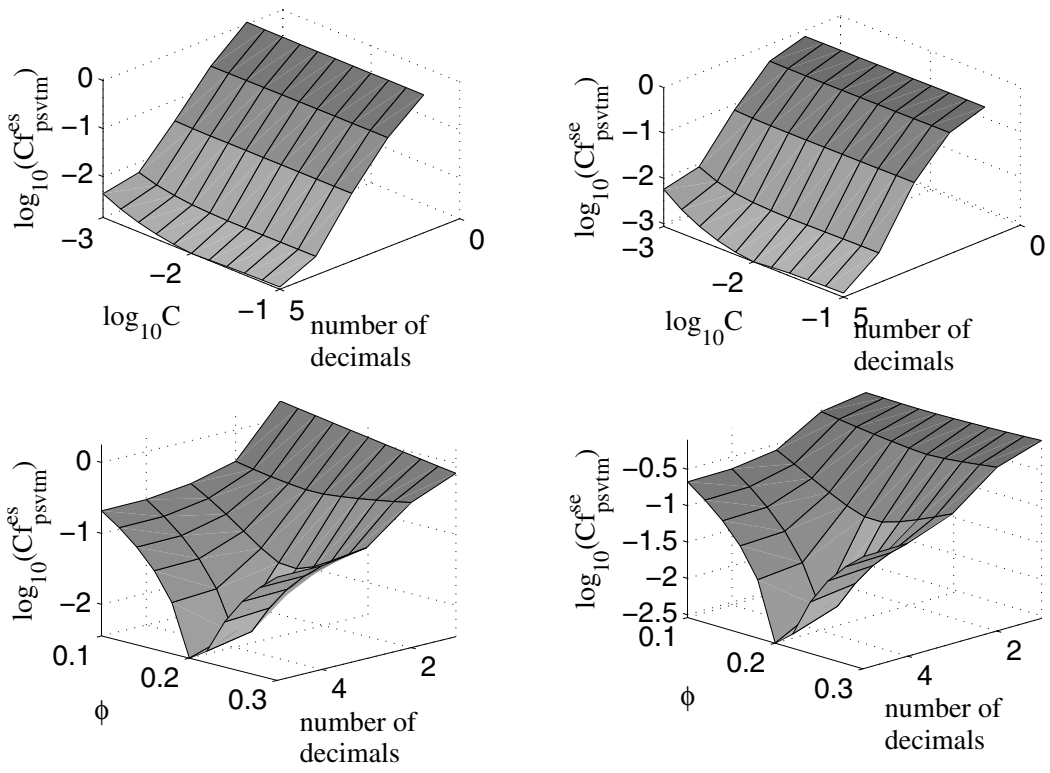

Figure 5.10: *Cost functions $\hat{C}(c)$ and $\hat{C}(\phi)$. The figure shows the P-SV-TM coupling cost functions as a function of the ion concentration and the figure truncation of the dataset.*

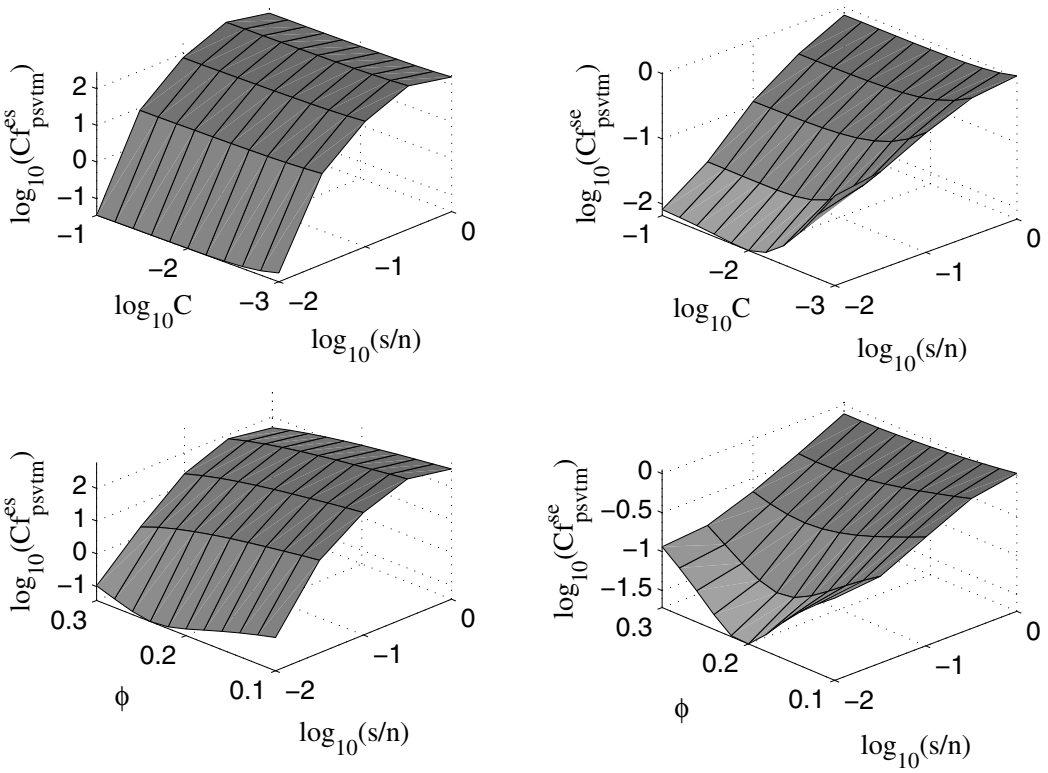

Figure 5.11: *Cost functions $\hat{C}(s/n, c)$. The figure shows the P-SV-TM coupling cost functions as a function of the ion concentration and the signal to noise ratio of the noise introduce in the dataset.*

5.5 Conclusions

In this chapter we have studied the sensitivity of the reflection coefficients of the seismo-electric conversions to contrasts in medium properties, and the reliability of the inverted reflection coefficients. The object of this is to theoretically test if we can actually obtain any useful information from the subsurface using data from the seismo-electric conversions that take place there.

We have compared the forward with the inverted coefficients for a certain set of medium property values using a cost function with norm L_2. The cost function shows the difference between these two coefficients, and more importantly it shows where it is minimal. The coordinates of that minimum point are the values of the lower medium parameters. We show in the cost function graphs that there is actually a region where the cost functions is minimal, and within that region there is indeed a minimum, but often difficult to find.

Finally we have simulated a real data set from a fieldwork where we use different sources and receivers. We have transformed these data to the (k_1, ω) domain and there we have extrapolated the one-way wavefields back to the interface level to obtain the reflection coefficient. When we use the full two-way model dataset, we find the values of the medium property responsible for the contrast after using a cost function. We have considered in some examples the role of factors as the interface depth, realistic receivers or noise in the measurements in the cost functions and we have seen that naturally for a deeper interface, poorly recorded signal or high noise the cost function becomes larger making the determination of the medium properties more difficult.

Chapter 6

Conclusions

We began this PhD. thesis addressing the question: what can we measure with the seismo-electric effect, and how? To orderly present our results we divided this thesis in five chapters plus the current one, six. The first chapter contains the usual general introduction and the literature review to put the reader into perspective.

In the second chapter of this thesis we obtained the wave equation for the coupled seismic and electric waves in a porous medium. We did it in the frequency domain for the 3-D and 2-D cases, and in the ray parameter domain for the 2-D and 1-D cases. We began with Pride's equations for the coupled electromagnetics and acoustics of porous media in the frequency domain [18], and expressed the vertical variations of chosen wavefields in terms of their lateral variation, and combined them into the matrix-vector equation

$$\frac{\partial \hat{\mathbf{Q}}}{\partial x_3} = \hat{\mathbf{A}}\hat{\mathbf{Q}} + \hat{\mathbf{D}}, \tag{6.1}$$

where $\hat{\mathbf{Q}}$ is a vector that contains the two-way wavefields that according Deresiewicz and Skalak [5] remain continuous across an interface. This was firstly done for the 3-D case, and later to simplify our model we applied it to a 2-D situation. In this case we considered a medium of horizontal homogeneous layers of porous media. In this medium the waves propagate only in the x_1x_3 plane, therefore all the derivatives with respect to x_2 are zero. This simplified dramatically the structure of matrix $\hat{\mathbf{A}}$ as it can be seen in equations (2.98)-(2.101). At this point the wave equation separated into two uncoupled partial differential equations that described the two types of coupling to be found on the seismo-electric effect: the SH-TE and the P-SV-TM couplings.

Next we Radon transformed the wave equation from the $(\mathbf{x}, \omega)$ domain to the (p_1, ω) domain, this replaced all derivatives with respect to x_1 by $-j\omega p_1$. We then rearranged the matrix $\hat{\mathbf{A}}$ and the vector $\hat{\mathbf{Q}}$ in such a way that the coupling between the compressional, the vertical shear and the TM electromagnetic waves on one hand, and the horizontal shear with the TE electromagnetic wave on the other hand became clear.

This rearranging yielded $\hat{\mathbf{A}}_{\mathrm{H}}$ and $\hat{\mathbf{A}}_{\mathrm{V}}$ and consequently the vectors $\hat{\mathbf{Q}}_{\mathrm{H}}$ and $\hat{\mathbf{Q}}_{\mathrm{V}}$ and a simpler and more compact expression of the wave equations. We presented them in equations (2.111) to (2.117). In the last section of the chapter we looked at the 1-D case, where we proved how the vertical shear and TM electromagnetic waves decouple from the compressional waves in the P-SV-TM coupling. This leaves the compressional waves uncoupled from the electromagnetic waves for normal incidence.

In the third chapter we defined the one-way operators that were used in our seismo-electric survey simulations. We began defining the composition operator that composes the two-way wavefields from one-way wavefields and its inverse that decomposes the two-way wavefields back to one-way wavefields. Once we got the composition operators we could calculate the reflection and transmission coefficients in the (p_1, ω) domain via an scattering matrix. This was done for two types of interfaces: porous/porous and a porous/vacuum. The former simulates two layers in the earth's subsurface while the later simulates the surface of the earth. Next we produced some results where we saw the dependency of the coefficients with the horizontal slowness for certain contrasts in medium properties as the pore fluid ion concentration, porosity or permeability. From these results we saw how the seismo-electric response of an interface is proportional to the contrast in the media properties.

With the reflection coefficients and the wave extrapolation operators we constructed a very simple one-way reflection model where we already observed the arrival times of reflections and conversions between different wavefields. This model was done in the (k_1, ω) domain, and via a Fourier transformation the results were shown in the (x_1, t) domain. This first step was a simplistic approach, yet it helped understanding the seismo-electric conversion at an horizontal interface in the subsurface.

In the next section we derived the decomposition and composition of wavefields at the source and receivers. In our next model the two-way source parameters were decomposed at the source into the one-way wavefields that propagated in the previous model. When these one-way wavefields were reflected back to the surface, they were composed back to the two-way wavefields measured at

the receivers. Via these operators we not only simulated any receiver, but also cancel certain wavefields to better study the interaction of different combinations of wavefields, as well as sources and receivers.

Finally we show a series of examples, one-way and two-way reflections from SH-TE and P-SV-TM couplings. From these we conclude that there are indeed multiple interactions between the seismic and electromagnetic wavefields in both directions, i.e. seismic to electromagnetic and vice versa, making the seismo-electric effect a more complicated case than just conversion from fast-P to electromagnetic waves.

In the fifth chapter we derived the global reflection and transmission coefficients based on the work by Kenneth [10]. Unlike the local reflection coefficients derived in the previous chapter, these coefficients take into account all the reflections and transmissions among the layers above and below the n^{th} interface, including the internal multiples.

Next we used the global coefficients to derive expressions to model a vertical seismo-electric profile (VSEP), where we saw how wavefields travel down and up a wellbore and were measured by different kinds of receivers after being reflected and refracted in the interfaces between media. As well as in previous chapter, the models were derived using just one-way wavefields, and also composing and decomposing the two-way wavefields at the source and receivers. The next step was to include the x_1 dependency in our VSEP model, this way we simulated a complete 2D grid of receivers spread along the x_1x_3 plane. The result of this model was a t, x_1, x_3 datacube where we could look at three types of slices: (t, x_1) as the results of Section 3.7.1, (t, x_3) as the VSEP results of Section 4.3.1 or (x_1, x_3) which gives us snapshots of the wavefields as they propagate with time along the x_1, x_3 plane as the results of Section 4.3.3.

In the second part of Chapter 5 we derived expressions to model a wellbore to wellbore survey based on two complementary VSEP models. Each of these two models simulated the propagation of wavefields above and below the source level. Each of these two models was fed iteratively with the outgoing wavefields of the opposite model to ensure the continuity of wavefields along the x_3 direction. We simulated a wellbore to wellbore survey in which two wellbores are 30 m apart, and we use several sources and receivers in both of them.

In the final chapter we studied the sensitivity of the reflection coefficients of the seismo-electric conversions to contrasts in medium properties, and the reliability of the inverted reflection coefficients. The object of this was to theoretically test if we can actually obtain any useful information from the subsurface using data from the seismo-electric conversions that take place there.

We compared the forward with the inverted coefficients for a certain set of medium property values using a cost function with norm L_2. The cost function showed the difference between these two coefficients, and more importantly it showed where it was minimal. The coordinates of that minimum point are the values of the lower medium parameters. We showed in the cost function graphs that there is actually a region where the cost functions is minimal, and within that region there is indeed a minimum, but it was often difficult to find.

Finally we simulated a real data set from a fieldwork where we use different sources and receivers. We transformed these data to the (k_1, ω) domain and there we extrapolated the one-way wavefields back to the interface level to obtain the reflection coefficient. When we used the full two-way model dataset, we found the values of the medium property responsible for the contrast after using a cost function. We considered also in some examples the role of factors as the interface depth, realistic receivers or noise in the measurements. we saw that naturally for a deeper interface, poorly recorded signal or high noise the cost function became larger making the determination of the medium properties more difficult.

Bibliography

[1] D. Beamish. Characteristics of near-surface electrokinetic coupling. *Geophys. J. Int.*, pages 231–242, 1999.

[2] D. Beamish and R.J. Peart. Electrokinetic geophysics–a review. *Terra Nova*, pages 48–55, 1998.

[3] K. et al Butler. An experimental seismoelectric survey for groundwater exploration in the australian outback. *SEG International Exposition and 72nd Annual Meeting*, 2002.

[4] H. W. et al Deckman. Determination of electrokinetic coupling coefficients. *75th Ann. Internat. Mtg.,Soc. Expl. Geophys., Expanded Abstracts*, 2005.

[5] H. Deresiewick and R. Skalak. On uniqueness in dynamic poroelasticity. *Bull. Seis. Soc. Am.*, pages 783–788, 1963.

[6] J. Frenkel. On the theory of seismic and seismo-electric phenomena in a moist soil. *J. Physics*, pages 230–241, 1944.

[7] C.W. Hunt and M.H. Worthington. Borehole electrokinetic responses in fractured dominated hydraulically conductive zones. *Geophysical Research Letters*, 27(9):1315–1318, May 2000.

[8] T. Ishido and H. Mizutani. Experimental and theoretical basis of electrokinetic phenomena in rock-water systems and its applications to gephysics. *Journal of Geophysical Research*, 86:1763–1775, 1981.

[9] A.G. Ivanov. Effect of electrization of earth layers by elastic waves passing through them. *Dokl. Akad. Nauk SSSR*, 24(1):41–45, 1939.

[10] B.L.N. Kennett. Seismic wave properties in stratified media. *Cambridge University Press*, 1989.

[11] A. Kepic and K. Butler. The art of measuring very low amplitude seismoelectric signals. *EAGE Conference and Exhibition*, 2002.

[12] S.T. Martner and N.R. Sparks. The electroseismic effect. *Geophysics*, 24:297–308, 1959.

[13] O.V. Mikhailov, M.W. Haartsen, and Nafi Toksöz. Electroseismic investigation of the shallow subsurface: Field measurements and numerical modeling. *Geophysics*, 62(1):97–105, jan–feb 1997.

[14] O.V. Mikhailov, J. Queen, and Nafi Toksöz. Using borehole electroseismic measurements to detect and characterize fractured (permeable) zones. *Geophysics*, 65(4):1098–1112, jul–aug 2000.

[15] J. Neev and F.R. Yeatts. Electrokinetic effects in fluid-saturated poroelastic media. *Physical review B*, 40(13), 1989.

[16] E.I. Parkomenko and I.V. Gaskarov. Borehole and laboratory studies of the seismoelectric effect of the second kind in rocks. *Physics of the solid earth*, pages 663–666, 1970.

[17] D.B. et al Pengra. Determination of rock properties by low-frequency ac electrokinetics. *Journal of Geophysical Research*, 104:29485–29508, 1999.

[18] S.R. Pride. Governing equations for the coupled electromagnetics and acoustics of porous media. *Physical Review*, 50(21):678–696, December 1994.

[19] S.R. Pride and M.W. Haartsen. Electroseismic wave properties. *Acoustic Society America*, 100(3):1301–1315, September 1996.

[20] S.R. Pride and F.D. Morgan. Electrokinetic dissipation induced by seismic waves. *Geophysics*, 56(7):914–925, July 1991.

[21] P.M. Reppert and F.D. Morgan. Frequency-dependant electroosmosis. *Journal of colloid and interface science*, 254:372–383, 2002.

[22] P.M. et al Reppert. Frequency-dependant streaming potentials. *Journal of colloid and interface science*, 234:194–203, 2001.

[23] A. H. et al Thompson. Field tests of electroseismic hydrocarbon detection. *75th Ann. Internat. Mtg.,Soc. Expl. Geophys., Expanded Abstracts*, 2005.

[24] A.H. Thompson and G.A. Gist. Geophysical applications of electrokinetic conversion. *Leading Edge*, pages 1169–1173, December 1993.

[25] R.R. Thompson. The seismic electric effect. *Geophysics*, 1:327–335, 1936.

[26] J. van der Kruk. *Three-dimensional Imaging of Multi-component Ground Penetrating Radar Data*. PhD thesis, Delft University of Technology, June 2001.

[27] C.P.A. Wapenaar. *Seismic wave theory*. In preparation.

[28] Kees Wapenaar. Reciprocity theorems for seismoelectric waves. *Journal of Seismic Exploration*, 2003.

[29] Z. Zhu and M.N. Toksoz. Crosshole seismoelectric measurements in borehole models with fractures. *SEG International Exposition and 72nd Annual Meeting*, 2002.

[30] Z. et al Zhu. Experimental studies of electrokinetic conversions in fluid-saturated borehole models. *Geophysics*, 64(5):1349–1356, 1999.

Summary

Seismo-electric profiling is gaining interest as a potential geophysical tool to extract information from the subsurface. In recent years we have seen developments in this field that make us believe that in a relatively short time it will be exploited as a geophysical method. Its sensitivity to changes in pore fluid chemistry makes it ideal for environmental applications as well as a wellbore tool. Besides, if we take into account that in every seismic or electromagnetic survey there are seismo-electric conversions and reflections generated, it makes this method an excellent complement to already known methods.

The objective of this thesis is to study the potential of the seismo-electric effect in known survey methods, and the actual possibilities it offers to retrieve information of the subsurface. We do this by developing a set of operators to describe our models of a simple split-spread shallow survey, VSEP and wellbore to wellbore measurements.

We begin with Pride's equations [18] for the coupled electromagnetics and acoustics of porous media. From Pride's equations we express the vertical variations of chosen wavefields in terms of the lateral variations of the same wavefield and we combine them into a matrix-vector wave equation.

It is shown that for horizontally layered media where the waves propagate in the x_1, x_3 plane the wave equation can be rearranged so that it uncouples into two independent sets of partial differential equations. These two sets of equations show us the two existing cases in the seismo-electric coupling: the P-SV-TM and the SH-TE cases. The P-SV-TM coupling includes the interactions between the compressional, vertical shear and TM electromagnetic waves, while the SH-TE coupling includes the interactions between the horizontal shear and the TE electromagnetic waves. TM and TE stand for "transverse magnetic" and "transverse electric" and the terms refer to the polarization of the magnetic and electric fields in the electromagnetic wave.

We describe the composition operator as a means to compose the two-way

wavefields from the one-way wavefields. We also describe the one-way wavefields as the up or down going individual wave types, and the two-way wavefields as the superposition of up and downgoing wavefields measurable in the field.

We define a seismo-electric survey by means of one-way operators describing each of the phenomena taking place, such as excitation, propagation and reflection. Finally we show examples of two cases where we applied the theory of this chapter, first a simple reflection using just one-way wavefields and second a more complex case including the simulation of the source and receivers.

The next step is to develop a more complex survey model such as a multi-layered medium. We derive the seismo-electric global reflection and transmission coefficients in a similar way as Kennett [10] does for seismic waves. Combining these coefficients we simulate a VSEP (Vertical Seismo-Electric Profile) in the (x_3, t) domain and later in the (x_1, x_3, t) domain. This last result has the form of a datacube into which slices can be extracted to better observe the seismo-electric conversion. Not only we obtained VSEP and split-spread results, but also timeslices where we see how the wavefields propagate and the conversion evolves with time in the x_1, x_3 plane.

The wellbore to wellbore model is constructed by concatenating two existing VSEP models. One of the VSEP models simulates the medium between the surface and the source in the well, while the second of the VSEP models simulates the medium between the source and the bottom of the well. In order to ensure the continuity of wavefields across the source level we feed the upgoing one-way wavefields from the lower VSEP model into the upper one, and consequently we also feed the downgoing wavefields from the upper VSEP model into the lower one. This finally gives us the results of a wellbore to wellbore simulation in the (x_1, x_3, t) domain for any well separation with all the features described in the previous paragraph.

Finally we analyze the information we can actually extract from the subsurface with a seismo-electric survey. We look at the reflection coefficient as a function of the upgoing one-way wavefield arriving to the surface from the same reflecting interface as in Section 3. After checking this coefficient with the forward coefficient we make use of a cost function to find certain parameters from the lower medium in the interface. In the cost function we compare the inverted reflection coefficients from the previous section with forward reflection coefficients that are a function of a range of values of certain medium parameters, in this case ϕ, G^{fr} and C. The results show how certain types of interfaces present more difficulties than others when trying to obtain lower medium properties.

To conclude this thesis we simulate an electro-seismic survey and we try

to obtain ϕ and C from the lower interface. For this we take into account the different sources and receivers, as well as noise, bad sampling and interface depth. We present the results as surfaces that showed how close we are from the real values of the sought parameters when the interface depth, data truncation and signal to noise ration change.

Samenvatting

Er bestaat een groeiende interesse voor het meten van het seismo-elektrisch effect als een geofysisch hulpmiddel om informatie over de ondergrond te verkrijgen. Recente ontwikkelingen in dit veld maken het aannemelijk dat deze methode binnen afzienbare tijd zal worden gebruikt als geofysische exploratie techniek. Door de gevoeligheid van de methode voor veranderingen in de porie vloeistofchemie is het ideaal voor gebruik in milieuverontreiniging problemen. Daarnaast is de methode zeer geschikt om te worden gebruikt vanuit boorgaten. De methode is een excellente uitbreiding op bestaande methodes omdat het seismo-elektrisch effect altijd optreedt bij al bestaande seismische en elektromagnetische meetmethoden.

Het doel van het onderzoek waarover in dit proefschrift wordt gerapporteerd is het onderzoeken van de mogelijkheden die het seismo-elektrische effect bieden in bekende meetmethoden en de mogelijkheid daadwerkelijk nieuwe informatie over de ondergrond te verkrijgen. Hiertoe hebben we een aantal operatoren ontwikkeld die ons model beschrijven van een drietal zogenaamde split-spread metingen. De eerste heeft zowel de zender als ontvangers aan het oppervlak, de tweede de zender aan het oppervlak en de ontvangers in een boorgat (VSEP), of omgekeerd, en de derde met de zender in een boorgat en de ontvangers in een ander boorgat (boorgat naar boorgat).

We beginnen met de vergelijkingen van Pride [18] voor de gekoppelde beschrijving van elektromagnetische en akoestische golven in poreuze media. Deze vergelijkingen worden zodanig herschreven dat verticale veranderingen in bepaalde golfveldgrootheden worden uitgedrukt in de laterale veranderingen van deze golfveldgrootheden. Deze vorm wordt gecombineerd in een stelsel golfvergelijkingen in matrix-vector vorm.

Voor het geval waarbij de golven propageren in het x_1, x_3-vlak in een horizontaal gelaagde configuratie wordt aangetoond dat dit stelsel van partiële differentiaalvergelijkingen ontkoppelt in twee onafhankelijke kleinere stelsels van partiële differentiaalvergelijkingen. Deze twee stelsels beschrijven de twee verschillende

mechanismen van seismo-elektrische koppeling: de P-SV-TM en de SH-TE koppeling. De P-SV-TM koppeling beschrijft wisselwerking tussen akoestische drukgolven (P) en vertikaal gepolariseerde akoestische schuifgolven (SV) met de transversaal magnetisch (TM) gepolariseerde elektromagnetische golven. De SH-TE koppeling beschrijft de wisselwerking tussen horizontaal gepolariseerde akoestische schuifgolven (SH) met de transversaal elektrisch (TE) gepolariseerde elektromagnetische golven.

Met behulp van een decompositie operator wordt het zogenaamde tweeweg golfveld ontbonden in twee zogenaamde éénweg golfvelden. Een tweeweg golfveld bestaat uit meetbare grootheden terwijl een éénweg golfveld uit een superpositie van opgaande en neergaande golfvelden bestaat die elk zijn opgedeeld in de verschillende golftypen. Een compositie operator reconstrueert uit de éénweg golfvelden weer de fysische golfveldgrootheden.

Een seismo-elektrische meting wordt nu beschreven met behulp van de éénweg golfvelden waarbij onderscheid wordt gemaakt tussen de verschillende onderdelen zoals, de excitatie, golfvoortplanting en reflectie. Dit deel wordt afgesloten met voorbeelden van twee gevallen om de beschreven theorie te illustreren. Eerst wordt een enkele reflectie getoond, berekend met de éénweg golfvelden, gevolgd door een meer ingewikkeld voorbeeld waarbij de excitatie en ontvangst mechanismen zijn meegenomen in de modellering.

De volgende stap is het modelleren van het meer ingewikkelde model van een meting in een configuratie met horizontaal gelaagde media. De globale seismo-elektrische reflectie- en transmissiecoëfficiënten worden afgeleid op basis van het seismische algoritme van Kennett [10]. Door deze twee coëfficiënten te combineren zijn we in staat een vertikaal seismo-elektrisch profiel (VSEP) te simuleren. Deze afleiding wordt eerst gedaan in het x_3, t domein en daarna in het x_1, x_3, t domein. In dit laatste domein wordt een datakubus gegenereerd waaruit vlakken kunnen worden uitgesneden om de seismo-elektrische omzettingen beter te kunnen observeren. We kijken niet alleen naar oppervlaktemetingen met ontvangers aan weerszijde van de bron en de VSEP meetopstelling, maar ook naar doorsneden in het x_1, x_3-vlak op vaste tijdstippen, zogenaamde tijdsneden, zodat de ontwikkelingen in de tijd van zowel de golfvoortplanting als de seismo-elektrische wisselwerking kunnen worden gevolgd in het gehele propagatievlak.

De boorgat naar boorgat configuratie wordt het meest eenvoudig gemodelleerd door twee VSEP modellen aan elkaar te koppelen in een iteratief schema. Het eerste VSEP model modelleert het deel tussen het oppervlak en de diepteposities van de bron, terwijl het tweede VSEP model de configuratie tussen de diepteposities van de bron en de onderste halfruimte modelleert. Door de simulatie van de

neergaande golfvelden van het eerste VSEP als invoer voor het tweede VSEP te nemen en de opgaande golfvelden van het tweede model te nemen als invoer voor het eerste VSEP model wordt zo het hele golfveld exact gemodelleerd na optelling van alle resultaten. Hierdoor kunnen we in het gehele x_1, x_3, t-domein een boorgat naar boorgat configuratie exact modelleren voor iedere gewenste afstand tussen de boorgaten.

We hebben de informatie geanalyseerd die we werkelijk uit de ondergrond kunnen halen met behulp van de seismo-elektrische meetmethode. Door de reflectiecoëfficiënt te destilleren uit de gesimuleerde metingen aan de hand van dataprocessing stappen op basis van ons model, zijn we in staat een kostfunctie te definiëren die geminimaliseerd kan worden door een bepaald aantal onbekende parameters te schatten. Dit is aangetoond door de oplossingruimte te bekijken in het geval dat porositeit, schuifmodulus en ion concentratie van de laag onder de reflector worden gekozen als de te schatten parameters. De resultaten laten zien dat niet elke reflector even gemakkelijk leidt tot goede schattingen van de medium parameters.

Uiteindelijk hebben we een werkelijke seismo-elektrische meting gesimuleerd zodanig dat de keuze van het aantal bronnen en ontvangers per bron positie, de tijdbemonstering, de diepte van de te analyseren reflector en het ruisniveau overeenkomen met een realistische acquisitieconfiguratie. Op basis van deze data hebben we geprobeerd de porositeit en ion concentratie van de laag onder de reflector te schatten. De resultaten hebben we gepresenteerd als oppervlakten die laten zien hoe dicht we de werkelijke waarden benaderen als functie van de signaalruis verhouding, de diepte van de reflector en de totale hoeveelheid beschikbare data.

Acknowledgements

As the reader has probably noticed, I am using the word "we" all through the thesis. The reason is that finishing this thesis would not be possible without the help and advice of many, many people. Most of them are mentioned in the following lines.

First of all I want to thank Kees Wapenaar, my supervisor and promotor, and Evert Slob, my copromotor for giving me the opportunity of this Ph.D. But above all I want to thank Kees for the all the freedom I enjoyed throughout the project, and Evert for his unlimited patience and the endless hours we spent in front of some equations or a Matlab screen.

In the first days of my Ph.D. I was completely lost (I can confess it now!), and I would still remain lost if it wasn't for the invaluable help and assistance of Arthur Denneman. In those days I had also very good support from Jeroen Goudswaard, Rob Hegge and Jan Willem Schoolmeesters in many areas, Linux, LaTeX and general stuff.

When the time for fieldwork arrived I could count on the great help and good humor of Albèr Hemstede, the fieldwork technician who fabricated parts and arranged instruments for my measurements.

Another remarkable chapter has been the supervision of master students in their final thesis. I had the pleasure of working with Dennis van den Burg in a very rewarding symbiosis, as well as with Gijs Meek who introduced me into the wonders of mathematical dutch.

In the time I worked here I have seen many people coming and going in this department, and I want to thank them all for the contribution they had to this thesis, and because with them I slowly learnt to ask better questions. Thanks among others to Ranajit Ghose, Guy Drijkoningen, Rutger van Spaendonk, Menno Dillen, Jan van der Kruk, Lourens van Zanen, Gerd Swinen, Martijn Frijnlink, Gerrit Toxopeus, Deyan Draganov, Petar Angelov, the students from DOGS, Guus Lohlefink, etc...

After spending some time at the "AIO attic" I moved to a new room with two mediterranean delights: Aletta Filippidou and Sevgi Tigrek with whom I would share the room the following years. Thanks girls for the "gezellige" mood you induced into the room and the endless conversations about anything unrelated with our respective projects. In fact the room's ambience became too good to help me finish the thesis, so I moved back to the attic where I share now a room with my roommates Cas Berentsen and Mohamed Darwish, to whom I thank the silence and tranquility I needed.

This thesis could not be finished if it wasn't for the almost daily relief I got from the Mars coffeebreak freaks: Cas, Aletta, Ainhoa, Tanguy and Sevgi who would stretch my brain before or after any silly Matlab bug would test my patience.

When it came to deal and understand the Dutch culture and way of life I got lots of good discussions and fun while hiking in the Ardennes with the Losers: Auke, Cas, Ain, Koen and Maaike.

I want to thank my family in Spain for giving me an open minded critical education and for supporting me at all times, even when I decided to leave and head for the Netherlands.

Finally I must of course thank my life friend Marco with whom I could share once again another adventure, and muchas thanks to my family in Delft: Ainhoa, Dani, Ici, Jorge and Aletta for being there all the time, and specially to Ainhoa to whom I owe a lot in this thesis.

Gracias a todos!

About the author

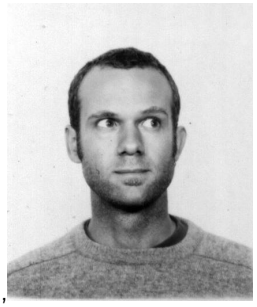

Antonio Rañada Shaw was born in Madrid, Spain, the 26^{th} of October 1970. First son of physicists, he was since early age in contact with sciences, craving for the answer to the ultimate question about the Universe, life and everything else.

He was raised in Madrid where he attended an uneventful school, graduating in 1988. In that year he entered the School of Civil Engineering and after two years he decided to follow his vocation and enrolled in the Faculty of Physics at Universidad Complutense de Madrid where he chose Geophysics to complete his Master's degree. Right after graduation he spent a year at Kent University at Canterbury, where he explored topics downright unrelated to geophysics, such as electronics and materials' science.

Antonio translated books and was radiological controller at nuclear power plants before joining Delft University of Technology to undertake his Ph.D. under the supervision of Kees Wapenaar and Evert Slob. There he learned and worked on the seismo-electric effect, its aplications and its potential. This Thesis is the final product of that Ph.D. project.